

The Choco low-level jet in CMIP5 experiments: present and future

A Thesis

Presented to

The Engineer Faculty

by

Juan Pablo Sierra Pérez

In Partial Fulfillment

of the Requirements for the Degree

Master of Environmental Engineering in the

Engineer Faculty

Universidad de Antioquia

Abril, 2017

The Choco low-level jet in CMIP5 experiments: present and future

Approved by:

Dr. Paola A. Arias, Advisor
School of Environmental Sciences
Universidad de Antioquia

Dr. Sara C. Vieira, Advisor
School of Environmental Sciences
Universidad de Antioquia

Dedication

To my family, because their love makes everything possible.

Acknowledgments

Passion is a contagious feeling. I am deeply thankful with all my professors at Universidad de Antioquia, because they taught me their love for science. Special thanks to professors Juan Fernando Salazar, Juan Camilo Villegas, and Alejandro Martínez; I feel very lucky to be their student. Above all, I am really grateful with my advisors, Paola Arias y Sara Vieira. They were an incredible support and source of inspiration during all these years and encouraged me to be a better scientist and a better person. Thanks for their inexhaustible patience and effort to make me less messy; without them, this work would not be possible.

Finally, this work was supported by “Departamento Administrativo de Ciencia, Tecnología e Innovación de Colombia” (Colciencias) Program no. 5509-543-31966. I acknowledge the World Climate Research Programme’s Working Group on Coupled Modelling, which is responsible for CMIP, and the climate modeling groups (listed in Tables 1.1, 2.1, and 3.1 of this manuscript) for producing and making available their model output. For CMIP, the US Department of Energy’s Program for Climate Model Diagnosis and Intercomparison provided coordinating support and led development of software infrastructure in partnership with the Global Organization for Earth System Science Portals. I also acknowledge the insightful comments from Rong Fu, Alejandro Martínez, and Jhan Carlo Espinoza.

Table of contents

Acknowledgments.....	4
List of tables.....	7
List of figures.....	8
Summary.....	12
Chapter 1: On the representation of precipitation over northern South America by CMIP5 global climate models.....	13
1.1 Introduction.....	13
1.2 Data and Methodology.....	14
1.3 Results.....	18
1.3.1 Simulation of the annual cycle of precipitation over northern South America.....	18
1.3.2 Possible causes of biases in the simulated annual cycle of precipitation over northern South America.....	24
1.4 Conclusions.....	29
1.5 Supplementary material.....	31
Chapter 2: How well do CMIP5 models simulate the low-level jet in western Colombia?	33
2.1 Introduction.....	33
2.2 Data and Methodology.....	36
2.2.1 The CMIP5 simulations.....	36
2.2.2 Reference data and methods.....	39
2.3 Results.....	41
2.3.1 Observations.....	41
2.3.2 Cluster analysis and model classification.....	44
2.3.3 Simulation of the basic features of the Choco jet.....	46
2.3.3.1 Annual cycle.....	48
2.3.3.2 Vertical structure.....	49
2.3.3.3 Spatial distribution.....	50

2.3.4 Representation of the mechanisms involved in the dynamics of the Choco jet.....	50
2.3.4.1 Local topography.....	51
2.3.4.2 Local surface temperature and SLP gradients.....	52
2.3.5 Connection between ITCZ and Choco jet location biases.....	55
2.3.6 Relationship between the Choco jet and precipitation over northern South America.....	61
2.3.7 Observed and simulated interannual variability of the Choco jet.....	63
2.4 Discussion and Conclusions.....	71
2.5 Supplementary material.....	79
Chapter 3: The future of the Choco low-level jet.....	80
3.1 Introduction.....	80
3.2 Data and Methodology.....	82
3.3 Results.....	84
3.3.1 Future changes in the basic features of the Choco jet.....	84
3.3.1.1 Annual cycle.....	85
3.3.1.2 Spatial distribution.....	86
3.3.2 Future changes in the mechanisms involved in the dynamics of the Choco jet.....	88
3.4 Discussion and Conclusions.....	93
3.5 Supplementary material.....	95
General Conclusions.....	98
References.....	102

List of tables

1.1 General description of the CMIP5 models used in this chapter. All models have available historical simulations during the period 1850-2005. AO: Atmosphere-Ocean General Circulation Models. ESM: Earth System Model. Chem: Models including atmospheric chemistry processes

1.2 Inter-hemispheric surface temperature gradient over the eastern tropical Pacific Ocean (15°S-20°N, 120°W-80°W) for the different seasons. Data are in °C. The asterisks indicate the reference datasets

2.1 General description of the CMIP5 models used in this chapter. All models have available historical simulations during the period 1850-2005. AO: Atmosphere-Ocean General Circulation Models. ESM: Earth System Model. Chem: Models including atmospheric chemistry processes

2.2 Inter-hemispheric temperature asymmetry index (°C), defined as the difference between the area-averaged surface air temperature north (0-20°N, 120°-80°W) and south (0-20°S, 120°-80°W) of the equator over the eastern Pacific. The index is computed considering a 1979-2005 climatology

2.3 Correlation coefficients between Choco jet index anomalies from different reanalysis and global climate indices from NOAA. Statistically significant correlations at 0.05 significance level are in bold

2.4 Correlation coefficients between Choco jet index anomalies, Niño 3.4 SST anomalies (5°S-5°N, 170°W-120°W), and precipitation anomalies over the Colombian Pacific coast (2°N-9°N, 80°W-76°W) from ERA-Interim and GCMs. AMIP models are identified with _A at the end

3.1 General description of the CMIP5 models used in this study. All models have available historical and RCP85 simulations during the periods 1850-2005 and 2006-2100 respectively

List of figures

1.1 Seasonal climatology of precipitation (mm day^{-1}) from TRMM (shaded) for: **a** DJF, **b** MAM, **c** JJA, **d** SON. Ensemble GCMs mean differences with respect to TRMM in contours

1.2 Taylor diagram quantifying the correspondence between simulated and observed rainfall seasonal climatology for the entire spatial domain (15°S – 20°N , 120°W – 0°W). Reference data corresponds to TRMM

1.3 a Map of regions selected to evaluate the simulation of the annual cycle of precipitation. Spatial mean of the rainfall annual cycle in the regions: **b** Amazon, **c** Andean, **d** Caribbean, **e** Pacific. Values in mm day^{-1} . Observations are marked with asterisks (*)

1.4 Scatter plot of rainfall spatial correlation pattern (respect to TRMM) and surface temperature (respect to ERA-Interim) for: **a** DJF **b** MAM, **c** JJA, **d** SON in the eastern Pacific (15°S – 20°N , 120°W – 80°W) as simulated by GCMs. The slope of the linear regression (m) and the correlation coefficient (R) between the two variables are presented in the upper left corner

1.5 Zonal mean of surface temperature over the eastern tropical Pacific Ocean (15°S – 20°N , 120°W – 80°W) for: **a** DJF **b** MAM, **c** JJA, **d** SON. Gray lines correspond to simulation of GCMs

S1-1 Seasonal mean precipitation flux (mm day^{-1}) over northern South America during DJF and MAM ((**A**) BCC-CSM1, (**B**) CanESM2, (**C**) CCSM4, (**D**) CESM1-FASTCHEM, (**E**) CESM1-WACCM, (**F**) FGOALS-g2, (**G**) GFDLESM-2M, (**H**) CNRM-CM5, (**I**) GISS-E2-H-CC, (**J**) CNRM5-CM5-2, (**K**) GISS-E3-R, (**L**) INMCM4, (**M**) GFDLESM2G, (**N**) IPSL-CM5B-LR, (**O**) MIROC4h, (**P**) MIROC5, (**Q**) MIROC-ESM, (**R**) MIROC-ESM-CHEM, (**S**) MPI-ESM-LR, (**T**) MPI-ESM-MR, (**U**) MPI-ESM-P, (**V**) MRI-CGCM3, (**W**) HadGEM2-CC, (**X**) HadGEM2-ES, (**Y**) NorESM1-M, (**Z**) NorESM1-ME, (**AA**) Ensemble mean, (**BB**) GPCP, (**CC**) TRMM, (**DD**) ERA-Interim). The asterisks indicate the reference datasets

S1-2 Seasonal mean precipitation flux (mm day^{-1}) over northern South America during JJA and SON ((**A**) BCC-CSM1, (**B**) CanESM2, (**C**) CCSM4, (**D**) CESM1-FASTCHEM, (**E**) CESM1-WACCM, (**F**) FGOALS-g2, (**G**) GFDLESM-2M, (**H**) CNRM-CM5, (**I**) GISS-E2-H-CC, (**J**) CNRM5-CM5-2, (**K**) GISS-E3-R, (**L**) INMCM4, (**M**) GFDLESM2G, (**N**) IPSL-CM5B-LR, (**O**) MIROC4h, (**P**) MIROC5, (**Q**) MIROC-ESM, (**R**) MIROC-ESM-CHEM, (**S**) MPI-ESM-LR, (**T**) MPI-ESM-MR, (**U**) MPI-ESM-P, (**V**) MRI-CGCM3, (**W**) HadGEM2-CC, (**X**) HadGEM2-ES, (**Y**) NorESM1-M, (**Z**) NorESM1-ME, (**AA**) Ensemble mean, (**BB**) GPCP, (**CC**) TRMM, (**DD**) ERA-Interim). The asterisks indicate the reference datasets

2.1 Basic features of the Choco jet. Annual cycle: zonal wind monthly climatology from: **a** ERA-Interim at 925hPa, **b** QuikSCAT at 10m height. **c-d** Vertical structure: seasonal climatology of zonal wind at 80°W between 5°S-9°N for MAM and SON from ERA-Interim. Spatial distribution: seasonal climatology of horizontal winds for MAM and SON from: **e-f** ERA-Interim at 925hPa, **g-h** QuikSCAT at 10m height

2.2 Cluster analysis for CMIP5 models classification in three groups: Best, Worst, and Intermediate models. **a** Dendrogram. **b** Plot of the distances between merged clusters as a function of the stage of the cluster analysis. Red dashed line indicates the optimal number of groups. **c** Scatter plot of the two first factors, which explain 79% of the total variance

2.3 Differences between Worst, Best and AMIP groups simulations respect to ERA-Interim reanalysis for the basic features of the Choco jet. **a** Differences of 925-hPa zonal winds at 80°W. **b** Vertical structure differences of the Choco jet (zonal wind) at 1000-700 hPa and 80°W during MAM and SON. **c** Seasonal climatology for horizontal winds at 925 hPa during MAM and SON. Wind differences and magnitudes are in m/s. ERA-Interim climatology is shown in contours

2.4 Representation of the mechanisms involved in the Choco jet by Worst, Best, and AMIP models. **a** Regions selected to compute temperature and sea level pressure differences (based on Poveda and Mesa 2000). **b** Annual cycle of the Choco jet index. Annual cycle of regional differences of **c-e** SLP and **f-h** temperature at 1000hPa

2.5 Latitudinal position anomalies of the eastern Pacific ITCZ and the Choco jet in **a** ERA-Interim and **b** AMIP models. Climatological annual cycle of the meridional migration of the **c** ITCZ and **d** the Choco jet by observations and model groups. **e** Scatterplot of Choco jet annual cycle PCC (respect to ERA-Interim) and zonally mean (85-80°W) ITCZ annual cycle between 5°S-12°N PCC (respect to TRMM). Blue solid lines correspond to the inter-model mean for the Choco jet and ITCZ PCCs. Circles represent Worst group models. Triangles show Best group models

2.6 **a** SLP gradient in ERA-Interim for JJA and SON. SLP gradient differences between: **b** Worst, **c** Best, **d** AMIP respect to ERA-Interim. Data in Pa*m⁻¹

2.7 Climatological zonal mean and inter-hemispheric asymmetry of precipitation. **a** Global zonally-averaged annual mean of precipitation. **b** Inter-hemispheric asymmetry (NH minus SH) of precipitation for Best, Worst, AMIP models and observations. Annual climatology is considered for the period 1979-2005

2.8 Monthly correlations between Choco jet index and precipitation anomalies over northern South America for: **a** CMIP models ((**A**) BCC-CSM1, (**B**) CanESM2, (**C**) CCSM4, (**D**) CESM1-FASTCHEM, (**E**) CESM1-WACCM, (**F**) FGOALS-g2, (**G**) GFDLES2M, (**H**) CNRM-CM5, (**I**) GISS-E2-H-CC, (**J**) CNRM-CM5-2, (**K**) GISS-E2-R, (**L**) INMCM4, (**M**) GFDLES2G, (**N**) IPSL-CM5B-LR, (**O**) MIROC4h, (**P**) MIROC5, (**Q**) MIROC-ESM, (**R**) MIROC-ESM-CHEM, (**S**) MPI-ESM-LR, (**T**) MPI-ESM-MR, (**U**) MPI-ESM-P, (**V**) MRI-CGCM3, (**W**) HadGEM2-CC, (**X**) HadGEM2-ES, (**Y**) NorESM1-

M, **(Z)** NorESM1-ME, **(AA)** ERA-Interim) **b** AMIP models (**(BB)** BCC-CSM1, **(CC)** CanAM4, **(DD)** FGOALS-s2, **(EE)** HadGEM2-AA, **(FF)** INMCM4, **(GG)** IPSL-CM5A-LR, **(HH)** IPSL-CM5A-MR, **(II)** MIROC5, **(JJ)** MIROC-ESM, **(KK)** MPI-ESM-LR, **(LL)** MPI-ESM-MR). The asterisks indicate the reference datasets. Only statistically significant correlations at 0.05 significance level are plotted

2.9 Time series for: **a** Choco jet index anomalies from NCEP-NCAR reanalysis, AMO and PDO indices from NOAA web page. All datasets smoothed with a 10-month running mean filter **b** Choco jet index and Niño3.4 SST anomalies from ERA-Interim

2.10 Wavelet power spectrums for the Choco jet index anomalies in the corresponding time period for ERA-Interim, CFSR, NCEP-DOE and NCEP-NCAR. Spectra were obtained from <http://paos.colorado.edu/research/wavelets/>, based on Torrence and Compo (1998)

2.11 Same as in Fig. 2.10, but for AMIP models

2.12 Same as in Fig. 2.11, but for CMIP models

2.13 a Scatterplot of grid size and PCC for annual cycle (left), vertical structure (middle), and the second factor obtained by Factor Analysis (section 2.3.2) (right). **b** Scatterplot of RMSE of topography and PCC of the spatial distribution of meridional wind (left), RMSE of annual cycle (middle), and the third factor (right). Correlation coefficients are shown in the lower left corner of each plots

S2-1 a Topography of Colombia from ETOPO (A*). **b** Topography differences respect to ETOPO ((BA) BCC-CSM1, (BC) CanESM2, (CD) CCSM4 and CESM1-FASTCHEM, (DE) CESM1-WACCM, (EF) CNRM-CM5 and CNRM-CM5-2, (FG) FGOALS-g2, (GH) GFDLESM-2M and GFDLESM-2G, (HI) GISS-E2-H-CC and GISS-E2-R, (IJ) HadGEM2-CC and HadGEM2-ES, (JK) INMCM4, (KL) IPSL-CM5B-LR, (LM) MIROC4h, (MN) MIROC5, (NO) MIROC-ESM and MIROC-ESM-CHEM, (OP) MPI-ESM-LR, MPI-ESM-MR and MPI-ESM-P, (PQ) MRI-CGCM3, (QR) NorESM1-M and NorESM1-ME. The asterisks indicate the reference datasets. Data in m

3.1 Annual cycle differences in the projected (under the RCP85 forcing scenario for 2070-2100) and present-day (1979-2005) zonal wind at 925hPa and 80°W. The asterisks indicate the Best models. Data in m s^{-1}

3.2 Boxplots of a Choco jet latitudinal anomalies (°), b Choco jet core intensity in present (m s^{-1}), and future conditions

3.3 Climatology differences between future (2070-2100) and present (1979-2005) horizontal winds at 925hPa for JJA. Asterisks indicate the Best models. Data in m s^{-1}

3.4 Seasonal JJA anomalies of the temperature differences at 1000hPa (°C) between: **a** Colom-ColPac, **b** ColPac-Niño, and **c** Colom-Niño. Seasonal anomalies of the SLP differences (Pa) between: **d** Colom-ColPac, **e** ColPac-Niño, and **f** Colom-Niño. **g** Area average precipitation anomalies (mm day^{-1}) over western Colombia (75°W-77.5°W, 2°N-8°N). **h** Choco jet index anomalies (m s^{-1}). Time series for the period 1979-2100

3.5 Probability density functions for seasonal JJA anomalies of: temperature differences at 1000hPa ($^{\circ}\text{C}$) between **a** Colom-ColPac, **b** ColPac-Niño, and **c** Colom-Niño. SLP differences (Pa) between **d** Colom-ColPac, **e** ColPac-Niño, and **f** Colom-Niño. **g** Area average precipitation anomalies (mm day^{-1}) over western Colombia (75°W - 77.5°W , 2°N - 8°N). **h** Choco jet index anomalies (m s^{-1}). Data from the multi-model ensemble. All PDFs exhibit changes with a 95% confidence level

3.6 Schematic diagram of the present conditions that partially explain the existence of the Choco jet and the future projected changes by GCM. A future warmer SSTs in front Ecuador-Peru coasts weaken north-south oceanic SLP gradient and push the Choco jet further south.

S3-1 Climatology differences between future (2070-2100) and present (1979-2005) horizontal winds at 925hPa for SON. Asterisks indicate the Best models

S3-2 Seasonal SON anomalies of the temperature differences ($^{\circ}\text{C}$) between: **a** Colom-ColPac, **b** ColPac-Niño, **c** Colom-Niño. Seasonal anomalies of the sea level pressure differences (Pa) between: **d** Colom-ColPac, **e** ColPac-Niño, **f** Colom-Niño. **g** Area average precipitation anomalies (mm day^{-1}) over western Colombia (75°W - 77.5°W , 2°N - 8°N). **h** Choco jet index anomalies (m s^{-1}). Time series for the period 1979-2100

S3-3 Probability density functions for seasonal JJASON anomalies of: temperature differences at 1000hPa ($^{\circ}\text{C}$) between **a** Colom-ColPac, and **b** ColPac-Niño. SLP differences (Pa) between **c** Colom-ColPac, **d** ColPac-Niño, and **e** Colom-Niño. **f** Area average precipitation anomalies (mm day^{-1}) over western Colombia (75°W - 77.5°W , 2°N - 8°N). Data from the multi-model ensemble. All PDFs exhibit changes with a 95% confidence level

S3-4 Ensemble mean of temperature difference between future (2070-2100) and present (1979-2005) climatology at 1000hPa for: **a** boreal summer, and **b** boreal fall. Data in $^{\circ}\text{C}$

S3-5 Ensemble mean of SLP gradient differences between future (2070-2100) and present (1979-2005) climatology for: **a** boreal summer, and **b** boreal fall. Data in Pa m^{-1}

Summary

South American countries exhibit a high vulnerability to climate change and natural climate variability. Hence, it is necessary for countries like Colombia to assess the possible impacts linked to climate change, in order to design adaptation strategies. The main tool for getting information about future climate are projections of global climate models (GCMs). This work aims to identify how GCMs included in the Coupled Model Intercomparison Project Phase 5 (CMIP5) simulate climate features over northern South America, especially mean seasonal precipitation and the Choco low-level jet, as well as their possible future conditions under a global warming scenario. This work is divided in three main chapters. The assessment of the ability of the CMIP5 models to represent the climatology of rainfall over northern South America is carried out in Chapter 1. The results of this chapter were presented in the “XXI Seminario de Hidráulica e Hidrología”, held on Bogotá-Colombia on August 24 to 26, 2016. Since precipitation is a complex variable and its origin processes are not well solved by global climate models, Chapter 2 analyzes the representation of the Choco low-level jet by GCMs. This jet is involved in the genesis of Mesoscale Convective System in the region, and therefore, is linked to precipitation over central and western Colombia. Products of this chapter were presented in the following events: “Observing and Modeling Climate Variability in the Intra-Americas Seas and Impacts on the Continental Americas and the Caribbean - IASCLIP Virtual Workshop” held on September 9th to 11th, 2015; “11th International Conference on Southern Hemisphere Meteorology and Oceanography” held at Santiago Chile on October 5th to 9th, 2015; “I Simposio de Hidrometeorología, Cambio Climático y Cambio Ambiental” held at Medellín-Colombia on November 30, 2015; and “II Simposio de Hidrometeorología, Cambio Climático y Cambio Ambiental” held at Medellín-Colombia on November 24, 2016. Furthermore, a paper regarding the main results discussed in this chapter is currently under review at the journal *Climate Dynamics*. Finally, the future projections of the Choco low-level jet are investigated in Chapter 3. Some of the results presented in this chapter were presented in the following events: “International Conference on Atmosphere-Biosphere Interactions, Purdue-Colombia” held at Medellín-Colombia on October 31 to November 2, 2016; and “32nd Conference on Hurricanes and Tropical Meteorology”, held at San Juan–Puerto Rico on April 17 to 22, 2016.

Chapter 1

On the representation of precipitation over northern South America by CMIP5 global climate models

1.1 Introduction

South American countries exhibit high vulnerability to climate change and natural climate variability, mainly due to their agriculture-based economy and hydro-power-based energy production (Torres and Marengo 2013). In particular, Colombian agricultural sector is responsible for generating around 21% of national employment and between 10-14% of the gross domestic product, while hydro-power satisfies 75% of the energy demand (DANE, 2011). High economic losses during La Niña 2010-2011, estimated near US \$7.8 billion, reflect the existent vulnerability in this country (Hoyos et al. 2013). However, vulnerability to extreme events is not only an economy matter, in fact, some studies recognize high mountain ecosystems are among the most sensitive environments to changes in climate conditions (Ruiz et al. 2007).

Taking into account that global climate change has consequences in regional climate, and that carbon dioxide (the main forcing for global warming) is expected to stay in the atmosphere for centuries (Schelsinger 2000), it is evident there is a need to assess the possible impacts of future climate change in order to design adaptation strategies and reduce the associated risk. The principal tool used to get an idea of the possible future climate is the analysis of projections from climate models under different greenhouse gases

emission scenarios. Recent studies from the last Intergovernmental Panel on Climate Change (IPCC) report (AR5) indicate that extreme events will probably be more intense and frequent over certain regions, including the tropics, by the end of the 21st century (Stocker et al. 2013). Furthermore, some studies indicate that El Niño Southern Oscillation (ENSO) will probably duplicate its frequency under a warmer climate (Cai et al. 2014), which could generate important socio-economic impacts over regions such as northern South America. To assess climate projections, the first step is to evaluate the ability of climate models to represent present climate. Future climate projections are often analyzed using climate models with better simulations of present climate conditions (Maloney et al. 2014). In this chapter, we look for identifying the Global Climate Models (GCMs) included in the Coupled Model Intercomparison Project Phase 5 (CMIP5) that exhibit the best representation of precipitation over northern South America, in order to validate their subsequent use in the evaluation of future climate projections. We also analyze the possible causes of the biases of the precipitation simulations in the region.

1.2 Data and Methodology

The region of interest, referred in this chapter as northern South America, is localized between 15°S-20°N and 120°W-0°W (Fig. 1.1). To assess the representation of the simulated climate in GCMs, it is common to compare simulated fields with observed fields (Glecker et al., 2008). For comparison, we use several precipitation datasets. The Tropical Rainfall Measurement Mission (TRMM) 3b43 V7 is used (Huffman et al. 2007). This dataset presents a grid size of 0.25° (around 28 km) and is available at the web page

<http://mirador.gsfc.nasa.gov/>. Besides, the reconstructed rainfall data from the Global Precipitation Climatology Project (GPCP) version 2.2 is also used (Adler et al. 2003). This dataset is the result of a combination of ground measurements, satellite gauges and statistical methods, and exhibits a horizontal resolution of 2.5° (about 278 km). In addition, this study uses two reanalysis products, which are a combination of observations, numerical methods and data assimilation techniques. We use the National Centers for Environmental Prediction Climate Forecast System Reanalysis (CFSR) (Saha et al. 2010) and the European Centre for Medium-Range Weather Forecast Interim Reanalysis (ERA-Interim) (Dee et al. 2011). CFSR, with a grid size of 38 km, overcomes its previous versions, NCEP-DOE and NCEP-NCAR, in the representation of circulation fields and rainfall (Wang et al. 2012). On the other hand, ERA-Interim is considered one of the best reanalysis over South America (Lorenz and Kunstmann 2012). This reanalysis has a horizontal resolution of about 80 km. The atmospheric variables analyzed in this chapter are rainfall and surface air temperature. Our analysis is focused over the time period 1979-2005, with an exception for TRMM dataset, which presents available data since 1998. Finally, this study uses the outputs from the historical experiment of 32 GCMs included in the CMIP5 project (Table 1.1). The historical experiment involves all observed forcings during the 20th century, including changes in the atmospheric composition due to human activities, volcanic eruptions, solar forcing, aerosol emissions, and changes in land use (Taylor et al. 2012). All datasets are in monthly resolution.

Table 1.1 General description of the CMIP5 models used in this chapter. All models have available historical simulations during the period 1850-2005. AO: Atmosphere-Ocean General Circulation Models. ESM: Earth System Model. Chem: Models including atmospheric chemistry processes

Model	Institute	Lat x Lon resolution	Type	Reference
ACCESS1-0/3	Commonwealth Scientific and Industrial Research Organisation and Bureau of Meteorology Australia	1.875 x 1.25	AO	Bi et al. 2013
BCC-CSM1.1	Beijing Climate Center	2.8 x 2.8	ESM	Xin et al. 2012
BNU-ESM	College of Global Change and Earth System Science, Beijing Normal University	2.8 x 2.8	ESM	Ji et al. 2014
CanESM2	Canadian Centre for Climate Modeling and Analysis	2.8 x 2.8	ESM	Arora et al. 2011
CCSM4	National Center for Atmospheric Research	1.25 x 0.94	AO	Gent et al. 2011
CESM1-WACCM	NSF-DOE-NCAR	1.25 x 0.9	AO	Hurrell et al. 2013
CESM1-FASTCHEM	NSF-DOE-NCAR	1.25 x 0.9	ChemAO	Hurrell et al. 2013
CMCC-CM	Centro Euro Mediterne per I Cambiamenti Climatici	0.75 x 0.75	AO	Scoccimarro et al. 2011
CNRM-CM5/2	Centre National de Recherches Meteorologiques – Centre Europeen de Recherche et Formation Avancees en Calcul Scientifique	1.4 x 1.4	ESM	Voldoire et al. 2013
CSIRO-Mk3-6-0	Commonwealth Scientific and Industrial Research Organisation and Queensland Climate Change Centre of Excellence	1.87 x 1.87	AO	Rotstayn et al. 2010
FGOALS-g2	Institute of Atmospheric Physics, Chinese Academy of Sciences	2.8 x 2.8	AO	Li et al. 2013

FIO-ESM	The First Institute of Oceanography, SOA, China		ESM	Qiao et al. 2013
GFDL-ESM2G/M	NOAA/Geophysical Fluid Dynamics Laboratory	2.5 x 2.0	ESM	Donner et al. 2011
GISS-E2-H-CC/E2-R	National Aeronautics and Space Administration (NASA) Goddard Institute for Space Studies	2.5 x 2.0	ChemAO	Kim et al. 2012
HADGEM2-CC	Met Office Hadley Centre	1.8 x 1.25	ESM	Jones et al. 2011
HADGEM2-ES	Met Office Hadley Centre	1.8 x 1.25	ChemESM	Jones et al. 2011
INM-CM4.0	Institute for Numerical Mathematics	2 x 1.5	AO	Volodin et al. 2010
IPSL-CM5B-LR/ IPSL-CM5A-LR	Institut Pierre Simon Laplace	3.75 x 1.9 2.5 x 1.26	ChemESM	Dufresne et al. 2013
MIROC4h	Atmosphere and Ocean Research Institute (The University of Tokyo), National Institute for Environmental Studies, and Japan Agency for Marine-Earth Science and Technology.	0.56 x 0.56	AO	Sakamoto et al. 2012b
MIROC5	Atmosphere and Ocean Research Institute (The University of Tokyo), National Institute for Environmental Studies, and Japan Agency for Marine-Earth Science and Technology.	1.4 x 1.4	AO	Watanabe et al. 2010
MIROC-ESM/-CHEM	Atmosphere and Ocean Research Institute (The University of Tokyo), National Institute for Environmental Studies, and Japan Agency for Marine-Earth Science and Technology.	2.8 x 2.8	ESM/ChemESM	Watanabe et al. 2010

MPI-ESM-LR/MR/P	Max Planck Institute for Meteorology	1.87 x 1.87	ESM	Zanchettin et al. 2012
MRI-CGCM3	Meteorological Research Institute	1.1 x 1.1	AO	Yukimoto et al. 2012
NorESM1-M	Norwegian Climate Center	2.5 x 1.9	ESM	Zhang et al. 2012
NorESM1-ME	Norwegian Climate Center	2.5 x 1.9	ChemESM	Tjiputra et al., 2013

In order to quantify the GCMs skill to represent present rainfall climatology, we use Taylor diagrams (Taylor 2001), which are based on different statistical metrics such as the root mean square error, the spatial correlation coefficient, and the spatial variances ratio between simulated and observed fields. Taylor diagrams are widely used because they summarize a lot of information in a single plot. Because computing all these statistical metrics is done grid by grid, we use bilinear interpolation to convert models and observations into a 2° common horizontal resolution (a common grid size in most of GCMs). The common resolution is also used to get the ensemble mean of all GCMs.

1.3 Results

1.3.1 Simulation of the annual cycle of precipitation over northern South America

The annual cycle of precipitation over northern South America is dominated by the latitudinal migration of the Inter Tropical Convergence Zone (ITCZ) (Poveda et al. 2006). Therefore, we could expect that a good representation in GCMs of the ITCZ and its annual latitudinal migration lead to an adequate simulation of precipitation over the region. During

boreal summer (June to August – JJA) and fall (September to November - SON), the ITCZ is located over the northern hemisphere whereas during boreal winter (December to February – DJF) and spring (March to May - MAM) it is located over the southern hemisphere, following the maximum warming zone (Fig. 1.1). GCMs are able to reproduce the continental ITCZ latitudinal movement although they present issues in properly locating rainfall maxima and minima inside the continent, since the spatial rainfall distribution is related to local features, such as topography, which models fail to capture. However, the ITCZ over the Atlantic and Pacific oceans is mainly located over the northern hemisphere during the whole year because of ocean-land-atmosphere interactions (Li and Philander, 1996). In average, GCMs are not able to keep the ITCZ north of the equator during boreal winter and spring, which causes dry (wet) biases over the northern (southern) part of both oceans (Fig. 1.1a-b). This bias is known as the double ITCZ problem (Hwang and Frierson, 2013). During boreal summer and fall, GCMs adequately capture the location of the oceanic ITCZ because in these months, both solar radiative forcing and ocean-land-atmosphere interactions locate the rainy belt north of the equator (Fig. 1.1c-d).

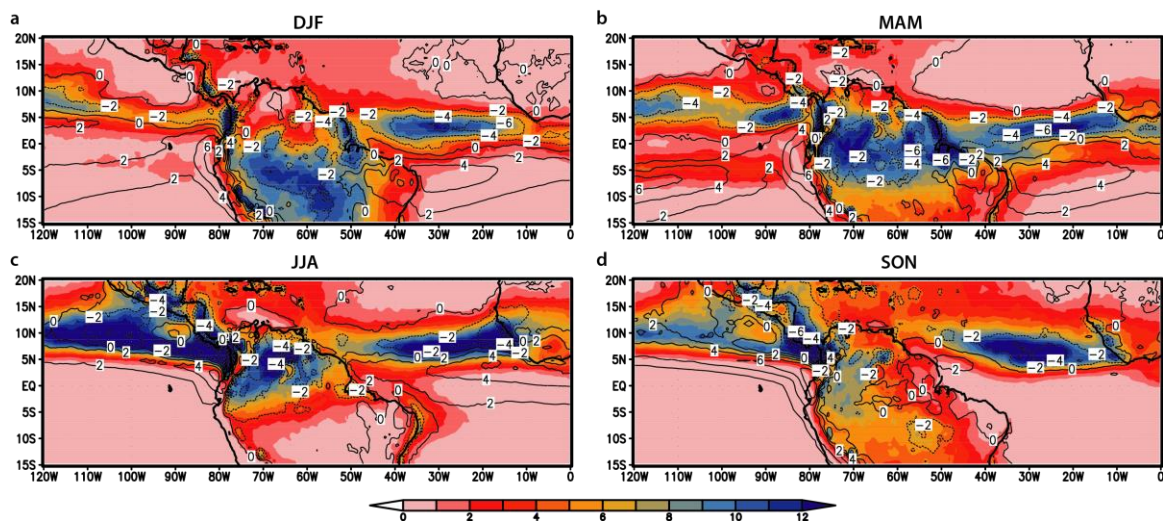


Fig. 1.1 Seasonal climatology of precipitation (mm day^{-1}) from TRMM (shaded) for: **a** DJF, **b** MAM, **c** JJA, **d** SON. Contours represent ensemble GCMs mean differences with respect to TRMM

In order to qualify precipitation simulation by GCMs, Figure 1.2 shows Taylor diagrams for all seasons respect to TRMM. It can be noticed that precipitation over the region is badly represented during DJF and MAM (smaller spatial correlation for all models and higher root mean square error during these seasons) as a consequence of an erroneous southward ITCZ (Fig. 1.2a-b). On the other hand, during JJA and SON, rainfall field is better simulated as a result of an adequate location of the oceanic ITCZ (Fig. 1.2c-d). Taylor diagrams also allow us to identify models that exhibit the closest simulations to observations during the different seasons. Although there is no a single model that overcome all models during all seasons, there are some models that can be recognized for presenting a better representation of rainfall during the entire year. Among these models are HadGEM2-CC, HadGEM2-ES, ACCESS1-0, ACCESS1-3, CMCC-CM, CESM1-FASTCHEM, CCSM4, and MIROC5. Some of these models have been highlighted in other studies because of their adequate simulations of precipitation and temperature over certain regions of northern South America (IDEAM 2012, Yin et al. 2013, Sierra et al. 2015).

To further explore the representation of precipitation over the region, Figure 1.3 presents the climatological annual cycle over: Amazon region (75°W-60°W, 3°N-10°S), Andean region (76°W-73°W, 8°N-3°N), Pacific region (80°W-76°W, 9°N-2°N), and Caribbean region (76°W-70°W, 12°N-8°N).

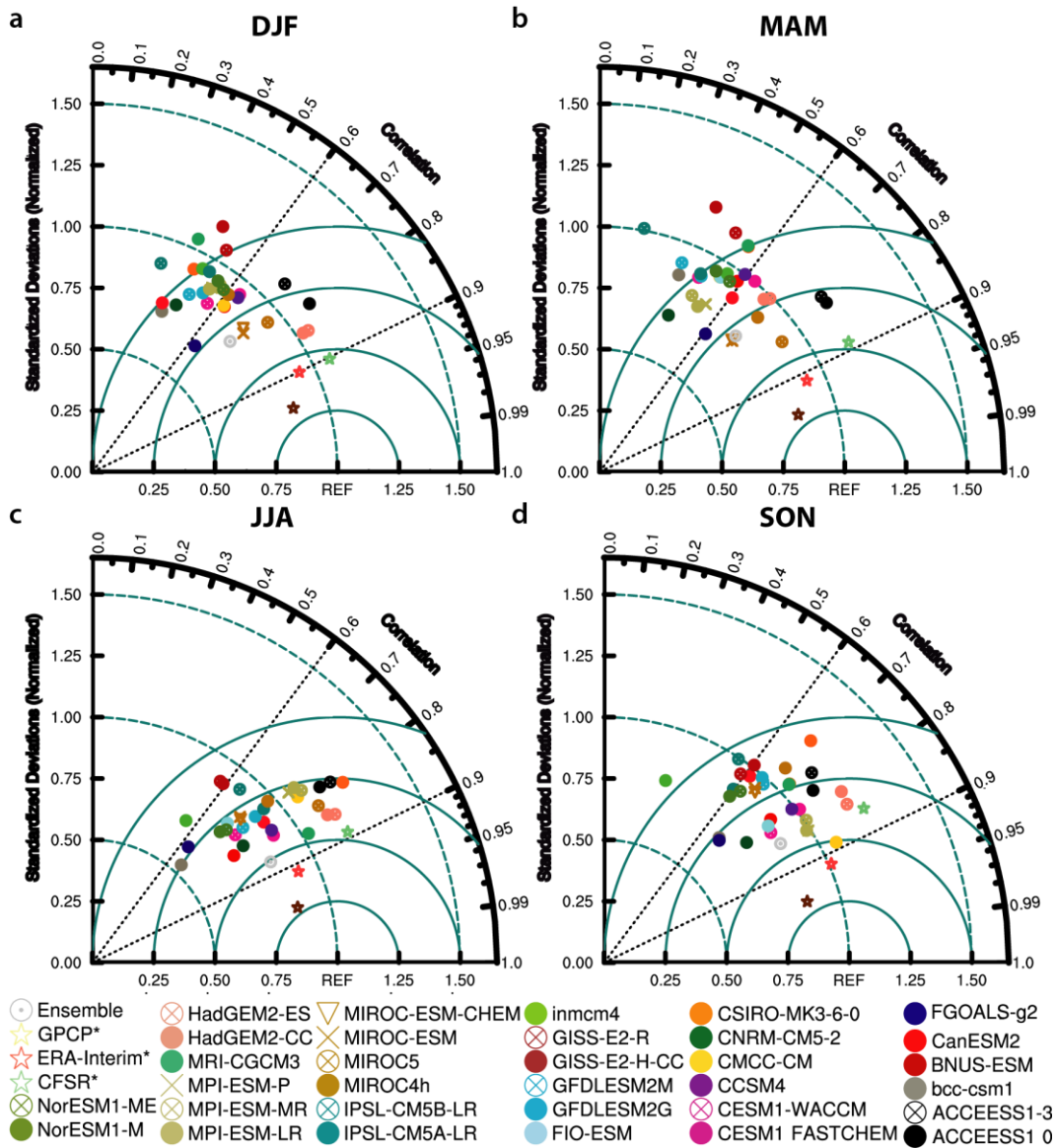


Fig. 1.2 Taylor diagram quantifying the correspondence between simulated and observed rainfall seasonal climatology for the entire spatial domain (15°S–20°N, 120°W–0°W). Reference data corresponds to TRMM

In general, all observation datasets are in agreement with the nature of the annual cycle over these regions, with some differences in rainfall magnitude. For all regions, the CFSR reanalysis overestimates precipitation respect to TRMM. The Amazon region presents a unimodal rainfall annual cycle in observations, with a single maximum (minimum) during March-May (July-September), as reported in previous studies (Fig. 1.3b) (Yin et al. 2013).

The unimodal pattern for precipitation over this region is well represented by 18 out of 32 models; however, only HadGEM2-CC, HadGEM2-ES, ACCESS1-0, and ACCESS1-3 reproduce precipitation magnitude closely to observations. Most of the GCMs considered here underestimate precipitation during the dry season over the Amazon region, as it has been established by different studies, due to an overestimation of the sensible heat and an underestimation of the latent heat in the region (Yin et al. 2013).

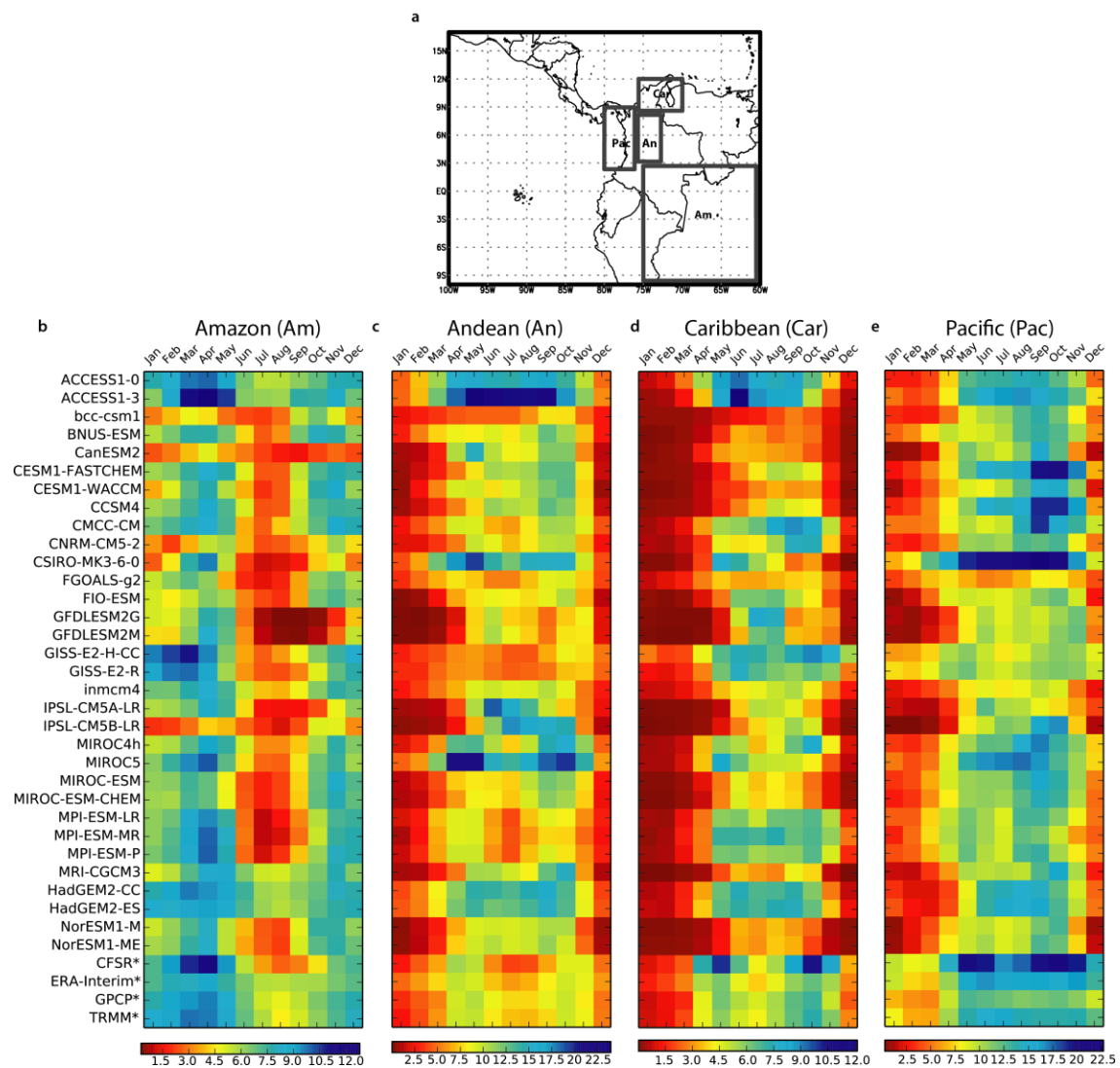


Fig. 1.3 a Map of regions selected to evaluate the simulation of the annual cycle of precipitation. Spatial mean of rainfall annual cycle in the regions: **b** Amazon, **c** Andean, **d** Caribbean, and **e** Pacific. Values in mm day⁻¹. Observations are marked with asterisks (*)

Observations indicate that the Andean region presents two rainfall peaks during April-May and October-November. Only half of the models can capture this bimodal annual cycle clearly; nevertheless most models present two peaks with almost the same magnitude during these two maxima (Fig. 1.3c). Rainfall intensity in this region is overestimated during wet months and underestimated at the beginning and the end of the year. Only ACCESS1-0, ACCESS1-3, CNRM-CM5-2, MIROC4h, MIROC5, MIROC-ESM, MIROC-ESM-CHEM, CanESM2, CSIRO, MPI-ESM-LR, MPI-ESM-MR, MPI-ESM-P, FGOALS-g2, CESM1-WACCM, and MRI can properly locate the maximum and minimum precipitation values in the annual cycle.

The annual cycle of precipitation over the Caribbean region is bimodal, with maxima rainfall during May and October (Fig. 1.3d) (IDEAM 2005). Simulation of rainfall by GCMs in this region is similar to precipitation over the Andean region. Most of GCMs exhibit an underestimation in precipitation at the beginning and the end of the year. This dry bias could be linked, as we discuss in following sections, to the erroneous southward location of the oceanic ITCZ during these months. Only 8 out of 32 models (including ACCESS1-0, ACCESS1-3, HadGEM2-CC, and HadGEM2-ES) can reproduce the bimodal pattern in the rainfall annual cycle over this region.

The Pacific region shows a disagreement between observed datasets. The CFSR reanalysis exhibits a bimodal pattern with maximum rainfall intensities during April and October. On the other hand, ERA-Interim, GPCP, and TRMM present a unimodal annual cycle with quasi-constant precipitation from May to November (Fig. 1.3e). It is particularly difficult for GCMs to realistically represent the annual cycle of precipitation over this region. Precipitation is underestimated during December-April, what leads to erroneous

precipitation minima in January (with the exception of HadGEM2-ES and HadGEM2-CC). GISS-E2-H-CC, GISS-E2-R, GFDLESM-2M, GFDLESM-2G and FIO-ESM present the best representation of rainfall in the Pacific region during the wet months of May-November (Fig. 1.3e).

1.3.2 Possible causes of biases in the simulated annual cycle of precipitation over northern South America

The spatial distribution of precipitation over the oceans is closely linked to sea surface temperatures (SSTs). Over oceans, regions with high rainfall intensities are commonly located over the warmest places because these regions enhance convective activity through heat and moisture fluxes (Hirota and Takayabu 2013). Therefore, a realistic representation of SSTs is mandatory in order to properly simulate rainfall distribution over oceans. Previous works identify an anomalous warming of the Southern Ocean as one of the causes for the double ITCZ bias, which seems to be related with a cloud deficit over the southern hemisphere (Hwang and Frierson 2013).

Figure 1.4 shows a scatter plot between the spatial correlation coefficient for precipitation over the eastern tropical Pacific (15°S - 20°N , 120°W - 80°W) and correlation coefficient for surface temperature over the same region. The direct relationship between these two variables over the ocean is evident; thus, a good simulation of the spatial pattern of SSTs is related with a well-simulated precipitation distribution. During DJF and MAM, surface temperature is badly simulated by GCMs (lower spatial correlation coefficients) (Fig. 1.4 a-b), in agreement with the precipitation biases during these seasons.

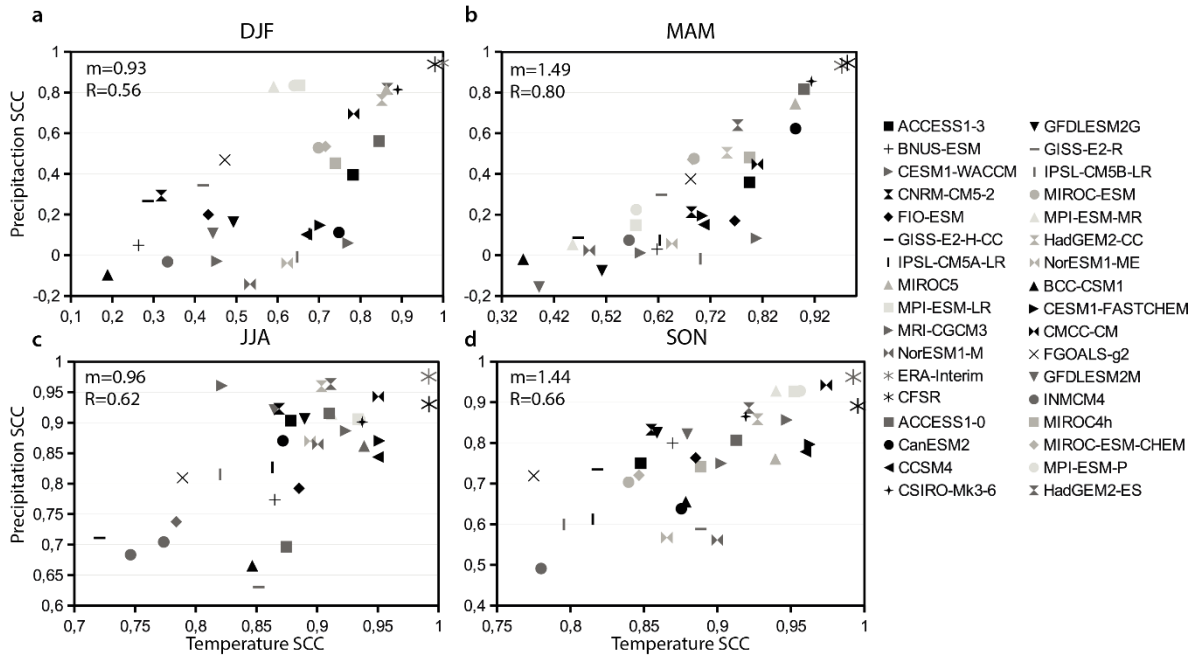


Fig. 1.4 Scatter plot of rainfall spatial correlation pattern (respect to TRMM) and surface temperature (respect to ERA-Interim) for: **a** DJF **b** MAM, **c** JJA, and **d** SON in the eastern Pacific (15°S-20°N, 120°W-80°W), as simulated by GCMs. The slope of the linear regression (m) and the correlation coefficient (R) between the two variables are presented in the upper left corner

The slope of the linear regression can be used in order to identify the sensitivity of the simulation of the spatial distribution of both variables. The linear regression slope is computed with the following equation:

$$m = \frac{\Delta SCC_{ppt}}{\Delta SCC_T} \quad [1.1]$$

where SCC_T and SCC_{ppt} represent the spatial correlation coefficients for both surface temperature and precipitation, respectively. The slope is higher during MAM and SON, indicating that small changes or improvements in the representation of surface temperature can generate important improvements in the simulation of precipitation over the eastern tropical Pacific in these seasons (Fig. 1.4 b-d). Correlation between these two variables is also the highest during these seasons, reflecting the close relationship between precipitation

and temperature at this time of the year. GCMs that better represent surface temperature over the Pacific Ocean also exhibit the most realistic ITCZ simulation (HadGEM2-ES, HadGEM2-CC, ACCESS1-0, ACCESS1-3, CMCC-CM, and CSIRO). These models also present a well-represented annual cycle of precipitation over the different regions discussed in the previous section. Conversely, GCMs that exhibit the driest biases over the Andean, Pacific, and Caribbean regions during boreal winter and spring tend to present the lowest spatial correlations of temperature and precipitation over the Pacific Ocean. This suggests that the dry biases in the annual cycle over the different continental regions between December-May could be related to an anomalous southward location of the oceanic ITCZ in the Pacific.

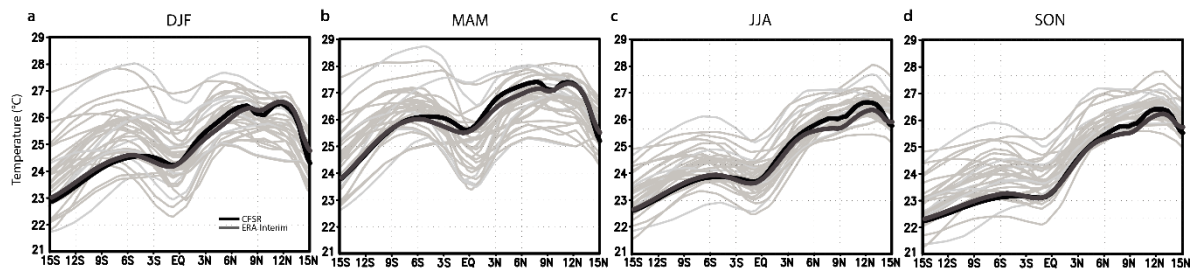


Fig. 1.5 Zonal-mean surface temperature climatology over the eastern tropical Pacific Ocean (120°W-80°W) for: **a** DJF **b** MAM, **c** JJA, and **d** SON. Gray lines correspond to simulations of GCMs

In order to get an idea about the behavior of the observed and simulated inter-hemispheric surface temperature gradient over the tropical Pacific, Figure 1.5 shows the zonal average of this variable between 120°W-80°W. Additionally, Table 1.2 present the inter-hemispheric surface temperature gradient in the same region, which is computed as the difference between the area averaged temperature north of the equator (up to 15°N) minus the area averaged temperature south of the equator (15°S). Surface temperature is higher north of the equator during the entire year in observations, generating a positive inter-

hemispheric gradient (Table 1.2). During boreal winter and spring, GCMs underestimate (overestimate) temperature north (south) of the equator (Fig. 1.5a-b), that leads to a weaker-than-observed inter-hemispheric gradient during DJF and MAM (Table 1.2). Some GCMs invert the temperature gradient sign and exhibit a warmer ocean south of the equator during the first half of the year (BCC, BNUS, CNRM, GISS, and MRI). Although the overestimation of surface temperature south of the equator by GCMs occurs during the whole year, during JJA and SON the temperature north of the equator is also overestimated, causing a positive inter-hemispheric gradient (Table 1.2).

Table 1.2 Inter-hemispheric surface temperature gradient over the eastern tropical Pacific Ocean (15°S-20°N, 120°W-80°W) for the different seasons. Data are in °C. Asterisks indicate reference datasets

Global Climate Models	DJF	MAM	JJA	SON
ACCESS1-0	1,61	1,22	2,76	3,33
ACCESS1-3	1,72	1,18	2,87	3,84
BCC-CSM1	-0,67	-0,61	2,66	2,77
BNUS-ESM	-0,05	0,02	2,22	2,52
CanESM2	1,26	1,47	3,55	3,78
CESM1-FASTCHEM	0,39	0,18	2,75	3,05
CESM1-WACCM	0,58	0,41	2,68	3,11
CCSM4	0,30	0,13	2,65	2,92
CMCC-CM	0,75	0,56	2,70	3,02
CNRM-CM5-2	-0,28	-0,11	2,46	2,46
CSIRO-Mk3-6	2,34	2,20	4,41	5,12
FGOALS-g2	0,44	0,20	1,80	2,17
FIO-ESM	0,34	0,38	1,66	1,82
GFDL-ESM2G	0,69	-0,15	3,62	4,73
GFDL-ESM2M	0,31	-0,56	2,70	3,68
GISS-E2-H-CC	-0,39	-0,65	1,58	1,99
GISS-E2-R	0,14	-0,00	2,13	2,57
INMCM4	-0,31	-0,26	1,32	1,49
IPSL-CM5A-LR	0,78	0,21	3,44	3,58
IPSL-CM5B-LR	0,90	0,19	2,82	3,25
MIROC4h	1,21	1,16	3,52	3,43
MIROC5	1,51	1,48	3,06	3,44
MIROC-ESM	1,55	1,70	3,24	3,49
MIROC-ESM-CHEM	1,63	1,66	3,32	3,57
MPI-ESM-LR	1,16	0,61	2,92	3,39

MPI-ESM-MR	0,84	0,36	2,69	3,28
MPI-ESM-P	1,24	0,73	3,01	3,49
MRI-CGCM3	-0,03	-0,04	1,61	2,05
HadGEM2-CC	1,33	0,45	2,47	3,27
HadGEM2-ES	1,55	0,71	2,67	3,52
NorESM1-M	0,35	-0,03	2,51	2,94
NorESM1-ME	0,66	0,23	2,68	3,17
CFSR*	1,79	1,41	3,31	3,75
ERA-Interim*	1,71	1,33	2,94	3,44
Ensemble	0,74	0,47	2,70	3,13

In general, GCMs that better represent the inter-hemispheric surface temperature gradient throughout the year exhibit a better simulation of precipitation over northern South America, as well as the annual cycle over the interest regions (ACCESS1-0, ACCESS1-3, CSIRO, and MIROC5). This result is in agreement with our hypothesis that an anomalous southward ITCZ over the Pacific and Atlantic oceans during DJF and MAM, caused by an anomalous warmer ocean south of the equator, is related to an underestimation of precipitation during the same seasons over different continental regions (Andean, Caribbean, and Pacific regions) (see supplementary material). However, some models present a good simulation of the inter-hemispheric temperature gradient and also exhibit a poor representation of precipitation in DJF (CanESM2). Other models, such as GISS-E2-R and GISS-E2-H-CC, invert the inter-hemispheric temperature gradient over the Pacific Ocean but do not exhibit dry biases over the regions of interest. This can be explained by the double ITCZ simulated by these models (see supplementary material). The different performances of GCMs reflect the complexity of the model representation of several physical processes related to rainfall. In addition, there are more important factors that influence the simulation of precipitation in these models, such as the representation of surface energy fluxes (Yin et al. 2013), soil moisture, and the role of the convection

schemes (Hirota and Takayabu 2013). The latter is beyond the scope of the discussion presented in this chapter, however understanding the role of these schemes could lead to improve our knowledge of the origin of precipitation errors in the simulations of GCMs over northern South America.

1.4 Conclusions

This chapter is intended to assess the ability of the last generation GCMs to represent the present climatology of precipitation over northern South America, in order to identify the models that exhibit the best simulations over the region and to analyze the possible causes of biases of rainfall simulations. In summary, GCMs have problems to simulate precipitation over the region during DJF and MAM, due to an anomalous southward location of their simulated oceanic ITCZ during the same seasons. This error in the location of the oceanic rain belt is produced, as previous studies find, by an overestimation of the surface temperature south of the equator in the eastern Pacific Ocean. Our results show that errors in the latitudinal position of the oceanic ITCZ during boreal winter and spring are linked to dry bias in the precipitation annual cycle over several continental regions (Andean, Pacific, and Caribbean regions). On the other hand, during boreal summer and fall, the eastern Pacific ITCZ is better represented by GCMs because during these months, both solar forcing, as well as ocean-land-atmosphere interactions, locates the ITCZ north of the equator. Although in a general sense, a good representation of the surface temperature over the eastern tropical Pacific is related with a satisfactory simulation of rainfall over the same region, our results suggest that during MAM and SON, small improvements in the

simulation of temperature spatial distribution can lead to significant improvements in precipitation spatial pattern. Using Taylor diagrams, annual cycles in continental regions, and the inter-hemispheric temperature gradients over the Pacific Ocean, we identify that some models (ACCESS1-0, ACCESS1-3, HadGEM2-CC, and HadGEM2-ES) present a better simulation of rainfall over northern South America. Because precipitation is the result of several complex processes, our findings exhibit important limitations as leaving aside many of these processes, such as surface energy fluxes, which could contribute to a better understanding of precipitation biases over the region. Among the different processes contributing to precipitation variability in northern South America are the local low-level jets, such as the Choco jet. Next chapter is focused on the simulation of this particular feature by CMIP5 models.

1.5 Supplementary material



Fig. S1-1 Seasonal mean precipitation flux (mm day^{-1}) over northern South America during DJF and MAM ((A) BCC-CSM1, (B) CanESM2, (C) CCSM4, (D) CESM1-FASTCHEM, (E) CESM1-WACCM, (F) FGOALS-g2, (G) GFDLESM-2M, (H) CNRM-CM5, (I) GISS-E2-H-CC, (J) CNRM5-CM5-2, (K) GISS-E3-R, (L) INMCM4, (M) GFDLESM2G, (N) IPSL-CM5B-LR, (O) MIROC4h, (P) MIROC5, (Q) MIROC-ESM, (R) MIROC-ESM-CHEM, (S) MPI-ESM-LR, (T) MPI-ESM-MR, (U) MPI-ESM-P, (V) MRI-CGCM3, (W) HadGEM2-CC, (X) HadGEM2-ES, (Y) NorESM1-M, (Z) NorESM1-ME, (AA) Ensemble mean, (BB) GPCP, (CC) TRMM, (DD) ERA-Interim). The asterisks indicate the reference datasets

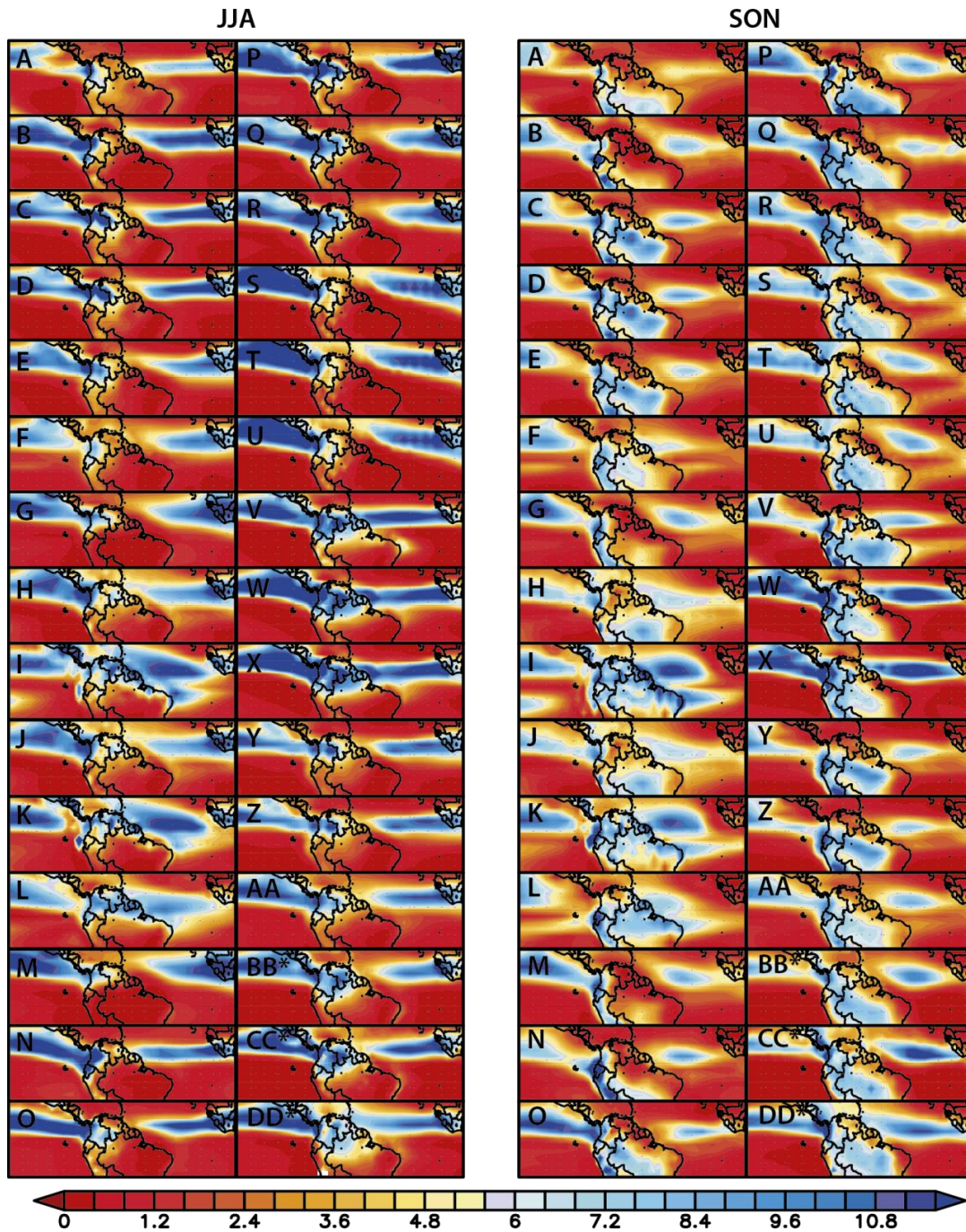


Fig. S1-2 Same as Fig. S1-1 but for JJA and SON

Chapter 2

How well do CMIP5 models simulate the low-level jet in western Colombia?

2.1 Introduction

The Choco jet (a.k.a. the western Colombia low-level jet) is an important atmospheric feature of Colombian and northern South America hydro-climatology (Poveda et al. 2011). This jet consists of a westerly low-level circulation over the eastern tropical Pacific that enters into the continent nearly at 5°N, carrying moisture from the Pacific Ocean to western and central Colombia (Poveda and Mesa 2000, Sakamoto et al. 2012a, Arias et al. 2015). The Choco jet exhibits a core at 925hPa and a marked annual cycle, with minor (major) activity during February-March (September-November) (Sakamoto et al. 2012a, Arias et al. 2015). The existence of this jet and its interaction with local topography induces the formation of Mesoscale Convective Systems (MCSs) in the region, partially explaining the large precipitation amounts observed in the Colombian Pacific lowlands (Mapes et al. 2003, Zuluaga and Poveda 2004). The average moisture transported by the Choco jet is estimated to be about 3774 m³/s, feeding the Atrato and San Juan rivers, which are among the rivers with the highest runoff rates on the world (Poveda and Mesa 2000). However, this jet is not only important due to its moisture transport but also to its interaction with several atmospheric regional phenomena such as the ITCZ, the Caribbean low-level jet (CLLJ)

(Amador 1998; 2008), and the easterly winds of the Equatorial Mid-Tropospheric Easterly Jet (EMTEJ).

The existence of the Choco jet is explained by a combination of several features: (i) SST and sea level pressure (SLP) gradients between the Ecuador-Peru cold tongue and western Colombian coast (Fig. 2.4a); (ii) predominant north-south orientation of the South American northwestern coast; (iii) topographic lifting; (iv) latent heat release in MCSs and its associated convection; and (v) change of sign of the Coriolis term between northern and southern hemispheres (Poveda and Mesa 2000, Poveda et al. 2014). In addition, recent studies suggest the possible influence of the Choco-Darien tropical rainforest in the maintenance of this jet (Poveda et al. 2014). Due to the role of SST gradients between Ecuador-Peru and the Colombian Pacific coast, the interannual variability of this jet is strongly modulated by ENSO, which modifies these temperature gradients, weakening (strengthening) the jet intensity during its warm (cold) phase (Poveda and Mesa 2000, Poveda et al. 2011, Arias et al. 2015, Hoyos et al. 2017). A weakening of the Choco jet reduces moisture advection to northern South America (Poveda et al. 2001), decreasing the amount and intensity of MCSs in the region (Zuluaga and Poveda 2004). These changes, and modification on the Hadley and Walker circulation during ENSO events explain the drier (wetter) conditions over western and central Colombia observed during El Niño (La Niña) phase (Poveda and Mesa 2000, Ambrizzi et al. 2004).

Other studies indicate that the Choco jet exhibits variability in longer time scales. Particularly, proxy-based studies suggest that this jet was stronger during the Last Glaciation due to an increased SST gradient between the eastern Pacific and northern South American coast (La Niña-like conditions), turning western Colombia wetter (Martínez et al.

2003). In this context, we could expect that future changes in atmospheric and oceanic temperatures related with global warming may modify the intensity of the Choco jet, bringing considerable consequences for the region's ecosystems and populations.

GCMs are among the main tools used to investigate future climate conditions under several external forcing scenarios (Flato et al. 2013). Several studies assess the representation of different low-level jets in the American continent by the most recent generation of GCMs grouped in CMIP5 project and previous versions (Jiang et al. 2007, Martin and Schumacher 2011, Ryu and Hayhoe 2013, Sheffield et al. 2013, Sierra et al. 2015). However, only a few studies evaluate the representation of the Choco jet, although using a limited sample of models. Sierra et al. (2015) identify that models with a better representation of the oceanic ITCZ and the Choco jet exhibit a better representation of seasonal rainfall pattern over northern South America. Although the GCMs evaluated in this study reproduce the Choco jet and its annual cycle, the missing data linked to model horizontal resolution limits the adequate simulation of some features of the jet, such as its vertical structure. Taking into account the lack of studies addressing the ability of GCMs to represent the Choco jet, the long-term variability of this jet suggested by proxies, and its possible future change linked to global warming, this chapter assesses the representation of the basic features of this jet by the CMIP5 historical experiment. To achieve this goal, we perform a classification based on model skills and determine to what extent the biases presented in CMIP5 historical simulations are related to the atmospheric or oceanic components of the models. This chapter is divided in the following sections: section 2.2 describes the datasets and methods used; section 2.3 describes the results of our evaluation; and section 2.4 presents a brief summary and discussion of our main findings and their possible implications.

2.2 Data and Methodology

2.2.1 The CMIP5 simulations

This study uses the historical runs of 26 coupled GCMs (CMIP) and 11 uncoupled atmospheric GCMs (AMIP) included in CMIP5 archives. AMIP models consist of the atmospheric component of the GCMs forced with observed SSTs. The historical experiment involves all forcing observed during the twentieth century, including changes in the atmospheric composition due to human activities, volcanic eruptions, solar forcing, aerosol emissions, and changes in land use (Taylor et al. 2012). The evaluation of CMIP and AMIP models allow identifying whether model biases arise from their atmospheric or their oceanic component (Martin and Schumacher 2011). Table 2.1 shows the description and references for each model used in this study. In order to identify the impact of model horizontal resolution on the representation of the basic features of the Choco jet, we keep model outputs at its original grid size, and only interpolate to a coarse resolution ($2.8^\circ \times 2.8^\circ$) through bilinear interpolation to compute ensemble means.

Table 2.1 General description of the CMIP5 models used in this chapter. All models have available historical simulations during the period 1850-2005. AO: Atmosphere-Ocean General Circulation Models. ESM: Earth System Model. Chem: Models including atmospheric chemistry processes

Model	Institute	Lat x Lon resolution	Type	CMIP/AMIP	Group	Topography RMSE (m)	Topography bias (%)	Reference
BCC-CSM1.1	Beijing Climate Center	2.8 x 2.8	ESM	CMIP/AMIP	Intermediate	611.83	-11.17	Xin et al. 2012
CanESM2	Canadian Centre for Climate Modeling and Analysis	2.8 x 2.8	ESM	CMIP/AMIP	Intermediate	494.16	41.91	Arora et al. 2011

CCSM4	National Center for Atmospheric Research	1.25 x 0.94	AO	CMIP	Intermediate	531.31	-8.31	Gent et al. 2011
CESM1-WACCM	NSF-DOE-NCAR	2.5 x 1.9	AO	CMIP	Intermediate	730.97	-23.98	Hurrell et al. 2013
CESM1-FASTCHEM	NSF-DOE-NCAR	1.25 x 0.9	ChemAO	CMIP	Intermediate	521.34	-8.31	Hurrell et al. 2013
CNRM-CM5/2	Centre National de Recherches Meteorologiques–Centre Europeen de Recherche et Formation Avancees en Calcul Scientifique	1.4 x 1.4	ESM	CMIP	Best	479.97	-1.43	Volodire et al. 2013
FGOALS-g2	Institute of Atmospheric Physics, Chinese Academy of Sciences	2.8 x 2.8	AO	CMIP/AMIP	Intermediate	500.57	7.55	Li et al. 2013
GFDL-ESM2GM	NOAA/Geophysical Fluid Dynamics Laboratory	2.5 x 2.0	ESM	CMIP	Intermediate	367.18	12.58	Donner et al. 2011
GISS-E2-H-CC/E2-R	National Aeronautics and Space Administration (NASA) Goddard Institute for Space Studies	2.5 x 2.0	ChemAO	CMIP	Intermediate	393.53/379.23	17.64/20.44	Kim et al. 2012
HADGE M2-CC	Met Office Hadley Centre	1.8 x 1.25	ESM	CMIP/AMIP	Best	551.00	-9.85	Jones et al. 2011
HADGE M2-ES	Met Office Hadley Centre	1.8 x 1.25	ChemESM	CMIP/AMIP	Best	551.00	-9.85	Jones et al. 2011
INM-CM4.0	Institute for Numerical Mathematics	2 x 1.5	AO	CMIP/AMIP	Worst	680.24	-7.68	Volodin et al. 2010
IPSL-	Institut Pierre	3.75 x	ESM	CMIP/AMIP	Intermediate	560.36	-11.09	Dufresne

CM5B-LR	Simon Laplace	1.9			diate			et al. 2013
MIROC4h	Atmosphere and Ocean Research Institute (The University of Tokyo), National Institute for Environmental Studies, and Japan Agency for Marine-Earth Science and Technology.	0.56 x 0.56	AO	CMIP	Intermediate	338.02	3.56	Sakamoto et al. 2012b
MIROC5	Atmosphere and Ocean Research Institute (The University of Tokyo), National Institute for Environmental Studies, and Japan Agency for Marine-Earth Science and Technology.	1.4 x 1.4	AO	CMIP/AMIP	Intermediate	556.66	-5.64	Watanabe et al. 2010
MIROC-ESM	Atmosphere and Ocean Research Institute (The University of Tokyo), National Institute for Environmental Studies, and Japan Agency for Marine-Earth Science and Technology.	2.8 x 2.8	ESM	CMIP/AMIP	Intermediate	530.73	6.26	Watanabe et al. 2010

MIROC-ESM-CHEM	Atmosphere and Ocean Research Institute (The University of Tokyo), National Institute for Environmental Studies, and Japan Agency for Marine-Earth Science and Technology.	2.8 x 2.8	ChemESM	CMIP	Intermediate	530.73	6.26	Watanabe et al. 2010
MPI-ESM-LR/MR/P	Max Planck Institute for Meteorology	1.9 x 1.9	ESM	CMIP/AMIP	Best	483.57	-2.23	Zanchettin et al. 2012
MRI-CGCM3	Meteorological Research Institute	1.1 x 1.1	AO	CMIP	Intermediate	429.46	2.25	Yukimoto et al. 2012
NorESM1-M	Norwegian Climate Center	2.5 x 1.9	ESM	CMIP	Worst	730.97	-23.99	Zhang et al. 2012
NorESM1-ME	Norwegian Climate Center	2.5 x 1.9	ChemESM	CMIP	Worst	730.97	-23.99	Tjiputra et al., 2013

2.2.2 Reference data and methods

Horizontal winds, air temperature, and SLP fields from the European Centre for Medium-Range Weather Forecasts Interim reanalysis (ERA-Interim) (Dee et al. 2011) are used. This reanalysis is considered as the best among the three current state-of-art reanalysis over some parts of South America (Lorenz and Kunstmann 2012). Consequently, this reanalysis has been widely used for studying climate conditions over northern South America (e.g., Yin et al. 2013, Poveda et al. 2014, Arias et al. 2015). Reanalysis data are interpolated using bilinear interpolation to the resolution of each model in order to compute

performance metrics. We also use NCEP-NCAR (Kalnay et al. 1996), NCEP-DOE (Kanamitsu et al. 2002), and CFSR (Saha et al. 2010) reanalyses in order to analyze the inter-annual variability of the Choco low-level jet. Furthermore, observed SST data from the Extended Reconstructed Sea Surface Temperature version 4 (ERSST v4) are used (Huang et al. 2014), and observed ocean surface winds at 10m-height data from NASA/JPL's sea wind Scatterometer (QuikSCAT) version 4 (Ricciardulli and Wentz 2011). QuikSCAT data are available for the period 1999-2009.

The ITCZ latitudinal movement is tracked using data from ERA-Interim, the Tropical Rainfall Measurement Mission (TRMM) 3B43 V7 (Huffman et al. 2007), and the Global Precipitation Climatology Project (GPCP) (Adler et al. 2003). The TRMM dataset has a spatial resolution of 0.5° and is available for the period 1998-2013. The GPCP data has a grid size of $2.5^\circ \times 2.5^\circ$ and covers the period 1979 to present.

The coupling between the ITCZ and the Choco jet in historical GCM simulations and observed data is explored taking into account the presence of autocorrelation among these time series, recognizing that serial correlation can make statistical tests less stringent, and could lead us to mistakenly reject the null hypothesis (Ebisuzaki 1997). In addition, in order to address the role of topography representation in the simulation of the Choco jet, we use the digital elevation model ETOPO1, from National Geophysical Data Center-NOAA. This dataset has a 1-arc-minute grid size, available at the website <https://www.ngdc.noaa.gov/mgg/global/global.html>.

To match the available record period in all datasets and model simulations, we use monthly mean values during the period 1979-2005. For precipitation, we compute climatological means using the record period available for each dataset. In order to compute metrics to

evaluate the simulations of the Choco jet basic features (annual cycle, spatial distribution, and vertical structure), we use the Root Mean Squared Error (RMSE) and the Pattern Correlation Coefficient (PCC), which are commonly used measures of accuracy for field forecast (Taylor 2001). RMSE and PCC are computed for each model and each season. Spatial Nash-Scutcliffe coefficient is also used in order to compare this metric with PCC and RMSE results. This efficiency index is widely used for assessing the predictive power of hydrological models (Mc Cuen et al. 2006). However, we do not use Nash index for factor and cluster analysis, and it is only used as validation information. On the other hand, some of these performance metrics (RMSE and PCC) may exhibit redundant information or positive intermodel correlation, a.k.a the multicollinearity problem (Yokoi et al. 2011). To address this issue and reach an adequate GCMs classification based on their simulations of the basic features of the Choco jet, we use factor analysis. Factor analysis allows representing a big set of variables as linear combinations of a few random variables, known as “factors”; hence, the existent correlation between the original variables makes possible their representation through a relatively small group of factors (Rencher 2003). Using the resultant factor scores from factor analysis, cluster analysis allows data separation into groups according to their degree of similarity and the difference between individual observations (Wilks 2011). This statistical method has been widely used in atmospheric sciences with different approaches (Yokoi et al. 2011, Wilks 2011 and references therein), and is particularly common in GCMs studies for identifying the inter-independence among different models (Knutti et al. 2013, Sanderson et al. 2015, Cannon 2015, Zubler et al. 2016). Our study uses both factor and cluster analyses in order to group different GCMs according to their ability to simulate the basic features of the Choco jet.

2.3 Results

2.3.1 Observations

We consider three basic features involved in the dynamics of the Choco jet: 1) the annual variability of the core velocities (annual cycle); 2) the seasonal variation of winds with height (vertical structure); and 3) the latitude-longitude location of the core (spatial distribution) (Fig. 2.1). Previous studies have considered these basic features to analyze the simulation of other low-level jets by GCMs (Jiang et al. 2007, Sheffield et al. 2013). Since the Choco jet is characterized by a dominant west-east surface flow, we use zonal winds to represent its annual cycle and vertical structure, and horizontal winds for its spatial distribution. We use the pressure range between 1000 and 700hPa to represent the vertical structure of the jet.

Figs. 2.1a-b show the observed annual cycle of the jet represented by of 925hPa zonal winds at 80°W, between 5°S and 20°N. The jet exhibits a clear annual cycle, with stronger intensity during SON and reduced activity during MAM, as previous studies indicate (Poveda and Mesa 2000). Although the jet is active throughout the entire year, it exhibits a seasonal latitudinal migration/amplification, with a further-south location between January-April, around 4°S-5°N; on the other hand, the Choco jet extends up to 9°N during the rest of the year, with a maximum intensity around 5°N. Both reanalysis data and satellite measurements from QuikSCAT agree on the latitudinal migration of the Choco jet along the year, although QuikSCAT indicate a stronger core than ERA-Interim.

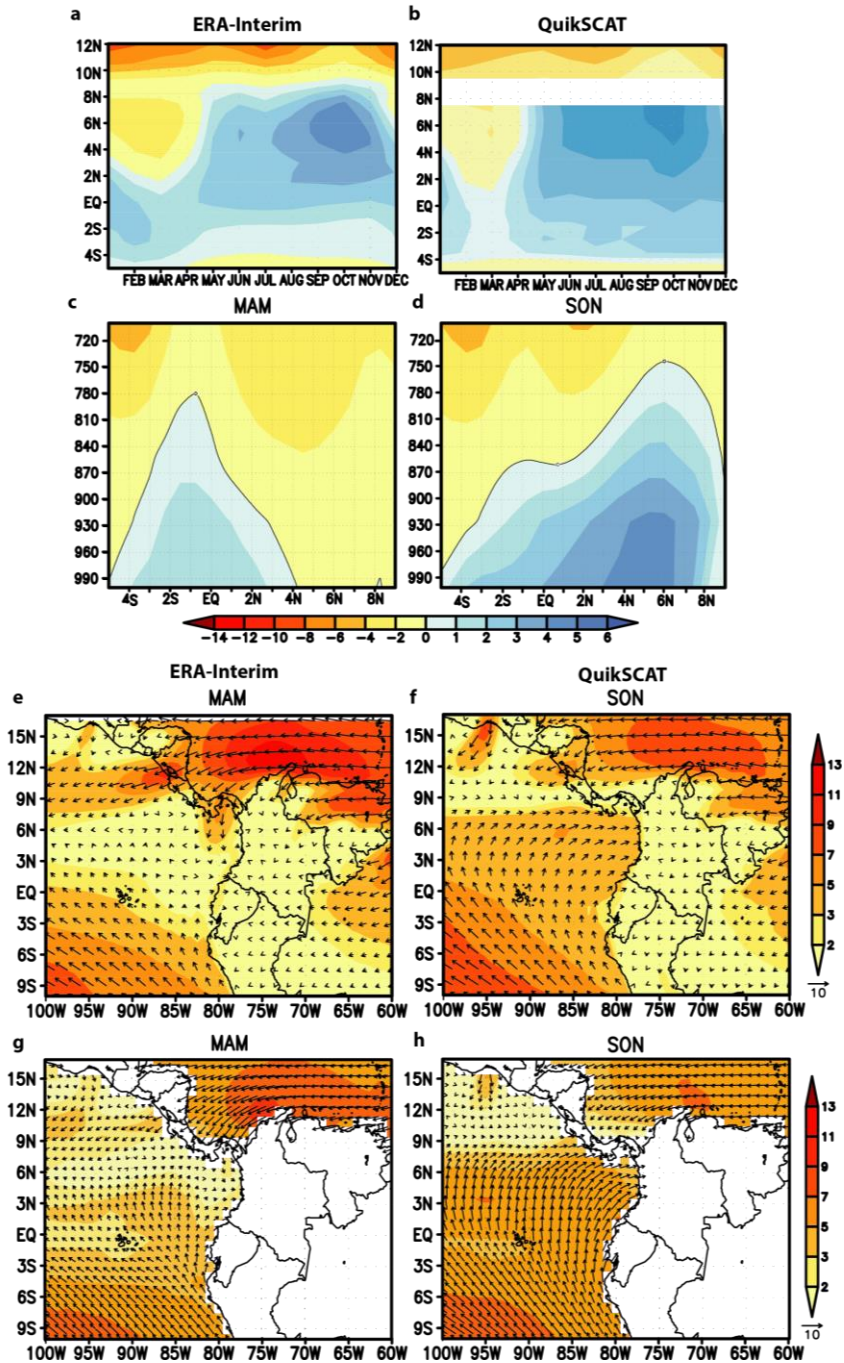


Fig. 2.1 Basic features of the Choco jet. Annual cycle: zonal wind monthly climatology from: **a** ERA-Interim at 925hPa, **b** QuikSCAT at 10m height. **c-d** Vertical structure: seasonal climatology of zonal wind at 80°W between 5°S-9°N for MAM and SON from ERA-Interim. Spatial distribution: seasonal climatology of horizontal winds (vectors) and wind magnitude (shading) for MAM and SON from: **e-f** ERA-Interim at 925hPa, **g-h** QuikSCAT at 10m height. Wind magnitudes are in m s^{-1}

The Choco jet depth varies throughout the year, reaching its maximum height (up to 750hPa) during SON (Figs. 2.1c-d), bounded by the easterly winds that shape the EMTEJ. During DJF (not shown) and MAM, the westerly winds of the Choco jet enter into the continent along 3°S-4°N (Figs. 2.1e-g). However, during JJA (not shown) and SON, the jet moves northward, amplifying its latitudinal band and reaching the South American land mass between 2°S-8°N (Fig. 2.1f-h). The similarity between ERA-Interim and QuikSCAT horizontal distribution and annual cycle of the Choco jet indicates that the reanalysis product captures the main features of this jet; therefore, we use ERA-Interim as reference data to evaluate CMIP5 models simulations.

2.3.2 Cluster analysis and model classification

To evaluate CMIP5 models performance in simulating the Choco jet, we compute RMSE and PCC for the basic features considered respect to ERA-Interim, during all seasons. In the assessment of the spatial distribution, we use a region centered on the jet (5°S-10°N, 85°W-75°W). For this feature, we analyze the representation of horizontal winds, which involves zonal and meridional winds, as well as the total wind magnitude. The RMSE and PCC provide complementary statistical information about model simulations: while the RMSE gives information about the amplitude and magnitude of the simulated field respect to observed field, the PCC measures the pattern similarity of these two fields (Taylor 2000). We also compute the Nash-Scutcliffe coefficient in order to validate the information obtained by PCC and RMSE, but this index is not used in factor and cluster analysis. In order to eliminate the multi-collinearity problem observed between these metrics and to

reduce the number of variables used, we implement a factor analysis. This analysis allows us to reduce the set of performance variables to only three factors, explaining the 90% of the original variance. These factors are the inputs for the cluster analysis, which employs the Ward's minimum variance method, a common technique for merging groups, joining clusters and minimizing the total sum of squared distances between models and the centroids of their respective groups (Wilks 2011).

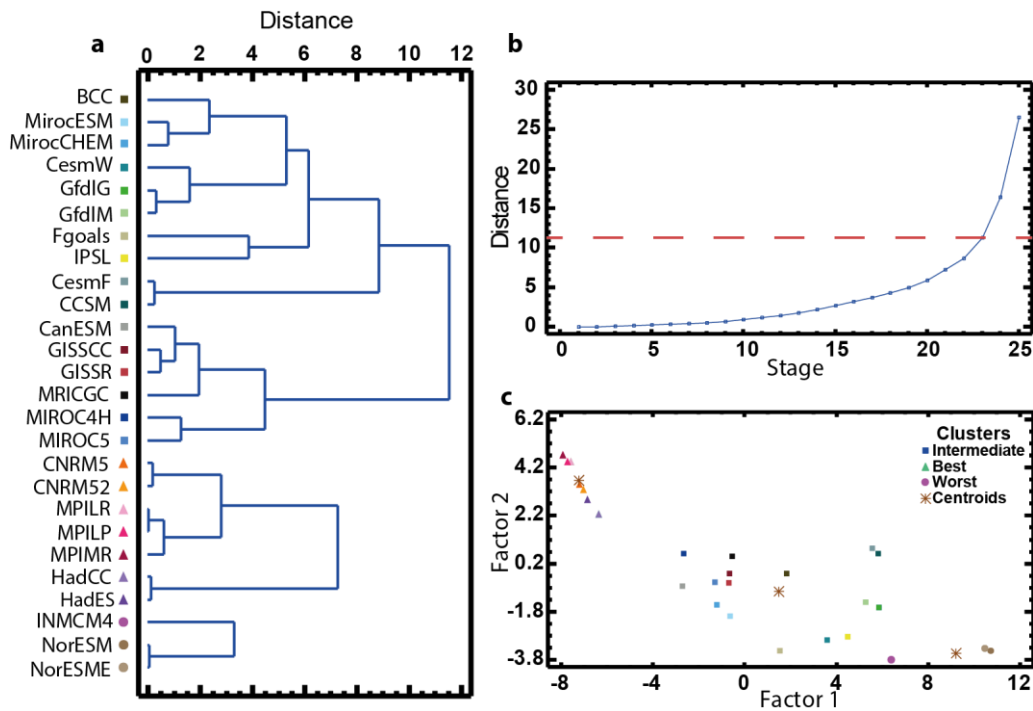


Fig. 2.2 Cluster analysis for CMIP5 models classification in three groups: Best, Worst, and Intermediate models. **a** Dendrogram. **b** Plot of the distances between merged clusters as a function of the stage of the cluster analysis. Red dashed line indicates the optimal number of groups. **c** Scatter plot of the two first factors, which explain 79% of the total variance

Figure 2.2 shows the results of the cluster analysis. At the first stages of the grouping process, the distances between groups are small since the clusters are not well defined, and models belonging to the same institute tend to merge because of their similarities (Fig. 2.2a). During each further stage, clusters are formed and start to differentiate from each

other until they join in a single group. Hence, an important question in cluster analysis is which intermediate stage or number of clusters should be chosen. A simple way to find out the optimal number of clusters is based on the inspection of the plot of distances between merged clusters, as a function of the stage of the analysis (Wilks 2011). Fig. 2.2b shows the distances plot for the cluster analysis performed in this study. A jump in the distances occurs when we identify three clusters, named “Best”, “Worst”, and “Intermediate” models. Models included in the Best group have been highlighted in previous works because of their accurate simulation of precipitation and SLP fields over northern South America (Yin et al. 2013, Palomino-Lemus et al. 2014, Sierra et al. 2015). On the other hand, the models included in the Worst group have been identified as those with the strongest double ITCZ bias (Li and Xie, 2014). Consistently, this group of models shows the worst simulation of the Choco jet main features considered here, as discussed in following subsections. In order to explore whether these clusters are adequately selected or not, we plot the two first factors explaining 79% of the total variance (Fig. 2.2c). The three groups selected are clearly separated, with Best models showing greater values for the second factor and smaller values for the first factor, whereas Worst models exhibit the opposite pattern. We also evaluate the robustness of the resulting clusters by adding and subtracting other variables to the analysis. Thus, we consider RMSE and PCC for the annual cycles of temperature and pressure gradients among explicative regions of the Choco jet (Fig. 2.4), using other definitions of distances (e.g. squared Euclidean distance) and other grouping approaches (e.g. single and average linkage). The results obtained are equivalent to those shown in Fig. 2.2 (not shown).

2.3.3 Simulation of the basic features of the Choco jet

Fig. 2.3 shows the climatological differences between the reference datasets (Fig. 2.1) and the ensemble mean of Best, Worst, and AMIP models. We consider AMIP models listed in Table 2.1. In summary, there is a clear difference in the simulation of the Choco jet basic features in Best and Worst models. However, a remarkable result is that all GCMs considered in this study are able to simulate the reversal of the easterly winds over the eastern tropical Pacific that forms the Choco jet (except INMCM4 model). In addition, AMIP models show a better representation of the Choco jet than Best models. Likewise, Best models exhibit a better simulation of the Choco jet than Worst models.

2.3.3.1 Annual cycle

Best models (PCC of 0.83, RMSE of 1.52 m s^{-1} and Nash of 0.22) exhibit a better simulation of the annual cycle of the Choco jet in comparison to Worst models (PCC of 0.46, RMSE of 5.32 m s^{-1} and Nash of -3.67). On the other hand, each AMIP model overcomes its CMIP counterpart. Worst models locate the Choco jet further south during the entire year, inducing negative biases in zonal wind north of the equator (Fig. 2.3a). Previous studies indicate that models included in the Worst group locate the Pacific ITCZ further south of its real position during boreal winter and spring; also, these models exhibit strong biases simulating the inter-hemispheric SST and precipitation gradient over the eastern tropical Pacific during these seasons (Li and Xie 2014, Sierra et al. 2015). These biases may contribute to the anomalous southward location of the Choco jet simulated by Worst models, by reducing temperature/pressure differences between the Ecuador-Peru cold tongue region and western Colombian coast.

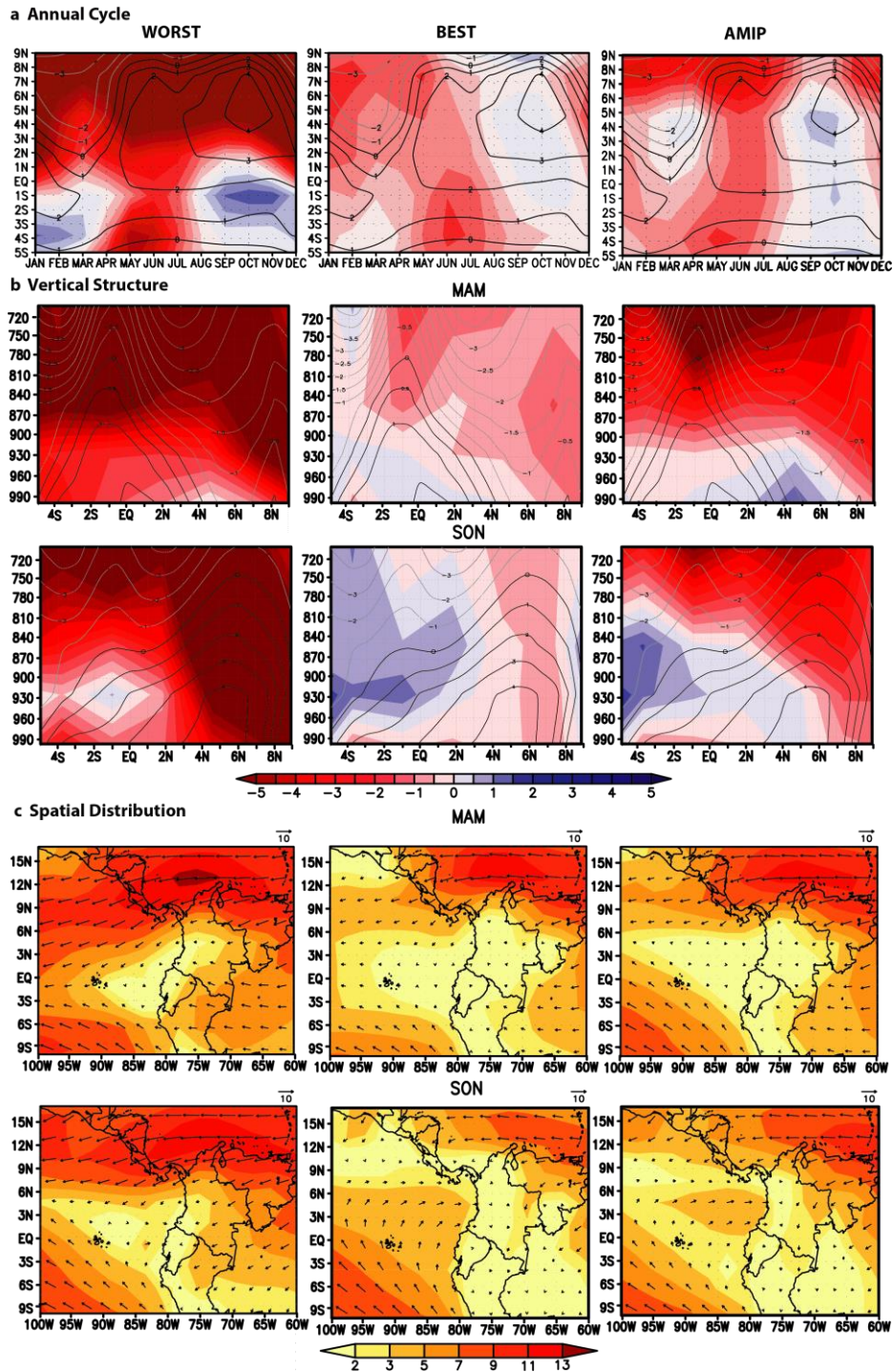


Fig. 2.3 Differences between Worst, Best and AMIP groups simulations respect to ERA-Interim reanalysis for the basic features of the Choco jet. **a** Annual cycle differences of the Choco jet (zonal winds at 925-hPa zonal winds and 80°W). **b** Vertical structure differences of the Choco jet (zonal wind) at 1000-700 hPa and 80°W during MAM and SON. **c** Seasonal climatology for horizontal winds (vectors) and wind magnitude (shading) at 925 hPa during MAM and SON. Wind differences and magnitudes are in m/s. In a and b, black solid (grey dashed) contours indicate positive (negative) zonal wind climatology from ERA-Interim

Best models simulation exhibits a Choco jet located slightly south respect to observations during May-July. The latter causes negative biases in zonal winds between 4°N and 8°N during these months (Fig. 2.3a). However, the jet reaches a further north position (10°N) in Best models during September-November, explaining the positive biases of zonal wind detected in these models (Fig. 2.3a). In addition, zonal wind differences between Best models and reference reanalysis indicate a biased southward migration of the jet during October-December, explaining the negative biases shown by simulations during these months; in observations instead, this southward migration starts in December. Best models also underestimate the jet velocities between December-July. Furthermore, Best and AMIP models share common biases: (i) a southward migration of the Choco jet starting in October instead of December and (ii) slower than observed Choco jet winds during six months, suggesting that the misrepresentation of this latitudinal migration is associated to the model atmospheric component (Fig. 2.3). Recent studies demonstrate that both AMIP and CMIP models of the CMIP5 project exhibit the double ITCZ bias (Li and Xie 2014). In this sense, an anomalous southward migration of the ITCZ, as occurring in GCMs with double ITCZ bias during boreal winter and spring, could lead to an anomalous southward migration of the Choco jet, explaining these errors in both AMIP and CMIP models. We discuss this idea in section 2.3.5.

2.3.3.2 Vertical structure

Model simulation of the jet vertical structure varies with season. Our results suggest it is more difficult for all models to correctly reproduce the jet vertical structure during SON and MAM than in DJF (not shown). Worst models overestimate the EMTEJ winds during all seasons, explaining the negative biases in zonal wind above 850 hPa (Fig. 2.3b). This

overestimation of the easterly winds could be linked to a poor representation of the topography over northern South America (sections 2.3.3.3 and 2.3.4). Therefore, Worst models present a shallower Choco jet during the whole year, especially during boreal summer and fall (Fig. 2.3b). The anomalous southern position of the jet simulated by Worst models causes a negative bias in zonal winds at shallower pressure levels, between 2°N-9°N, during all seasons. Conversely, Best models perform a better representation of the Choco jet intensity and depth throughout the year. Although Best models are able to reproduce the increase of the jet depth during SON, as observed in ERA-Interim (Figs. 2.1c-d), their simulated jet is still too shallow, as indicated by the negative biases in Fig. 2.3b. This slightly shallow jet occurs during MAM and JJA and is also observed in AMIP models.

2.3.3.3 Spatial distribution

In spite of the latitudinal amplification and migration of the Choco jet through the year, this jet enters to the continent north of the equator during all seasons (Figs. 2.1 e-h). Best and AMIP models are able to properly simulate the latitudinal range of the jet entrance to South American land mass. However, Worst models simulate this entrance further south during DJF and SON. During the other seasons, these models simulate easterly winds instead. In the same way, Worst models overestimate northerly winds over the tropical eastern Pacific Ocean and underestimate the southerly winds during all seasons (Fig. 2.3-c). This result is in agreement with a further southward ITCZ in simulations by these models, as identified in previous studies (Li and Xie 2014, Sierra et al. 2015). Best and AMIP models show a closer representation of the surface horizontal wind magnitude and distribution over the tropical eastern Pacific Ocean. Even in some seasons (JJA and SON), Best models overcome AMIP

models in simulating the horizontal wind over this region (Fig. 2.3-c). During JJA, Best and AMIP models present weaker winds entering to the continent, causing an underestimation of the Choco jet intensity in these months (Figs 2.3a, 2.4b).

2.3.4 Representation of the mechanisms involved in the dynamics of the Choco jet

As discussed in the Introduction, the Choco jet is the result of several interacting factors. Particularly, the topographic lifting of the air masses transported by the jet, and the SST and SLP differences between three particular regions, are important to determine the jet activity (Poveda and Mesa 2000, Poveda et al. 2014). These three regions are western Colombia (Colom; 75°W-77.5°W, 2°N-8°N), Colombian Pacific coast (ColPac; 77.5°W-82°W, 2°N-8°N), and Niño 1-2 region (10°S-0°, 90°W-80°W) (Fig. 2.4a). Thus, we assess how the CMIP5 GCMs represent these surface air temperature and SLP differences, as well as the orography of the Andes in northern South America, in order to understand their biases simulating this low-level jet.

2.3.4.1 Local topography

The sharp topography of the Andes is an important feature that influences climate and meteorological phenomena in the region. It shapes the distribution of precipitation in several areas of South America (Garreaud et al. 2009) via channeling the low-level circulation that carries moisture into the continent (Insel et al. 2010). In this sense, the topography of South America is also important to determine the spatial distribution of the low-level winds. For instance, in a recent work based on modelling experiments, Saurral et

al. (2015) demonstrate the Andes play a crucial role in shaping moisture fluxes over South America during the whole year. In particular, they find the South American low-level jet is simulated by models only when Andes topography is considered; moreover, simulations with no Andes indicate that precipitation is significantly reduced over the Pacific coast of Colombia, whereas when the Andes height is doubled, precipitation increases in the same region. In order to identify a relationship between local topography representation and the simulation of the basic features of the Choco jet, we use land topography information from the ETOPO 1 as reference data. In this sense, the RMSE and bias metrics are calculated for all models over the domain 10°S - 12°N and 60°W - 85°W . Since bias is defined as the mean error, this estimator can mislead conclusions when negative and positive errors are averaged. Despite this possible error, this measure of bias gives useful information when there is a clear trend in models to overestimate or underestimate the assessed field.

RMSE and bias in topography representation for each model are summarized in Table 2.1. In general, CMIP5 models underestimate the northern Andes height and overestimate the surroundings lowlands (see supplementary material), resulting in a misrepresentation of the topographic zonal gradient, as described by Saurral et al. (2015). Worst models exhibit the highest RMSE (Table 2.1). Despite the fact that Best models do not exhibit the more realistic representation of the Andes, they certainly overcome Worst models. In addition, there is not a direct link between horizontal resolution and the quality of topography representation since models with relatively coarse resolution can present low RMSE and vice versa (Table 2.1). Similarly, although the Choco jet is a local feature, models with finer horizontal resolution do not necessarily exhibit a better simulation of this jet. However, Best models have a finer horizontal resolution than Worst models, suggesting

that finer grid sizes could improve the model representation of the Choco jet, although it does not entirely rely on model grid size.

2.3.4.2 Local surface temperature and SLP gradients

To identify how CMIP5 models simulate Choco jet activity, Fig. 2.4b shows the annual cycle of the Choco jet index according to ERA-Interim reanalysis and model simulations. The Choco jet index is defined as the 925hPa zonal wind at 80°W averaged in the range 5°S-7°N (Poveda and Mesa 2000). As discussed in previous sections, ERA-Interim presents an annual cycle with minor activity during February-March and maximum velocities during October (Fig. 2.1). Due to the anomalous southward location of the Choco jet showed by Worst simulations (Fig. 2.3), their jet index is negative during the entire year (Fig. 2.4b), indicating a prevalence of the trade winds. All models underestimate the relative peak of the jet index between May, June and July, suggesting that this error comes from the atmospheric component of the GCMs.

To link the biases exhibited by model simulations to their representation of local surface temperature and SLP, Figs. 2.4c-h show the annual cycles of surface temperature and pressure differences between the key regions of the Choco jet. These annual cycles are unimodal, with a single peak during September and a minimum gradient in March for temperature and an opposite pattern for the SLP. This is consistent with the timing of the maximum and minimum activity of the Choco jet (Poveda and Mesa 2000). The amplitude of the surface temperature cycles, as observed from ERA-Interim, is higher than suggestions by previous studies based on NCEP-NCAR reanalysis (Poveda and Mesa 2000). Best and AMIP models are able to represent the annual cycle of temperature differences between regions Colom and Niño 1-2, although they show issues simulating the

minimum temperature difference. Worst models underestimate this temperature difference during the whole year (Fig. 2.4f). For Colpac-Niño1-2 difference, Best and AMIP models show a more adequate simulation of the annual cycle of temperature differences between regions. Best models underestimate the temperature difference between August-December. Again, Worst models strongly underestimate the amplitude of the cycle, especially between April-January (Fig. 2.4h). AMIP models exhibit an adequate representation of the amplitude of this annual cycle, as expected, due to the nature of their oceanic surface air temperature data (Fig. 2.4h). Finally, all model groups misrepresent the annual cycles of surface temperature and SLP differences between Colom and Colpac regions. Models simulate a bimodal pattern while observations exhibit a unimodal cycle (Fig. 2.4g-d). The fact that GCMs are able to simulate the existence of the Choco jet but not the annual cycle of temperature and SLP differences between Colom and Colpac regions suggest that these sea-land gradients could be less important to explain the existence of the jet than differences among other regions. The underestimation of temperature and pressure differences between Colom-Niño1-2 and Colpac-Niño1-2 by Worst models is consistent with an anomalously southward ITCZ and a warmer-than-observed southeastern Pacific, what causes the southward location of the Choco jet observed in these models.

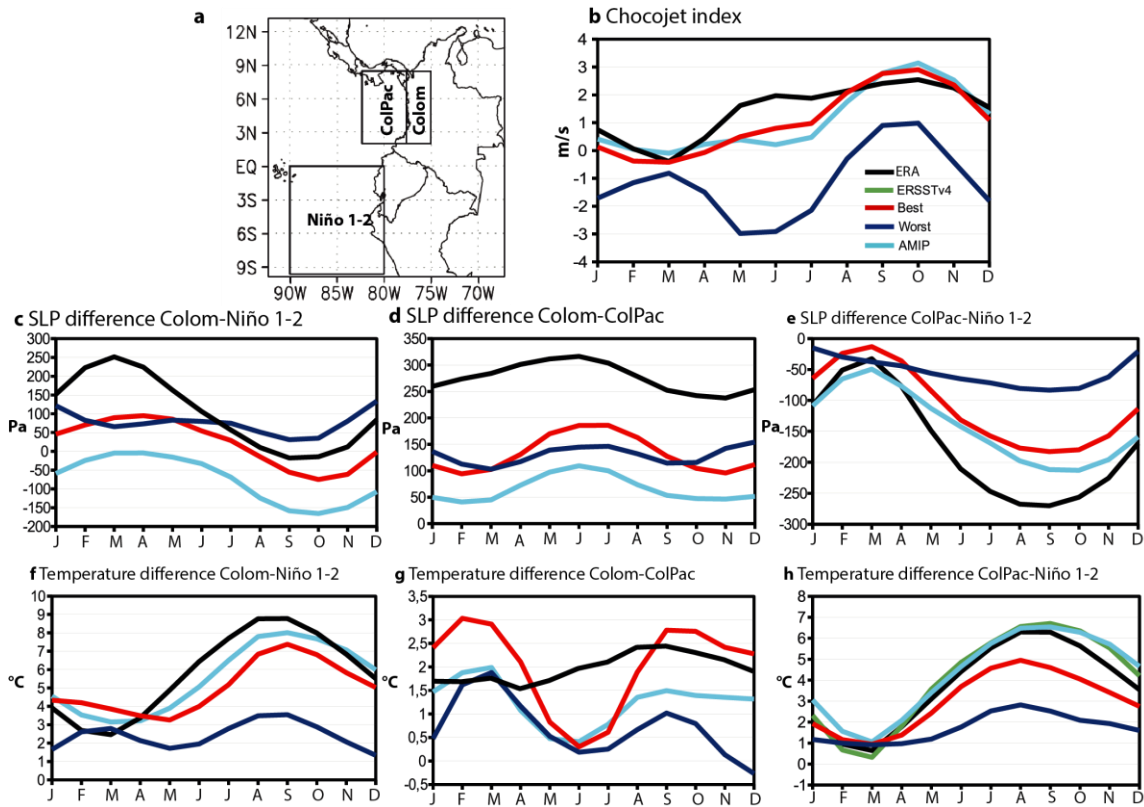


Fig. 2.4 Representation of the mechanisms involved in the Choco jet by Worst, Best, and AMIP models. **a** Regions selected to compute temperature and sea level pressure differences (based on Poveda and Mesa 2000). **b** Annual cycle of the Choco jet index. Annual cycle of regional differences of **c-e** SLP and **f-h** temperature at 1000hPa

2.3.5 Connection between ITCZ and Choco jet location biases

As mentioned in previous sections, recent works identify that models included in our “Worst group” locate the Pacific ITCZ erroneously south of its real position during DJF and MAM, as well as exhibit biases simulating the inter-hemispheric SST and precipitation gradient over the eastern tropical Pacific during the same seasons (Li and Xie 2014, Sierra et al. 2015). Worst models also exhibit a further southward location of the Choco jet over the entire year (sections 3.3-3.4). The Choco jet emerges from the eastward deviation of the southerly winds over the eastern tropical Pacific, which are part of the Hadley circulation. Thus, in this section we look for a relationship between the Choco jet and ITCZ latitudinal

migration in seasonal and interannual time scales, in order to show that an anomalous southward location of the ITCZ by model simulations can lead to a further southward position of the Choco jet.

On millennial and longer time scales, the ITCZ suffers shifts in its position causing precipitation and temperature changes over tropical regions (Wang et al. 2004). Paleoclimate records, observational data, and modeling simulations indicate that the mean position of the ITCZ is driven by changes in the atmospheric energy balance (Broccoli et al. 2006). On interannual and seasonal time scales, the meridional position of the ITCZ depends on both the cross-equatorial atmospheric energy transport and the atmospheric net energy input (Bischoff and Schneider 2016). In particular, seasonal ITCZ shifts are controlled by inter-hemispheric solar heat differences and are linked to the cross-equatorial atmospheric energy transport (Donohoe et al. 2013).

In order to track the meridional movement of the eastern Pacific ITCZ, we follow the methodology proposed by Adam et al. (2016). The latitude of the ITCZ is calculated using the area-weighted precipitation P , zonally averaged among 80° - 85° W, integrated in a range of latitudes (φ_1 and φ_2), and through a weighting function relying on an integer power N :

$$\varphi_E = \frac{\int_{\varphi_1}^{\varphi_2} \varphi [\cos(\varphi) P]^N d\varphi}{\int_{\varphi_1}^{\varphi_2} [\cos(\varphi) P]^N d\varphi} \quad [2.1a]$$

The choice of different values for φ_1 , φ_2 and N yield different ITCZ latitude indices.

Following Adam et al. (2016), we use φ_{max} and φ_{cent} indices, defined as:

$$\begin{aligned} \varphi_{max} \{N = 10, \varphi_1 = 20^\circ S \text{ and } \varphi_2 = 20^\circ N \\ \varphi_{cent} \{N = 1, \varphi_1 = 20^\circ S \text{ and } \varphi_2 = 20^\circ N \quad [2.1b] \end{aligned}$$

The ITCZ is tracked using all precipitation datasets considered here. While φ_{max} is equivalent to track the precipitation maximum, this index reduces the noise observed when the precipitation maximum is directly identified (Adam et al. 2016). Moreover, φ_{cent} is the tropical precipitation centroid and describes a precipitation median (φ_{med}), an equivalent index that has been used in previous works (Adam et al. 2016). For tracking the Choco jet meridional location, we use the latitude of the maximum zonal wind at 925hPa, at 80°W and between 15°S-15°N.

Figure 2.5a shows the latitude anomalies of the position of the ITCZ and the Choco jet from ERA-Interim. The coupling between ITCZ and the Choco jet is evident (PCC of 0.50, statistically significant at $p < 0.05$). In particular, during strong El Niño years such as 1982-1983 and 1997-1998, there is a clear ITCZ southward migration, consistent with previous studies (Rasmusson and Carpenter 1982, Russell and Johnson 2007). We get consistent results for the rest of observed precipitation datasets (not shown). In association with the movement of the ITCZ, the Choco jet migrates southward during strong El Niño years. Taking into account that AMIP models include observed SSTs, and therefore the ENSO signal, we assess the models ability to simulate the migration of the ITCZ and the response of the Choco jet (Figure 2.5b). Although AMIP models underestimate the anomalous movement of the ITCZ, these models are able to represent the ITCZ southward position during El Niño events, and the responses on location of the Choco jet (PCC of 0.52, statistically significant at $p < 0.05$).

The annual cycles of the meridional migration of the ITCZ and the Choco jet observed in reference datasets and simulations are shown in Fig. 2.5c and 2.5d, respectively. The ITCZ follows an annual migration with further south (north) position during boreal winter-spring

(summer-autumn), driven by the inter-hemispheric solar heat differences. AMIP and Best models adequately locate the ITCZ throughout the year. However, Worst models simulate the ITCZ around 5° further south of its real position during all months. Choco jet presents a similar annual cycle but its location is always south of the ITCZ, as shown in models and observations. Again, AMIP and Best model simulations are closer to the real position of the jet, but the last group locates the jet further south between June-August. The Choco jet simulated by Worst models, as well as their simulated ITCZ, is located further south respect to observations, especially during June-December (Fig. 2.5d). Scatterplot of the Choco jet annual cycle (Fig. 2.1a) PCC respect to ERA-Interim, and the eastern ITCZ annual cycle PCC respect to TRMM allow us to identify the relationship between the representation of the annual cycle of the ITCZ and the Choco jet locations. In general, models with a better representation of the annual cycle of the ITCZ position present a closer simulation of the Choco jet location throughout the year, as observed from Best models (except HadGEM2 models, which exhibit low values of the ITCZ PCC). On the other hand, Worst model have the lowest PCC for the annual cycles of both ITCZ and Choco jet locations.

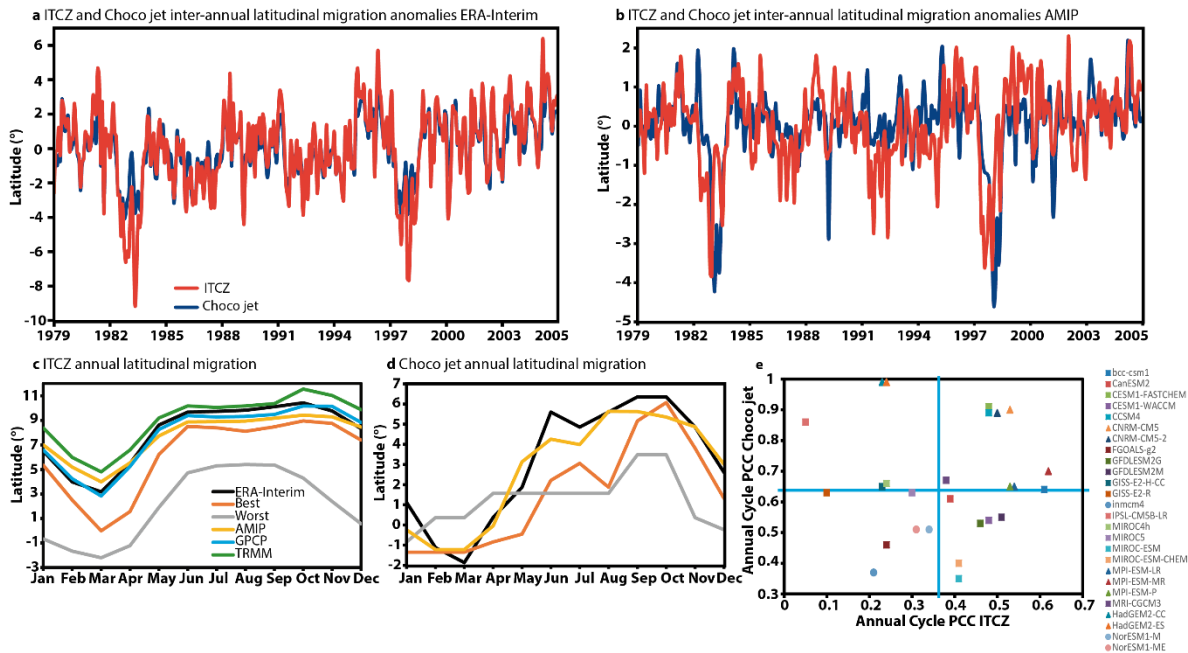


Fig. 2.5 Latitudinal position anomalies of the eastern Pacific ITCZ and the Choco jet in **a** ERA-Interim and **b** AMIP models. Climatological annual cycle of the meridional migration of the **c** ITCZ and **d** the Choco jet by observations and model groups. **e** Scatterplot of Choco jet annual cycle PCC (respect to ERA-Interim) and zonally mean (85-80°W) ITCZ annual cycle between 5°S-12°N PCC (respect to TRMM). Blue solid lines correspond to the inter-model mean for the Choco jet and ITCZ PCCs. Circles represent Worst group models. Triangles show Best group models

To explore the possible causes of the biases in the ITCZ and Choco jet meridional position, Fig. 2.6 presents ERA-Interim SLP gradient in JJA and SON, and SLP gradient differences for all model groups. In general, the observed pressure gradient is oriented from mid-latitudes to the tropics, towards the ITCZ over the Pacific and Atlantic oceans (Fig. 2.6a). Over the continents, however, there are large errors in this gradient, mainly in regions with high topography. Worst models simulate an anomalous southward pressure gradient among 5°-15°N in the eastern tropical Pacific (Fig. 2.6b). This bias, which occurs in these models during the whole year though stronger during JJA and SON, helps to explain their further southward location of the ITCZ. Worst models also underestimate the northward pressure gradient observed between the equator and 5°N during boreal summer and fall. Although

Best and AMIP models also underestimate the northward pressure gradient in this latitudinal fringe during SON, their error magnitudes are smaller than Worst models.

Biases in the surface pressure gradient observed in Fig. 2.6 could be related to errors in the simulation of the inter-hemispheric temperature asymmetry over the tropics. To identify this link, Table 2.2 summarize the inter-hemispheric asymmetry index over eastern tropical Pacific, defined as the area-averaged surface air temperature difference between north (0°-20°N, 120°-80°W) and south (20°S-0°, 120°-80°W) of the equator. The annual cycle of the solar radiation from ERA-Interim and ERSST data shows larger heating north of the equator during boreal summer and fall, and lower during boreal winter and spring. All model groups are able to simulate the annual cycle of the inter-hemispheric temperature difference, but Worst models underestimate the asymmetry during the year, which is consistent with a larger double ITCZ bias due to an overestimated Southern Hemisphere heating. By contrast, Best models are closer to observations but also underestimate the temperature asymmetry index during DJF-MAM (especially the CNRM models).

Table 2.2 Inter-hemispheric temperature asymmetry index (°C), defined as the difference between the area-averaged surface air temperature north (0-20°N, 120°-80°W) and south (0-20°S, 120°-80°W) of the equator over the eastern Pacific. The index is computed considering a 1979-2005 climatology

Dataset/Model Group	DJF	MAM	JJA	SON
ERA	1.54	1.40	3.61	4.01
ERSST	2.32	1.90	4.22	4.75
Worst	0.26	0.27	2.75	2.96
Best	0.55	0.34	3.17	3.48
AMIP	1.88	1.59	3.85	4.30

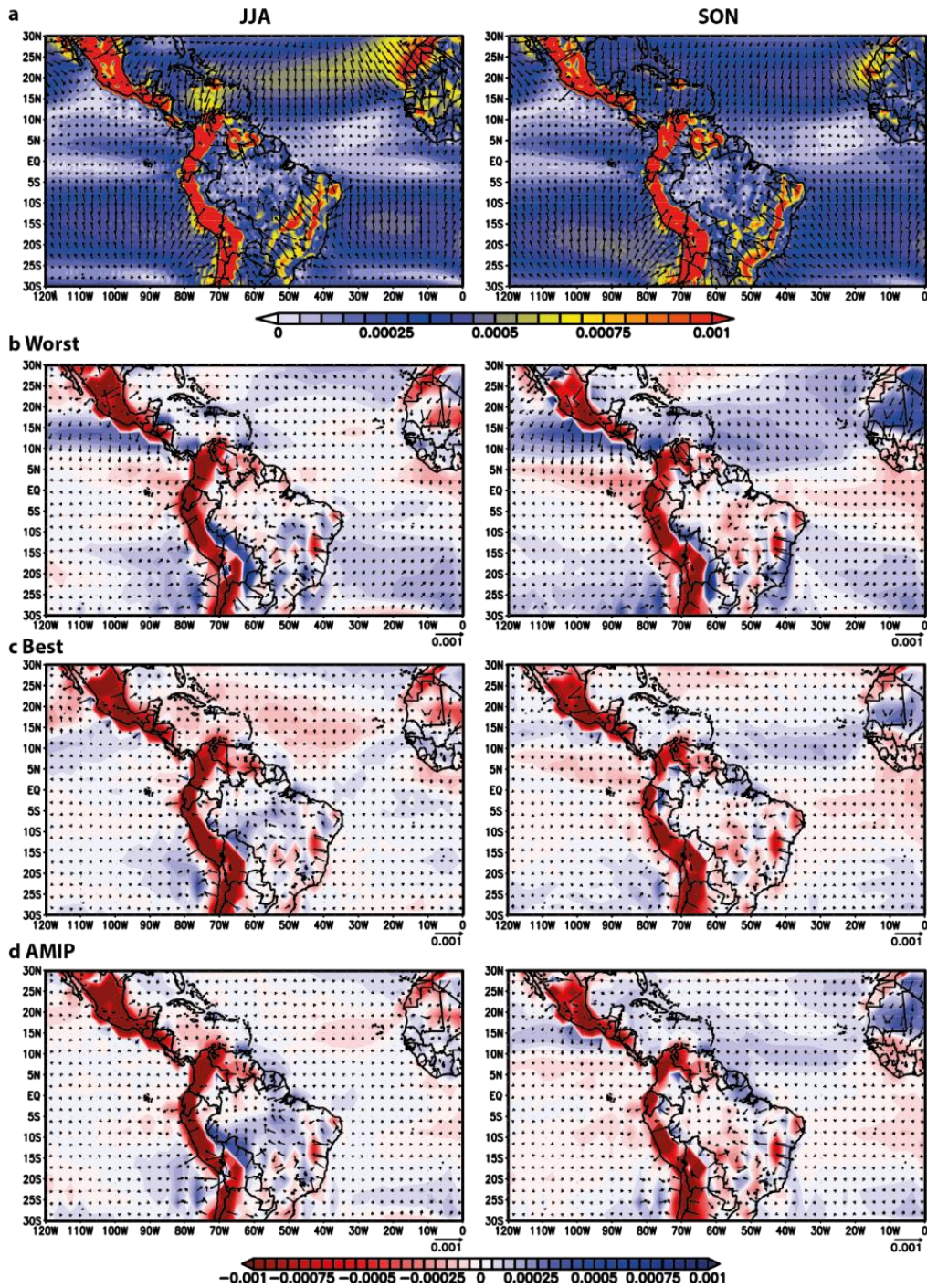


Fig. 2.6 a SLP gradient (vectors) and SLP gradient magnitude (shading) in ERA-Interim for JJA and SON. SLP gradient differences (vectors) and SLP gradient difference magnitude (shading) between: **b** Worst, **c** Best, **d** AMIP respect to ERA-Interim. Data in Pa*m-l

To further identify the double ITCZ bias in Best, AMIP and Worst models, we follow Hwang and Frierson (2013) and compute the global zonal precipitation mean and the inter-

hemispheric precipitation asymmetry (Fig. 2.7). Precipitation is higher north of the equator in the tropics for GPCP, AMIP and Best models (Fig. 2.7a). Conversely, Worst models present the north and south tropical precipitation similar in magnitude, or even exhibit higher rainfall values south of the equator (INMCM4, not shown) (Fig.2.7a). Thus, Best and AMIP models exhibit higher inter-hemispheric precipitation asymmetry indices than Worst models (Fig. 2.7b). Only two models included in the Best group (CNRM-CM5 and CNRM-CM5-2) show precipitation asymmetry indices close to Worst model values, as a response to an inverted inter-hemispheric temperature asymmetry index (not shown).

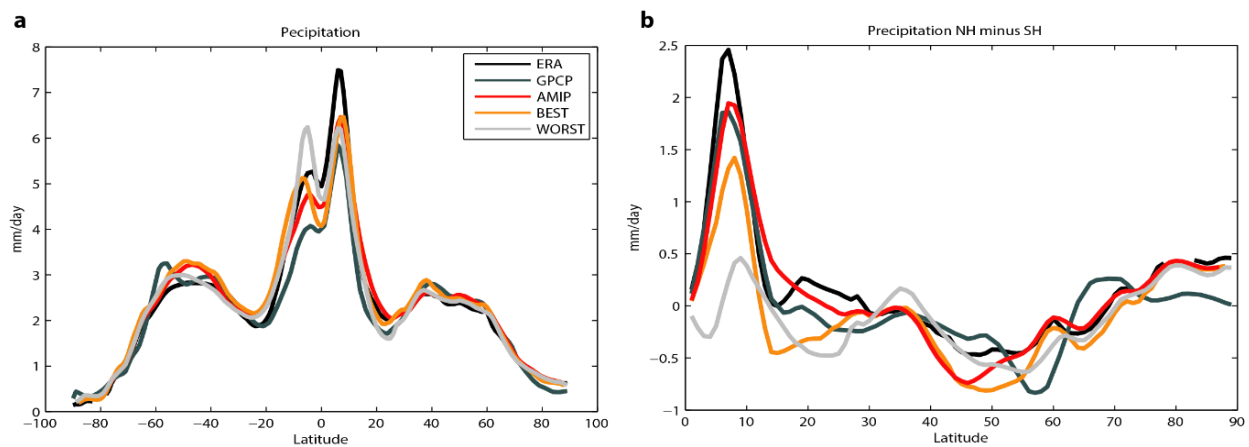


Fig. 2.7 Climatological zonal mean and inter-hemispheric asymmetry of precipitation. **a** Global zonally-averaged annual mean of precipitation. **b** Inter-hemispheric asymmetry (NH minus SH) of precipitation for Best, Worst, AMIP models and observations. Annual climatology is considered for the period 1979-2005

2.3.6 Relationship between the Choco jet and precipitation over northern South America

In order to identify the relationship between monthly rainfall anomalies and the Choco low-level jet exhibited by observations and GCM simulations, Figure 2.8 shows the correlation coefficient between these variables over northern South America. Following previous studies (Martin and Schumacher 2011, Sierra et al. 2015) we use rainfall and Choco jet

index anomalies to avoid spurious correlations associated to the seasonal cycle in both variables.

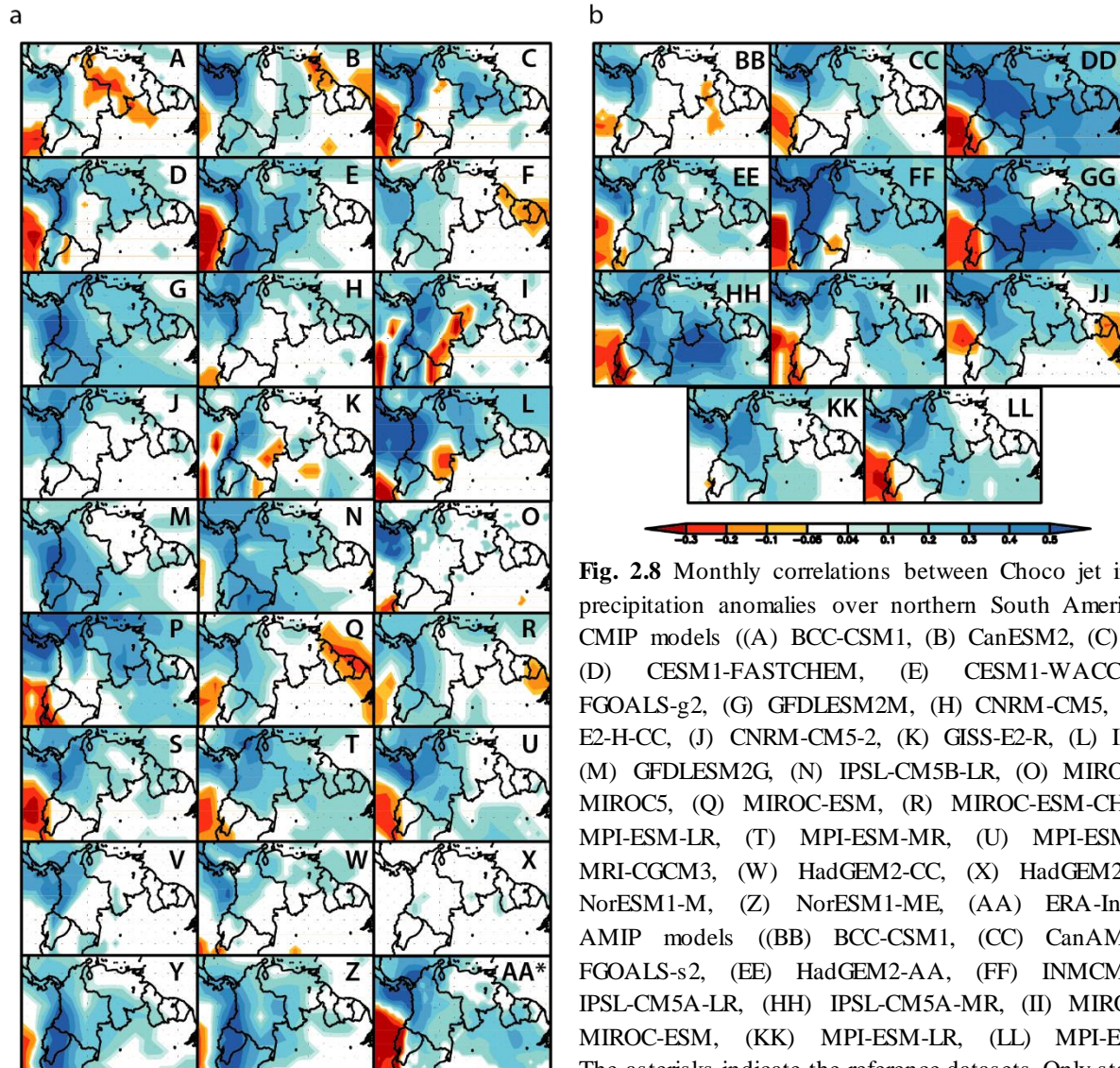


Fig. 2.8 Monthly correlations between Choco jet index and precipitation anomalies over northern South America for: **a** CMIP models ((A) BCC-CSM1, (B) CanESM2, (C) CCSM4, (D) CESM1-FASTCHEM, (E) CESM1-WACCM, (F) FGOALS-g2, (G) GFDLESM2M, (H) CNRM-CM5, (I) GISS-E2-H-CC, (J) CNRM-CM5-2, (K) GISS-E2-R, (L) INMCM4, (M) GFDLESM2G, (N) IPSL-CM5B-LR, (O) MIROC4h, (P) MIROC5, (Q) MIROC-ESM, (R) MIROC-ESM-CHEM, (S) MPI-ESM-LR, (T) MPI-ESM-MR, (U) MPI-ESM-P, (V) MRI-CGCM3, (W) HadGEM2-CC, (X) HadGEM2-ES, (Y) NorESM1-M, (Z) NorESM1-ME, (AA) ERA-Interim) **b** AMIP models ((BB) BCC-CSM1, (CC) CanAM4, (DD) FGOALS-s2, (EE) HadGEM2-AA, (FF) INMCM4, (GG) IPSL-CM5A-LR, (HH) IPSL-CM5A-MR, (II) MIROC5, (JJ) MIROC-ESM, (KK) MPI-ESM-LR, (LL) MPI-ESM-MR). The asterisks indicate the reference datasets. Only statistically significant correlations at 0.05 significance level are plotted

Positive (negative) correlations indicate that a stronger Choco jet is related to wetter (drier) conditions in those regions. ERA-Interim presents positive correlations over western and northern Colombia, the easternmost north equatorial Pacific, north of Brasil and the southern part of Venezuela. On the other hand, this reanalysis presents negative correlations over western Ecuador and the southeastern tropical Pacific because a stronger Choco jet

implies an enhanced moisture advection from these regions towards the Choco jet region. This dipole pattern is well simulated by some models (CCSM4, CESM1-FASTCHEM, CESM1-WACCM, MPI-ESM-LR, MPI-ESM-MR, MPI-ESM-P, MIROC5). Other models exhibit erroneous negative correlations inside the continent (MIROC-ESM-CHEM, MIROC-ESM, GISS-E2-R, GISS-E2-H-CC, FGOALS-s2, BCC-CSM1, CanESM2) or only positive correlations over most of the region (GFDLESM-2M, CNRM-CM5, GFDLESM-2G, IPSL-CM5B-LR, MIROC4h, MRI-CGCM3, HadGEM2-CC, NorESM-1M, NorESM-ME). In general, AMIP models exhibit a better representation of the rainfall-Choco jet relationship, with some exceptions (BCC-CSM1, MIROC-ESM, MPI-ESM-LR). Worst models present a non realistic representation of this relationship over the region, however only three of the Best models exhibit a well represented dipole pattern, what implies that a good representation of the basic features of the Choco jet climatology do not involve a good representation of all properties of the Choco jet.

2.3.7 Observed and simulated interannual variability of the Choco jet

The interannual variability of the Choco jet is modulated by ENSO through a reduction in the temperature gradient between Colombian Pacific coast and Niño 1+2 region during El Niño events (Poveda and Mesa 1999). However, there are other large-scale phenomena that can modify the eastern Pacific Ocean SSTs, and therefore generate changes in the velocities of the Choco low-level jet. The North Atlantic SST long term oscillation, known as the Atlantic Multi-decadal Oscillation (AMO), presents a 65-80 year cycle and has impacts on global climate (Kerr 2000, Ting et al. 2011). Long term variations in North Atlantic SSTs are positively correlated with SSTs in most of the northern Pacific and negatively correlated with SSTs over the central and western tropical Pacific and in the

eastern south tropical Pacific (Enfield et al. 2001). In the same way, the Pacific SSTs exhibit a long-term oscillation with 20-30 year cycle of ENSO like features in SST, surface pressure and wind stress fields (Zhang et al. 1997). Fig 2.9 shows the time series of Choco jet index anomalies, Niño3.4 SST anomalies, PDO and AMO indices. PDO and AMO indices are obtained from the National Oceanic & Atmospheric Administration (NOAA) web page <https://www.esrl.noaa.gov/psd/data/climateindices/list/>. The AMO index is defined as the ten-year running mean of detrended SSTs anomalies north of the equator (Enfield et al. 2001), and the PDO index is calculated from the leading PC of monthly SST anomalies in the North Pacific Ocean (Zhang et al. 1997, Mantua et al. 1997). Since NCEP-NCAR reanalysis provides data from 1948 to present, we consider this dataset to identify possible long-term variability in the Choco jet.

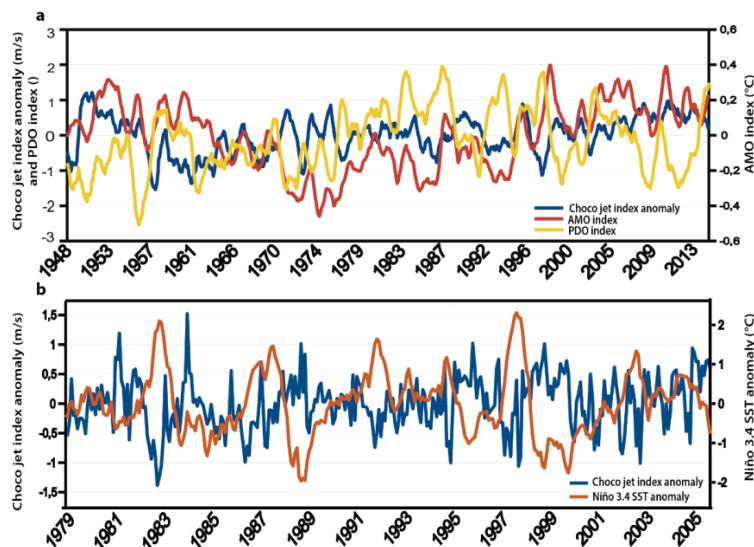


Fig. 2.9 Time series for: **a** Choco jet index anomalies from NCEP-NCAR reanalysis, AMO and PDO indices from NOAA web page. All datasets smoothed with a 10-month running mean filter **b** Choco jet index and Niño3.4 SST anomalies from ERA-Interim

The opposite relationship between the Choco jet and ENSO is clearly presented in Fig. 2.9b, where the minor (major) activity of the Choco jet occurs during the strongest El Niño

(La Niña) years, such as the 1982-1983 (1988-1989) and 1998-1999 (1999-2000) events. A similar opposite relationship occurs between the Choco jet and PDO due to the alike SST and SLP patterns over the Pacific Ocean between PDO and ENSO events. Conversely, a direct relationship seems to occur between the Choco jet and the AMO. The AMO warm phase is related with a cooling over the south tropical eastern Pacific and a warming in front the Colombian Pacific coasts (Enfield et al. 1997) what could produce a major SST and pressure gradients leading to a strengthening of the Choco jet. An adequate analysis of this relationship requires however a longer period for the records of the jet. Table 2.3 illustrates the relationships between the Choco jet and the AMO, PDO and ENSO discussed above. Due to the high degree of serial correlation in the time series we use the effective sample size in the correlation test (Ebisuzaki 1997).

Table 2.3 Correlation coefficients between Choco jet index anomalies from different reanalysis and global climate indices from NOAA. Statistically significant correlations at 0.05 significance level are in bold

	CFSR	NCEP-DOE	ERA	NCEP-NCAR (1979)	NCEP-NCAR (1948)
AMO	0.266	0.143	0.227	0.149	0.137
PDO	0.003	-0.238	-0.068	-0.141	-0.188
Nino12	-0.128	-0.166	-0.145	-0.011	-0.106
Nino34	-0.238	-0.373	-0.337	-0.209	-0.303
Nino4	-0.150	-0.323	-0.288	-0.265	-0.296
MEI	-0.241	-0.423	-0.341	-0.286	-0.303

There are negative significant correlations between the Choco jet and the ENSO indices (except Niño 1+2 anomalies) for all reanalysis. Due to the similar SST pattern between PDO and ENSO events there are also negative correlations for the Choco jet and the PDO. This correlation is only statistically significant for the NCEP-NCAR reanalysis, probably because this reanalysis has a longer time period that covers around two cycles of the PDO (60 years). As we expected, there is a direct relationship (positive correlation) between

AMO and the Choco jet in all reanalysis due to SST anomalies linked to this phenomena over the Pacific Ocean. However, these correlations are not statistically significant for most of the reanalysis (except for ERA-Interim) probably because it is necessary a longer record for the Choco jet index to cover at least one entire cycle of the AMO.

In order to identify the dominant modes of variability in the Choco jet time series we use the Fast Wavelet Transform (Torrence and Compo 1998). Figure 2.10 shows the wavelet power spectrum of different observation datasets in the corresponding time period.

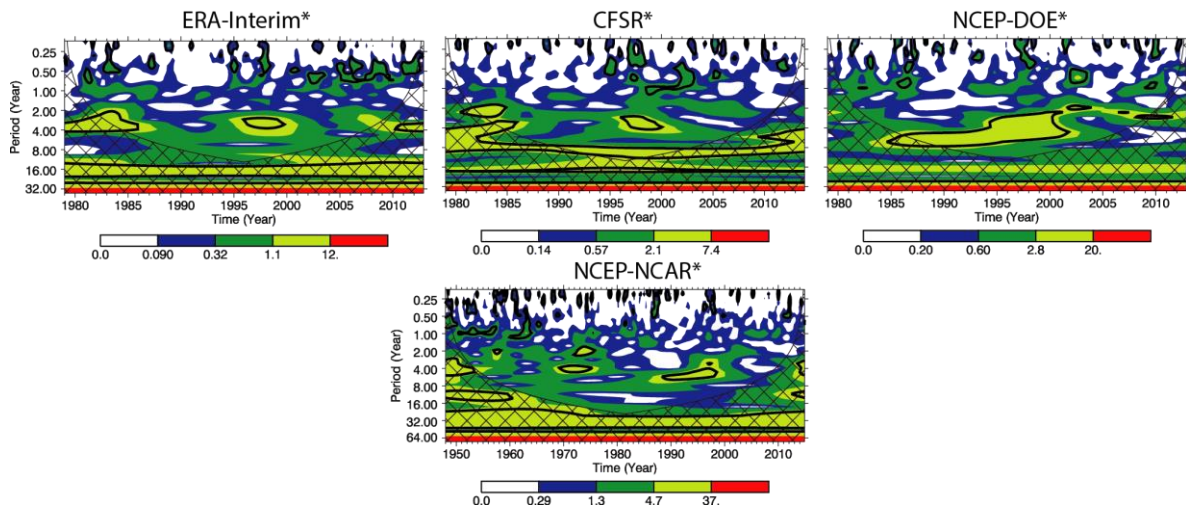


Fig. 2.10 Wavelet power spectrums for the Choco jet index anomalies in the corresponding time period for ERA-Interim, CFSR, NCEP-DOE and NCEP-NCAR. Spectra were obtained from <http://paos.colorado.edu/research/wavelets/>, based on Torrence and Compo (1998)

The ENSO signal in the Choco jet index time series is present in all datasets, with large variability linked to frequencies of 2-4 and 4-8 years. Therefore, there are important contributions to Choco jet variability during strong El Niño years such as 1972-1973 (NCEP-NCAR), 1982-1983 (CFSR and ERA-Interim) and 1997-1998 (all observation datasets). All reanalysis also exhibit strong spectral peaks associated with low frequencies

(16, 32 and 64 years) that contribute more to the total variability and are probably linked with the PDO and AMO. However, the contribution of the low frequency phenomena to the original Choco jet time series is still not clear and, it would be convenient to calculate the percentage of a power spectral band for 20-60 years in the time series.

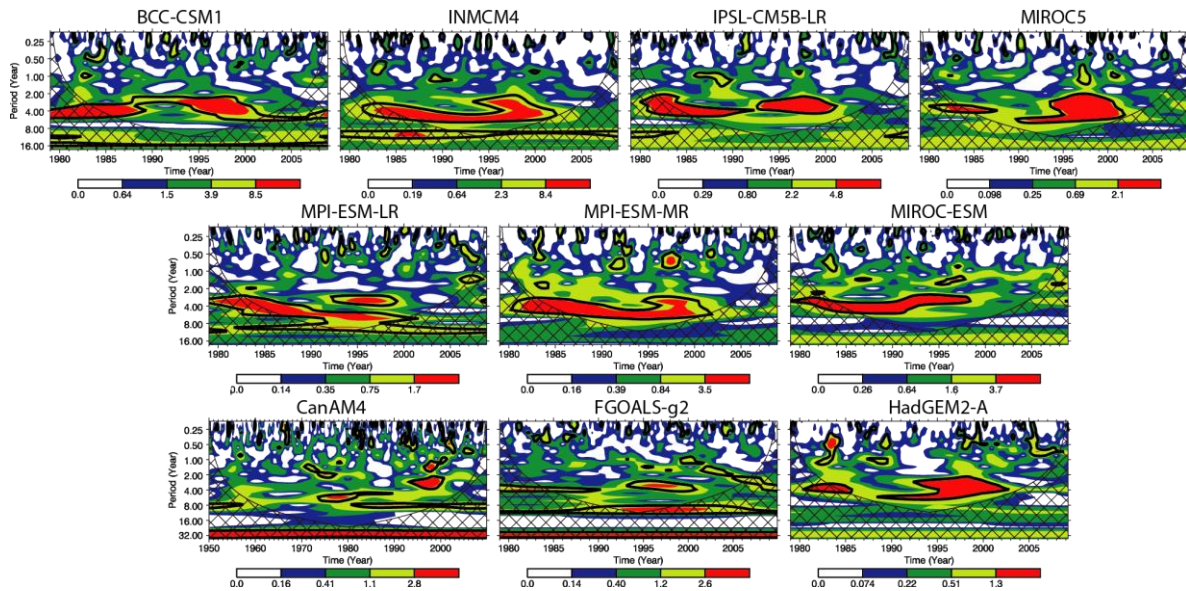


Fig. 2.11 Same as in Fig. 2.10, but for AMIP models

In the same way, we performed the Fast Wavelet Transform to the simulated Choco jet index anomalies for AMIP models. We find that all AMIP models can represent the ENSO signal in the variability of the Choco jet, with major contributions during strong warm events of this phenomenon (1982-1983 and 1997-1998). However, most of the AMIP models overestimate the variability linked to the ENSO and underestimate the importance of the variability in lower frequencies that is present in observations. This result suggests a less sensitive Choco jet to large-scale ocean-atmosphere phenomena (PDO and AMO) in AMIP models.

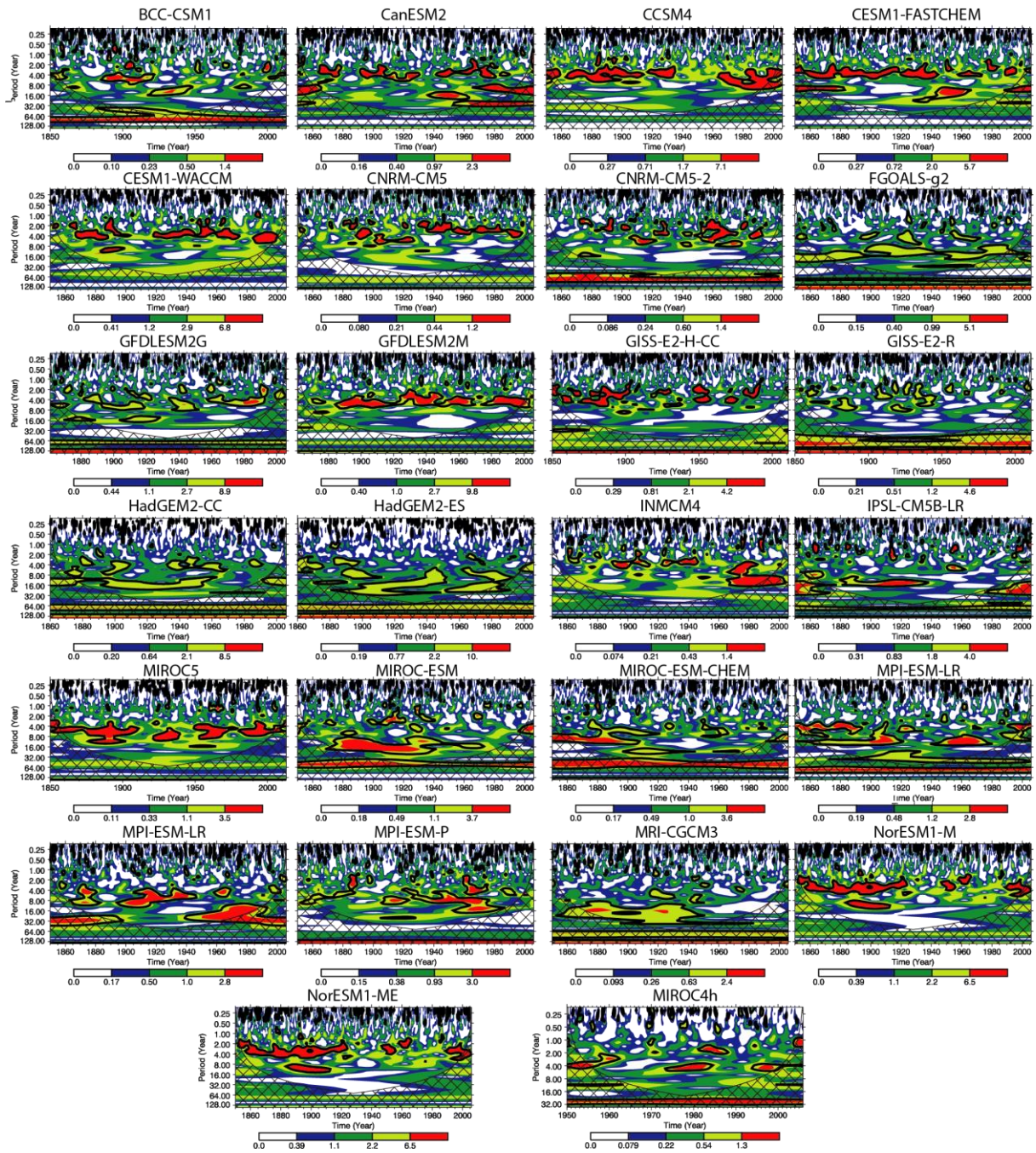


Fig. 2.12 Same as in Fig. 2.11, but for CMIP models

CMIP models also represent the influence of ENSO over the variability of the Choco low-level jet, but 11 GCMs present this phenomenon as the main director of the Choco jet variability. Most GCMs properly simulate the variability of the Choco jet linked to low

frequencies, 10 from the 26 models present the AMO frequencies (around 64-128 year) as the main contributor to the Choco jet variability and 5 models exhibit the PDO frequencies as the principal contributor (16-32 year cycle). It is important to remark that previous studies find that CMIP5 models present high prediction skill for the AMO index and low prediction skill for the PDO in the decadal simulations (Kim et al. 2012). However, other studies demonstrate that GCMs part of the CMIP5 project reproduce the basic features of the SST and SLP spatial patterns linked with the PDO, and the teleconnections with North America precipitation anomalies (Polade et al 2013, Sheffield et al. 2013). On the other hand, this generation of global climate models exhibits improvements in the representation of the ENSO compared to the CMIP3 models (Bellenger et al. 2014). CMIP5 models are also able to reproduce the ENSO-precipitation teleconnections over North America (Langenbrunner and Neelin 2013).

Although the signal of the ENSO is present in the simulated Choco jet index it is necessary to evaluate whether the relationship ENSO-Choco jet is represented realistically in GCMs. Thus, we compute the correlation between the Choco jet index anomalies and SST anomalies over Niño3 region (5°S - 5°N , 150°W - 90°W), as well as the correlation among these indices and the precipitation anomalies time series over the Colombian Pacific coast (2°N - 9°N , 80°W - 76°W) (Table 2.4). In general all models can adequately represent the opposite relationship between ENSO and the Choco jet, thus GCMs can simulate a weaker Choco jet when they simulate El Niño conditions and vice versa. Only BCC-CSM1, GISS-E2-R and MRI-CGCM3 exhibit problems in reproducing this relationship. On the other hand, GCMs are able to represent the direct observed relationship between the precipitation over western Colombia and the Choco jet (except HadGEM2-ES), this is, a stronger Choco

jet leads to a wetter conditions over the Colombian Pacific region (Poveda and Mesa 2000). There is no significant difference between AMIP and CMIP models, and between Best and Worst models, which means that a better representation of the climatological basic features of the Choco jet is not necessarily related with a better representation of the interannual variability and the relationship between the jet and the precipitation over the region.

Table 2.4 Correlation coefficients between Choco jet index anomalies, Niño 3.4 SST anomalies (5°S-5°N, 170°W-120°W), and precipitation anomalies over the Colombian Pacific coast (2°N-9°N, 80°W-76°W) from ERA-Interim and GCMs. AMIP models are identified with _A at the end

	Precipitation-Choco jet	ENSO-Choco jet
ERA-Interim*	0.66	-0.57
bcc-csm1_A	0.58	-0.29
CanAM2_A	0.56	-0.31
FGOALS-s2_A	0.66	-0.69
HadGEM2-A_A	0.58	-0.48
inmcm4_A	0.86	-0.60
IPSL-CM5A-LR_A	0.64	-0.62
IPSL-CM5A-MR_A	0.65	-0.67
MIROC5_A	0.34	-0.53
MIROC-ESM_A	0.44	-0.35
MPI-ESM-LR_A	0.47	-0.32
MPI-ESM-MR_A	0.44	-0.52
Bcc-csm1	0.42	0.02
CanESM2	0.68	-0.38
CESM1-FAS TCHEM	0.68	-0.48
CESM1-WACCM	0.57	-0.56
CCSM4	0.72	-0.56
CNRM-CM5	0.61	-0.34
CNRM-CM5-2	0.61	-0.28
FGOALS-g2	0.44	-0.13
GFDLES M2 G	0.605	-0.29
GFDLES M2 M	0.64	-0.35
GISS-E2-H-CC	0.48	-0.35
GISS-E2-R	0.48	-0.07
inmcm4	0.82	-0.22
IPSL-CM5B-LR	0.62	-0.18
MIROC4h	0.56	-0.26
MIROC5	0.34	-0.53

MIROC-ESM	0.42	-0.15
MIROC-ESM-CHEM	0.41	-0.24
MPI-ESM-LR	0.50	-0.38
MPI-ESM-MR	0.39	-0.41
MPI-ESM-P	0.54	-0.36
MRI-CGCM3	0.68	-0.06
HadGEM2-CC	0.54	-0.19
HadGEM2-ES	0.09	-0.33
NorESM1-M	0.59	-0.35
NorESM1-ME	0.63	-0.39
AMIP	0.57	-0.49
CMIP	0.54	-0.30
BEST	0.47	-0.33
WORST	0.68	-0.32

2.4 Discussion and Conclusions

This chapter explores the ability of 26 CMIP and 11 AMIP GCMs included in the CMIP5 archive to simulate the climatological basic features of the Choco low-level jet. AMIP models are used in order to identify whether model biases arise from their atmospheric or their oceanic component. Based on similar studies of different low-level jets, we consider three basic features of this jet: its annual cycle, its spatial distribution, and its vertical structure (section 2.3.1). In order to qualify the model simulation of these relevant aspects of the Choco jet, we use PCC and RMSE as model performance metrics. Some of these metrics may exhibit redundant information. Hence, factor analysis is used. An objective classification of GCMs based on their skill to exhibit a realistic representation of the Choco jet is done through cluster analysis (section 2.3.2). Three groups of models are identified, namely “Best”, “Worst”, and “Intermediate” models; however, our analysis is focused only on Best, Worst and AMIP models.

In spite of being a local atmospheric phenomenon, this study demonstrates that nearly all GCMs (except INMC4) can represent the inversion in the trade winds west of the northern South American Pacific coast that forms the Choco low-level jet. Although GCM horizontal resolution is generally coarser than 100km, we identify Best models exhibit a realistic simulation of the basic features of this jet. Conversely, Worst models exhibit some biases such as an anomalous southward location of the Choco jet during the whole year and a shallower jet. It is also important to remark that all AMIP models overcome their CMIP counterpart, which reflects the impact and importance of well-simulated SSTs on the representation of the Choco jet. However, Best and AMIP models present common errors, such as the underestimation of the jet intensity during December-July (especially between June-July) and a shallower jet during the entire year, suggesting the source of these errors arises from the atmospheric component of models. Independently of the differences between Best and Worst groups, all models represent the existence of the Choco jet. In this sense, a natural question that comes up is: Why are GCMs able to simulate a local feature such as the Choco jet? The model skill to represent the Choco jet comes from their ability to reproduce some of the main precursors of this jet (section 2.3.4). As we discuss in sections 2.1 and 2.3, the Choco jet is thought to be, among other processes, the result of the temperature and pressure differences between particular regions in the eastern Pacific and western Colombian lands. These temperature and pressure differences are not local features since they cover an area around 18° latitude and 15° longitude, what allows GCMs to represent them. Nevertheless, Worst models considerably underestimate the temperature and pressure differences between these key regions. On the other hand, all GCMs misrepresent temperature and pressure differences between western Colombia and the Colombian Pacific coast. The fact that GCMs can properly reproduce the Choco jet even

when they do not simulate these particular temperature and pressure differences suggest that these differences are not a determinant factor for the existence of the Choco jet. The latter suggests that temperature/pressure differences between the Niño 1.2 region and western Colombia landmass, as well as the inter-hemispheric temperature/pressure contrasts over the eastern tropical Pacific appear to be more important to determine the reversal of the southeasterly trades toward northern South America. However, the unrealistic representation of the temperature/pressure differences between western Colombia and the Colombian Pacific coast by GCMs could be related to a misrepresentation of the tropical rainforest over western Colombia due to erroneous representations of surface energy fluxes in the region, as observed over the Amazon forest (Yin et al. 2013). Although previous works have hypothesized the processes that explain the existence of this jet (Poveda and Mesa 2000), their relative importance on the genesis and variability of the Choco jet existence is not yet well understood.

Another important question that arises is: How could we improve the simulation of local low-level jets by GCMs? The connection between high horizontal resolution and a realistic simulation of some atmospheric variables and processes by GCMs has been pointed out by several studies (Oueslati and Bellon 2015, Gulizia and Camilloni 2015). The results discussed in section 2.3.4.1 suggest that finer grid sizes in GCMs could be related with a better representation of the basic features of the Choco jet. Particularly, Best models have a finer horizontal resolution than Worst models, suggesting that finer grid sizes could improve the model representation of this jet. We further explore this link between grid size and the quality of the Choco jet simulation by computing correlations between PCC and

RMSE of the basic features of the Choco jet and the model grid size. Only the most significant correlations are shown in Fig. 2.13.

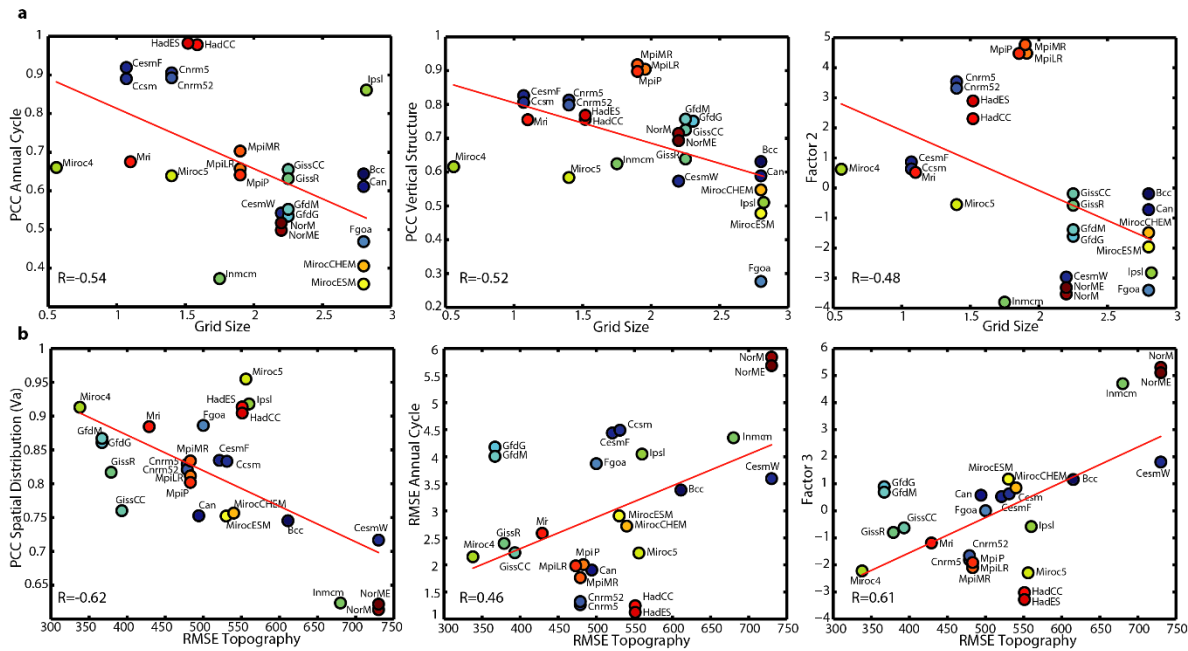


Fig. 2.13 a Scatterplot of grid size and PCC for annual cycle (left), vertical structure (middle), and the second factor obtained by Factor Analysis (section 2.3.2) (right). b Scatterplot of RMSE of topography and PCC of the spatial distribution of meridional wind (left), RMSE of annual cycle (middle), and the third factor (right). Correlation coefficients are shown in the lower left corner of each plot

Since grid size is defined by latitudinal and longitudinal resolutions, we average these dimensions in order to get a single value. As we expect, direct (inverse) relationship is found between grid size and RMSE (PCC), showing that the coarser the resolution, the higher (lesser) the RMSE (PCC) of the basic features of the jet. However, the correlation is statistically significant only for PCC of the annual cycle, the spatial distribution of the zonal winds, and the vertical structure of the jet (Fig. 2.13a). These features are all estimated using zonal winds, suggesting that in the region, a finer horizontal resolution could improve the simulation of the spatial pattern of the east-west component of the wind.

A significant correlation is also found between grid size and the second factor obtained from Factor Analysis (section 2.3.2), which explains around 14% of the total variance.

Similar results are obtained for the connection between topography simulation and the basic features of the Choco jet. In particular, high values of RMSE in topography are significantly associated with high RMSE in the annual cycle, the spatial distribution of the zonal wind, the magnitude of the horizontal wind, and the vertical structure, as well as with low values of the PCC of spatial distribution in meridional wind (Fig. 2.13b). RMSE in topography also shows significant correlations with the three factors of the basic features of the jet, suggesting that a better representation of the Andes height may improve the simulation of the basic features of the Choco jet. This could be related to a better simulation of the topographic lifting effect described by Poveda and Mesa (2000) and a better representation of the horizontal wind field in the region. In section 2.3.4.1, we find that all GCMs underestimate the northern Andes height and overestimate its neighborhood lowlands (supplementary material), generating a misrepresentation of the topographic zonal gradient, as described by previous works (Saurral et al. 2015). In accordance with the above results (Fig. 2.13b), Worst models exhibit the highest RMSE (Table 2.1). Best models do not exhibit the most realistic representation of the Andes but they certainly overcome Worst models. Besides, as we argue in section 2.3.4.1, there is not a direct link between horizontal resolution and the quality of topography representation. Recent works recognize that GCMs with resolutions coarser than 100km (most of CMIP5 GCMs considered in this work) are unable to represent the steep slopes of the Andes (Saurral et al. 2014). Hence, the relationship between resolution and topography is not evident since all GCMs used in this study (except MIROC4h) have resolution coarser than this limit value. In this sense, as

GCMs improve their horizontal resolution to values finer than 100km, their simulation of topography could improve, which could lead to a better representation of the basic features of the Choco jet.

However, as we discuss in section 2.3.5, a good representation of the Choco jet is also linked with a well-simulated eastern Pacific ITCZ. By tracking the latitudinal position of the ITCZ and the Choco jet core on annual and interannual time scales, we identify there is a coupling between these two atmospheric phenomena: when the ITCZ is located further south (during El Niño years), the Choco jet also migrates southward, and vice versa (Fig. 2.5). We demonstrate GCMs are able to reproduce this relationship and, thus, a misrepresentation on the position of the eastern Pacific ITCZ could lead to a biased simulation of the Choco low-level. Indeed, Worst models simulate the Choco jet further south during the entire year, because of an erroneous southern location of the eastern Pacific ITCZ (Fig. 2.5). This bias in the position of the rainy belt over the eastern tropical Pacific Ocean relates to an anomalous surface pressure gradient exhibited by Worst models during the whole year, pushing southward the oceanic ITCZ (Fig. 2.6). The anomalous pressure gradient is originated by a warm bias in the southern part of the eastern tropical Pacific Ocean and is closely related with the double ITCZ bias (Table 2.2). In fact, models included in our Worst group present a strong double ITCZ bias (Fig. 2.7) (Li and Xie 2014). The double ITCZ has been identified as the most significant and persistent bias of the GCMs (Hwang and Frierson 2013) and presents several different possible causes. Some studies relate the existence of the double ITCZ with warm SSTs errors in the coastal upwelling of Peru (Gordon et al. 2000), an underestimation of stratocumulus over the same region (Ma et al. 1996), and the insufficient cooling by ocean transients from the upwelling region (Colas et al. 2012). Additionally, several studies argue that errors in precipitation

over the tropics could be linked to errors outside the tropics, such as cloud biases over the Southern Ocean (Hwang and Frierson 2013) and a weaker-than-observed Atlantic Meridional Overturning Circulation (AMOC) (Wang et al. 2014). In particular, previous studies indicate that changes in some aspects of the convection scheme (Zhang and Wang 2006) or in the surface wind stress formulation (Luo et al. 2005) of GCMs could contribute to a reduction of their ITCZ bias. Our results suggest that reductions of the double ITCZ bias could lead to a better simulation of the basic features of the Choco jet. Therefore, reductions in cloud and AMOC errors observed in GCMs may enhance the representation of the temperature/pressure differences between the Ecuador-Peru cold tongue region and western Colombian coast and the latitudinal position of the ITCZ. The latter could contribute to a better representation of the location of the Choco jet, an important feature that influences climate and weather conditions over northern South America and Central America, considered among the most vulnerable regions under a climate change scenario.

Finally, in sections 2.3.6-2.3.7 we explore the GCMs skill to represent the interannual variability dominant modes of the Choco jet, as well as the interannual relationship with the precipitation over the region. The interannual variability of the Choco jet is mainly controlled by low frequency phenomena such as the PDO and AMO in all reanalysis. The ENSO signal also plays an important role in controlling the interannual variability of the Choco jet, with important contributions during strong El Niño years such as 1972-1973, 1982-1983 and 1997-1998 (Fig. 2.10). ENSO and PDO, due to the similar SLP and SST anomalies pattern over the Pacific Ocean, are negatively related to the activity of the Choco jet. Conversely, the Choco jet seems to be directly correlated with the AMO phase because during the warm phase of the AMO there is a cooling over the south tropical eastern Pacific

and a warming in front of the Colombian Pacific coast (Enfield et al. 1997) which could produce a major SST and pressure gradients leading to a strengthening of the Choco jet (Fig. 2.9 and Table 2.3).

AMIP models are able to represent the influence of the PDO, AMO and ENSO in the variability of the Choco jet, but in these models the last phenomenon is the principal director (Fig. 2.11). Similarly, CMIP models present the signal of these global scale atmospheric-ocean phenomena in the variability of the Choco jet, 11 models present ENSO as the dominant mode, 10 exhibit the AMO frequencies as the dominant mode, and 5 the PDO frequencies (Fig. 2.12). Most of the CMIP models (except BCC-CSM1, GISS-E2-R and MRI-CGCM3) and all AMIP models can adequately represent the opposite relationship between ENSO and the Choco low-level jet, which means that models are able to simulate a weaker (stronger) Choco jet during El Niño (La Niña) conditions (Table 2.4). In the same way, CMIP and AMIP models are able to properly represent the direct relationship observed between the Choco jet activity and the precipitation over the western part of Colombia. However, only some models (CCSM4, CESM1-FASTCHEM, CESM1-WACCM, MPI-ESM-LR, MPI-ESM-MR, MPI-ESM-P, MIROC5) are able to realistically simulate the spatial pattern of the relationship between the Choco jet index anomalies and the precipitation anomalies over the region. AMIP models present a better simulation of this pattern. As the selection of Best and Worst models is only based on the representation of the climatological features of the jet, Best and Worst models do not exhibit significant differences in their representations of the interannual variability of the Choco jet. Therefore, to explore the future projections of the Choco jet it would be suitable to use all GCMs and not only the models classified as Best.

2.5 Supplementary material

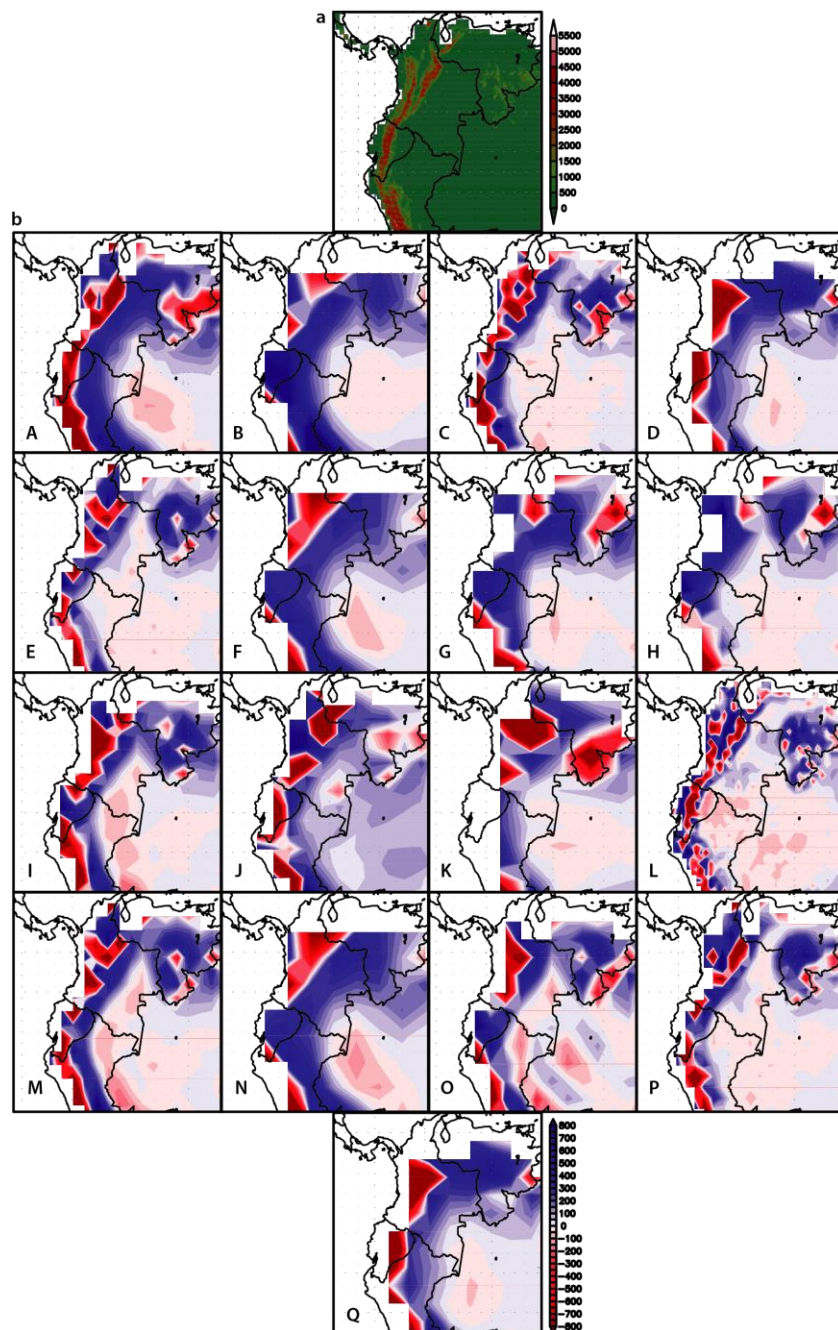


Fig. S2-1 **a** Topography of Colombia from ETOPO (A*). **b** Topography differences respect to ETOPO ((A) BCC-CSM1, (B) CanESM2, (C) CCSM4 and CESM1-FASTCHEM, (D) CESM1-WACCM, (E) CNRM-CM5 and CNRM-CM5-2, (F) FGOALS-g2, (G) GFDLESM-2M and GFDLESM-2G, (H) GISS-E2-H-CC and GISS-E2-R, (I) HadGEM2-CC and HadGEM2-ES, (J) INMCM4, (K) IPSL-CM5B-LR, (L) MIROC4h, (M) MIROC5, (N) MIROC-ESM and MIROC-ESM-CHEM, (O) MPI-ESM-LR, MPI-ESM-MR and MPI-ESM-P, (P) MRI-CGCM3, (Q) NorESM1-M and NorESM1-ME. Data in m

Chapter 3

The future of the Choco low-level jet

3.1 Introduction

The Colombian Pacific coast is an extremely wet place. With an annual mean precipitation between 8000 and 13000 mm, this region presents one of the rainiest places on the world and rivers with important runoff rates such as San Juan and Atrato Rivers (Poveda and Mesa 2000). The existence of this rainy place is partially explained by the presence of a low-level westerly circulation that enters from the Pacific Ocean, known as the Choco low-level jet. These surface winds advect moisture, and once in the continent, interact with the topography and the easterlies to induce the formation of Mesoscale Convective Systems in the region (Mapes et al. 2003, Zuluaga and Poveda 2004). At interannual time scale, this jet exhibits important variability linked to ENSO, strengthening (weakening) during La Niña (El Niño) events and transporting more (less) moisture to northern South America. As a consequence, during La Niña events the western and central parts of Colombia experiment positive rainfall anomalies; the opposite pattern occurs during El Niño years (Poveda et al. 2001, Ambrizzi et al. 2004). However, as we discuss in section 2.3.7, there are other large-scale phenomena with lower time frequencies that can modify the eastern Pacific Ocean SSTs and therefore, generate changes in the velocities of the Choco low-level jet. Our results suggest that, due to their similar pattern in SSTs and SLPs anomalies over the Pacific Ocean, ENSO and PDO are negatively related with the Choco jet while AMO presents a positive relationship (section 2.3.7). Indeed, recent studies identify an increasing

trend during the last decades in precipitation and average river discharges over the Pacific region, as a consequence of a strengthening of the Choco jet (Carmona and Poveda 2014), which could be related with the most recent shift of the PDO (Mantua and Hare 2002). On the other hand, proxy based studies suggest that during the Last Glaciation this surface circulation was stronger due to persistent La Niña-like conditions over the Pacific Ocean that turned western Colombia wetter (Martínez et al. 2003). Similarly, climate simulations with GCMs part of the Paleoclimate Modelling Intercomparison Project Phase 3 (PMIP3) indicate an enhancement of the Choco jet intensity during the Little Ice Age (Tapias and Arias 2017). Hence, future changes in atmospheric and oceanic temperatures linked with global warming may modify the intensity of the Choco jet, bringing considerable consequences for the region's ecosystems and populations.

Taking into account the long-term variability of the Choco jet suggested by proxies and paleoclimate simulations, this chapter explores the possible future changes in the jet under a global warming scenario, using 32 GCMs part of the CMIP5 project. We use the historical run and the Representative Concentration Pathway 8.5 (RCP85) for the future projections. The former involves both natural and anthropogenic influences from 1850-2005. On the other hand, the RCP85 run assumes a radiative forcing that stabilizes with an increasing of about 8.5 Wm^{-2} after 2100 and corresponds to the strongest global warming and worst-case scenario (Taylor et al. 2012). Detailed description of data and method used is given in section 3.2. Section 3.3 describes the projected changes of the Choco jet to the end of the 21st century; and section 3.4 summarizes the results.

3.2 Data and Methodology

In order to assess the future changes in the Choco jet, we use monthly mean values from 32 coupled ocean-atmosphere GCMs, part of the CMIP5 project (Table 3.1). Only one ensemble (r1i1p1) is used for each model. Historical and RCP85 experiments are analyzed to identify changes in some of the basic features of the Choco jet (spatial distribution and annual cycle, as described in section 2.3.1). In this sense, we compare the end of the 21st century climatology (2070-2100) with present conditions (1979-2005). Therefore, zonal and meridional wind fields are used in the analysis.

Since the Choco jet is partially explained by temperature and SLP gradients between explicative regions (Ecuador-Peru cold tongue and western Colombian coast, see section 2.1), future changes in these gradients are explored. We pay special attention to the projected changes in GCMs part of the Best group (models highlighted for their more realistic representation of the basic features of the jet, see section 2.3.2), since a better representation of the present climate could be linked with a more realistic representation of future projections (Maloney et al. 2014, Knutti 2010). However, as every climate model provides alternative representations of the Earth system's response to external warming forcing (Collins et al. 2013), we use several models in order to map out the range of "possible futures" and to get an idea of the uncertainty in the climate projections. Furthermore, our results indicate that models with a better simulation of the basic features of the jet do not present a better representation of the interannual variability. Therefore, it is useful to analyze all GCMs projections, and not only the models included in the Best group, for exploring the future of the Choco jet.

Following previous studies, we use Wilcoxon-Mann-Whitney test for assessing the statistical significance of the projected changes, and Mann-Kendall test for assessing the existence of trends in the time series (Palomino et al. 2015, von Storch and Zwiers 2013).

Table 3.1 General description of the CMIP5 models used in this study. All models have available historical and RCP85 simulations during the periods 1850-2005 and 2006-2100, respectively

Model	Institute	Lat x Lon resolution	Reference
ACCESS1-0/3	Commonwealth Scientific and Industrial Research Organisation and Bureau of Meteorology Australia	1.875 x 1.25	Bi et al. 2013
CCSM4	National Center for Atmospheric Research	1.25 x 0.94	Gent et al. 2011
CESM1-BGC	NSF-DOE-NCAR	1.2 x 0.9	Hurrell et al. 2013
CMCC-CMS	Centro Euro Mediterne per I Cambiamenti Climatici	1.9 x 1.9	Scoccimarro et al. 2011
CMCC-CM	Centro Euro Mediterne per I Cambiamenti Climatici	0.75 x 0.75	Scoccimarro et al. 2011
CMCC-CESM	Centro Euro Mediterne per I Cambiamenti Climatici	2.0 x 1.9	Scoccimarro et al. 2011
CNRM-CM5	Centre National de Recherches Meteorologiques–Centre Europeen de Recherche et Formation Avancees en Calcul Scientifique	1.4 x 1.4	Voldoire et al. 2013
CSIRO-Mk3-6-0	Commonwealth Scientific and Industrial Research Organisation and Queensland Climate Change Centre of Excellence	1.87 x 1.87	Rotstayn et al. 2010
FGOALS-g2	Institute of Atmospheric Physics, Chinese Academy of Sciences	2.8 x 2.8	Li et al. 2013
GFDL-ESM2G/M/CM3	NOAA/Geophysical Fluid Dynamics Laboratory	2.5 x 2.0	Donner et al. 2011
GISS-E2-/H/H-CC/R/E-CC	National Aeronautics and Space Administration (NASA) Goddard Institute for Space Studies	2.5 x 2.0	Kim et al. 2012
HADGEM2-AO	National Institute of Meteorological Research/ Korea Meteorological Administration	1.8 x 1.25	Collins et al. 2011

HADGEM2- /CC/ES	Met Office Hadley Centre	1.8 x 1.25	Jones et al. 2011
INM-CM4.0	Institute for Numerical Mathematics	2 x 1.5	Volodin et al. 2010
IPSL-CM5B- LR/ IPSL- CM5A-LR	Institut Pierre Simon Laplace	3.75 x 1.9 2.5 x 1.26	Dufresne et al. 2013
MIROC5	Atmosphere and Ocean Research Institute (The University of Tokyo), National Institute for Environmental Studies, and Japan Agency for Marine-Earth Science and Technology.	1.4 x 1.4	Watanabe et al. 2010
MIROC-ESM/ -CHEM	Atmosphere and Ocean Research Institute (The University of Tokyo), National Institute for Environmental Studies, and Japan Agency for Marine-Earth Science and Technology.	2.8 x 2.8	Watanabe et al. 2010
MPI-ESM- LR/MR	Max Planck Institute for Meteorology	1.87 x 1.87	Zanchettin et al. 2012
MRI-CGCM3	Meteorological Research Institute	1.1 x 1.1	Yukimoto et al. 2012
NorESM1-M	Norwegian Climate Center	2.5 x 1.9	Zhang et al. 2012
NorESM1-ME	Norwegian Climate Center	2.5 x 1.9	Tjiputra et al., 2013

3.3 Results

3.3.1 Future changes in the basic features of the Choco jet

Changes in the annual cycle and spatial distribution of the Choco jet are assessed in this section. Based on similar studies on different low-level jets, we define the annual variability of the jet's core velocities as the annual cycle, and the latitude-longitude location of the core as the spatial distribution (Jiang et al. 2007, Sheffield et al. 2013). The Choco low-level jet is a westerly surface circulation, thus we use zonal winds at 925hPa to

represent its annual cycle, and horizontal winds at the same level pressure for the spatial distribution. Differences between future (2070-2100) and present (1979-2005) climatologies of these basic features are analyzed for the 32 GCMs, with an assessment of the inter-model agreement in projected changes and a special focus in the projected conditions by Best models.

3.3.1.1 Annual cycle

Fig. 3.1 shows the differences between future and present climatological annual cycle of the Choco jet. There are two non-contradictory future conditions that are dominant in GCM's projections. Almost half of the models (12) simulate a weakening of the Choco jet between June-November located north of the equator. In particular, Best models (HadGEM, MPI and CNRM) exhibit an agreement in this type of projected changes in the annual cycle. On the other hand, other twelve models suggest a strengthening of the jet to the south of the equator during June-September (Fig. 3.1). Specifically, GCMs with a weaker Choco jet to the north of the equator present a slight strengthening of the jet to the south of the equator (MPI-ESM-LR/MR, HadGEM2-AO/ES/CC, ACCESS1-0/3 and CMCC-CESM/CM). Conversely, NorESM1-M/ME models project an increase in the intensity of the Choco jet during the whole year over both north and south equatorial regions. However, it is important to remark that these models are part of the Worst group in simulating the basic features of the jet (section 2.3.2). Some models (CMCC-CMS, IPSL-CM5B-LR, MIROC5 and MRI-CGCM3) present no important changes through the year. Regardless whether there is a strengthening or weakening of the projected intensity of the jet, changes in the annual cycle tend to occur in the second part of the year, between May-November in most of the models.

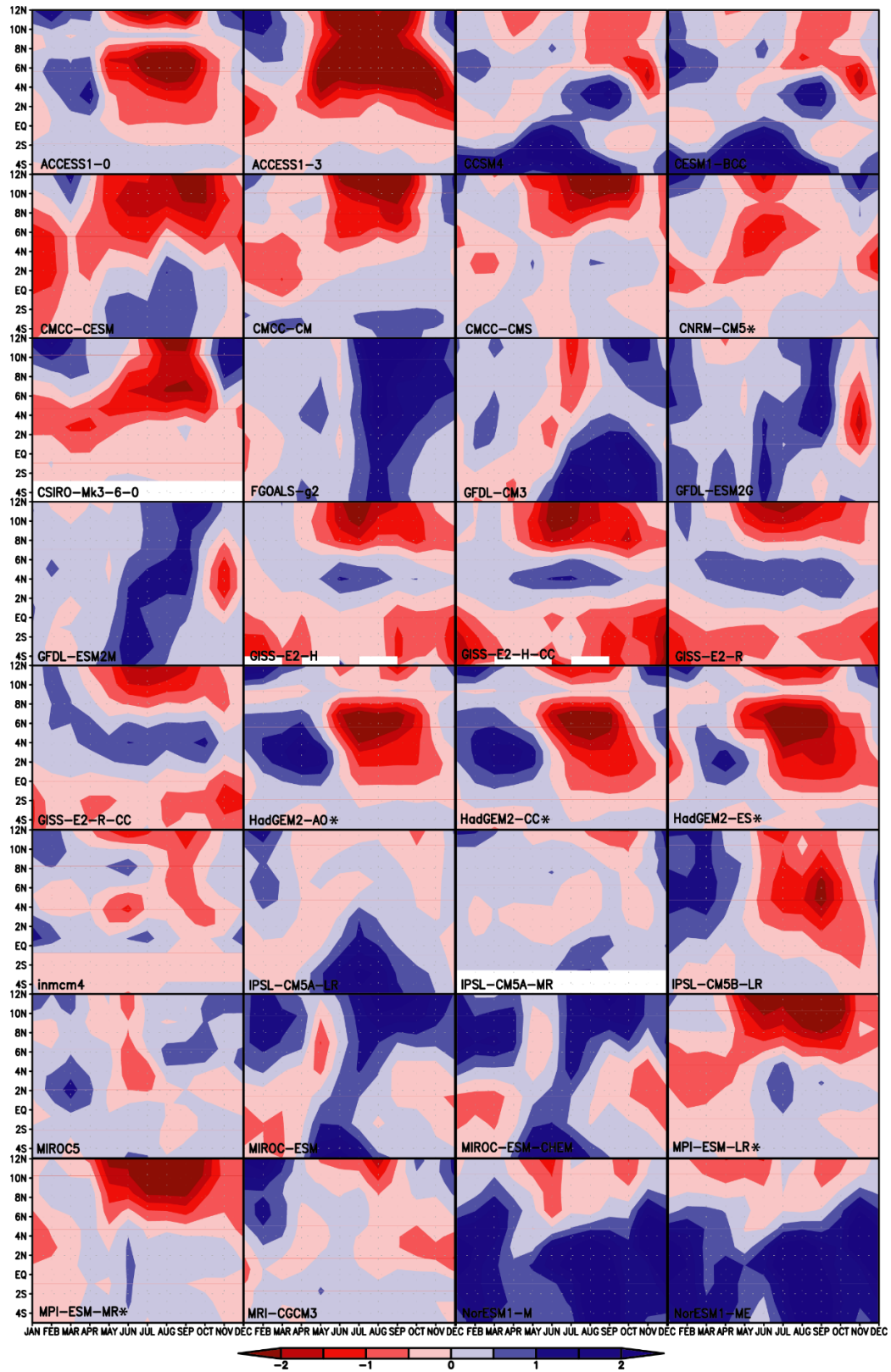


Fig. 3.1 Annual cycle differences between future (2070-2100) and present (1979-2005) zonal wind at 925hPa and 80°W. The asterisks indicate the Best models. Data in $m s^{-1}$

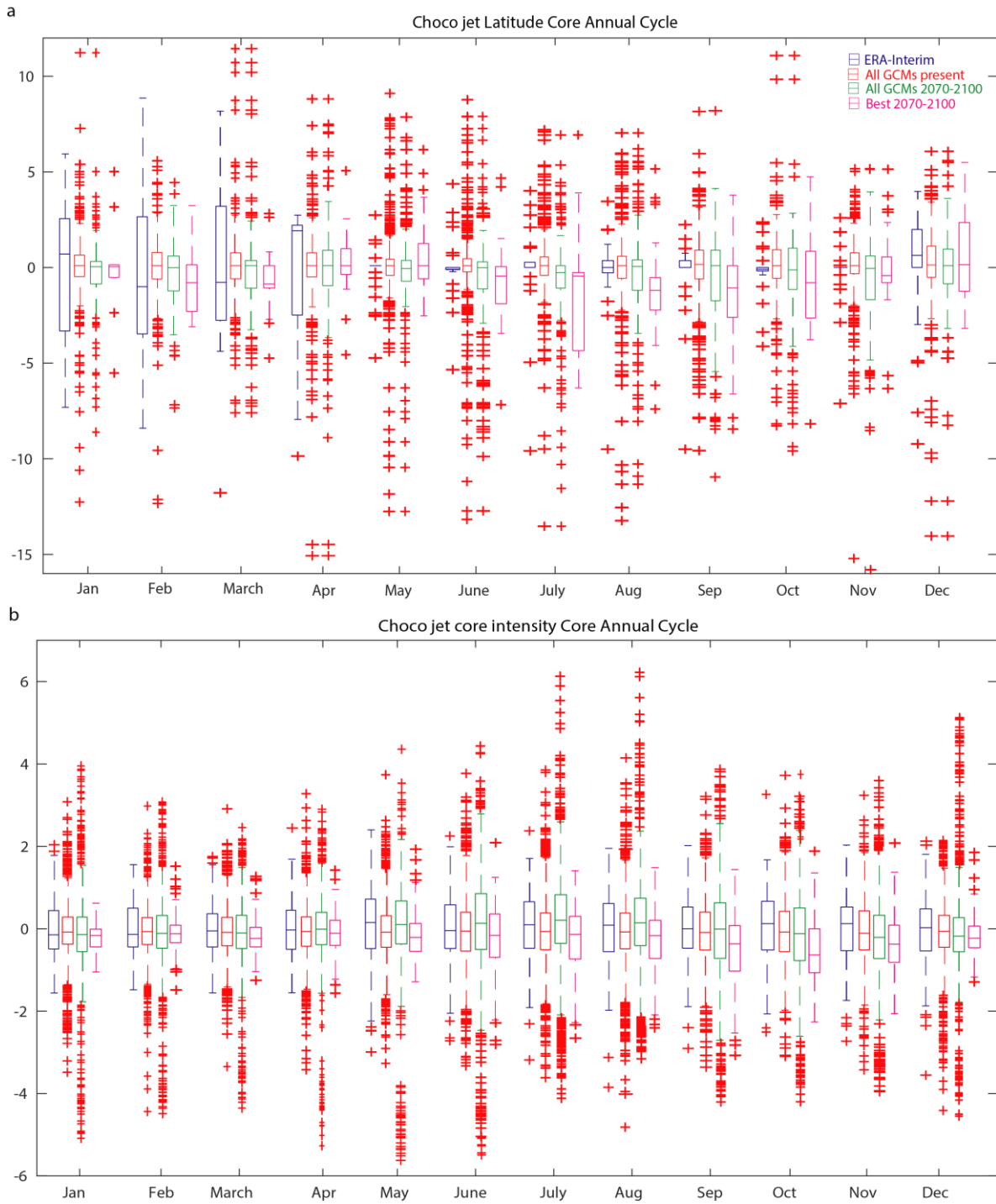


Fig. 3.2 Boxplots of **a** Choco jet latitudinal anomalies ($^{\circ}$), **b** Choco jet core intensity (m s^{-1}) for present and future conditions

In order to confirm the results discussed above, we analyze the Choco jet latitudinal anomalies time series (latitude location of the jet). The tracking of the Choco jet is

performed by locating the core of the jet (maximum zonal wind at 925hPa, at 80°W and between 15°S-15°N). We also analyze the jet's core time series looking for identifying the future changes in the Choco jet intensity. We do not use the Choco jet index because it involves a latitudinal average that can lead to misleading conclusions. Fig 3.2 a shows a southern location of the Choco jet by the end of the century in all GCMs and Best models during June-November in accordance with Fig 3.1. On the other hand, Fig 3.2 b presents a strengthened Choco jet in all GCMs set and a weakened jet in Best models projections. These changes also occurs during the second half of the year.

3.3.1.2 Spatial distribution

Although in the annual mean, the tropical Pacific is not one of the main moisture sources to northern South America, it becomes important during the boreal fall (Arias et al. 2015, Agudelo et al. 2017). Particularly, for western Colombia, the south tropical Pacific Ocean plays an important role for the genesis of MCSs during June-November (Sakamoto et al. 2011), when the Choco low-level jet is more active (Poveda and Mesa 2000). Accordingly, we focus our analysis in the boreal summer and fall seasons. In addition, the future changes in the annual cycle of the jet obtained in this study appear to be significant for these particular seasons. Figure 3.3 shows the differences between future and present climatological horizontal winds over northern South America at 925hPa (spatial distribution of the Choco jet) during boreal summer. Most of the models present an intensification of the Caribbean low-level jet by the end of the 21st century under a global warming scenario that is consistent with previous studies (Taylor et al. 2013, Cook et al. 2008). Over the Pacific Ocean, the GCM's projected changes are in less agreement. However, some models (including Best models) present a decreasing in the Choco jet wind

velocities that occurs between 3°N-9°N (ACCESS1-0, ACCESS-3, CMCC-CM, CSIRO, HadGEM2-AO, HadGEM2-ES, HadGEM2-CC, MPI-ESM-LR, MPI-ESM-MR). Conversely, models with a stronger Choco jet present an enhanced jet located south of 3°N (CCSM4, CESM1-BGC, FGOALS-g2, IPSL-CM5A-LR, IPSL-CM5A-MR, MIROC-ESM, MIROC-ESM-CHEM, NorESM1-ME, NorESM1-M). Similar changes are observed during SON, but more GCMs (13) simulate a weakening of the Choco jet in this season (Fig. S3-1). Lee and Wang (2014) find similar changes in horizontal winds at 850hPa using RCP4.5 scenario for the end of the 21st century.

3.3.2 Future changes in the mechanisms involved in the dynamics of the Choco jet

The existence of the Choco jet is the result of, among others factors, SST and SLP differences between three particular regions: western Colombia (Colom; 75°W-77.5°W, 2°N-8°N), Colombian Pacific coast (ColPac; 77.5°W-82°W, 2°N-8°N), and Niño 1-2 region (10°S-0°, 90°W-80°W) (Fig. 2.4a) (Poveda and Mesa 2000, Poveda et al. 2014). Figure 3.4 presents the seasonal anomalies for temperature and SLP differences among these regions, as well as the precipitation area average over western Colombia (75°W-77.5°W, 2°N-8°N) and the Choco jet index during boreal summer. We also assess the changes in probability density function (PDF) for the seasonal anomalies of these time series. Significant changes in the future PDFs are identified using Wilcoxon-Mann-Whitney test by comparing present (1979-2005) and future (2073-2100) conditions. Fig. 3.5 shows the distributions for all models ensemble.

There is a strong agreement (20 out of 32 models) in a positive significant temperature gradient trend between Colom-ColPac regions during the whole year caused by a stronger warming over the continent (Figs. 3.4a and 3.5a). However, the SLP gradient between the same regions also exhibits a positive significant trend in most of the models (19 out of 32 models), which implies a weakening of the surface pressure gradient (Figs. 3.4d and 3.5d). Best models are in agreement in these projected changes. A significant trend of weakening for temperature and SLP differences between ColPac-Niño regions are observed through the year (Figs. 3.4b, 3.5b, 3.4e and 3.5e), with higher agreement during JJA and SON (22 out of 32 models for SLP gradients, and 14 out of 32 models for SST differences, respectively). Because these temperature and SLP gradients are involved in the movement of air masses from the southern tropical Pacific to the Colombian coasts, their weakening could be related with a weakening of the Choco jet activity north of the equator and a strengthening over the southern part, i.e., a southward migration of the Choco jet as the previous section suggests. In fact, in Chapter 2 we find that Worst models exhibit a further south Choco jet and weaker SST and SLP gradients between ColPac-Niño regions. On the other hand, although the SLP gradient between Colom-Niño presents a positive significant trend for most of the models during all the seasons (weakening trend) (Figs. 3.4f and 3.5f), Best models only agree in the nature of the change during the second part of the year. Conversely, there is a low agreement in the projected changes of the temperature differences between the same regions. Therefore, we find favorable future conditions for an enhancement of the Choco jet activity north of the equator driven by Colom-ColPac temperature differences during the entire year, but unfavorable conditions related with a weakening of temperature differences between ColPac-Niño regions, as well as a decreasing of the SLP differences among all regions. However, the weakening of the SST

gradient between ColPac-Niño regions, as well as a more marked landmass-ocean temperature gradient, strengthen the Choco jet in front of the Ecuador coast (see supplementary material).

Precipitation over western Colombia is related with the activity of the Choco jet (Poveda and Mesa 2000, Poveda et al. 2006) (see section 2.3.6). Over this region, the area averaged rainfall anomalies exhibit a positive trend in most of the models during boreal summer and fall (Figs. 3.3g and 3.4g, S3-2g S3-3g, S3-2f and S3-3f). However, there exist an agreement in the future rainfall changes among Best models only in JJA. Palomino-Lemus et al. (2015) find an increase in future precipitation over western Colombia using a downscaling technique for five CMIP5 GCMs.

Because the Choco jet index is defined as the mean of zonal winds between the latitudinal range 5°S-7°N, and taking into account that the jet exhibits different future changes over the northern and southern equatorial region, most of the models present opposite anomalies that are averaged when computing the jet index, generating no apparent significant changes in the jet index. In spite of this, almost half of the models and the multi-model mean present a significant positive trend in the Choco jet intensity during JJA (Figs. 3.4h and 3.5h), which is consistent with the agreement in the increasing rainfall anomalies over the Pacific Colombian region observed in the western Colombia precipitation time series.

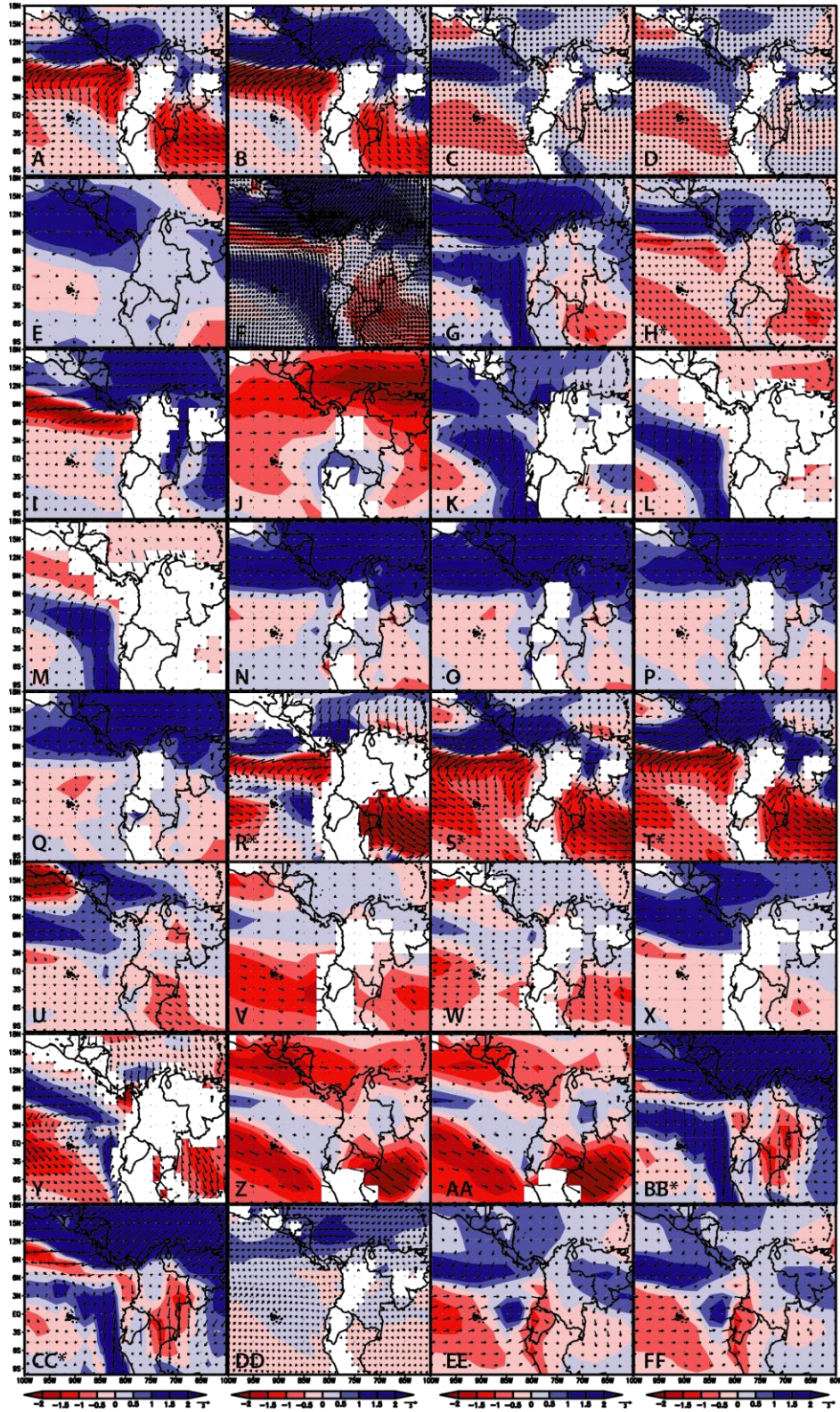


Fig. 3.3 Climatology differences between future (2070-2100) and present (1979-2005) horizontal winds (vectors) and wind difference magnitude (shading) at 925hPa for JJA. Asterisks indicate the Best models ((A) ACCESS1-3, (B) ACCESS1-0, (C) CCSM4, (D) CESM1-BGC, (E) CMCC-CESM, (F) CMCC-CM, (G) CMCC-CMS, (H*) CNRM-CM5, (I) CSIRO-Mk3-1-0, (J) FGOALS-g2, (K) GFDL-CM3, (L) GFDLES-

2G, (M) GFDLESM-2M, (N) GISS-E2-H-CC, (O) GISS-E2-H, (P) GISS-E2-R-CC, (Q) GISS-E2-R, (R*) HadGEM2-AO, (S*) HadGEM2-CC, (T*) HadGEM2-ES, (U) INMCM4, (V) IPSL-CM5A-LR, (W) IPSL-CM5A-MR, (X) IPSL-CM5B-LR, (Y) MIROC5, (Z) MIROC-ESM, (AA) MIROC-ESM-CHEM, (BB*) MPI-ESM-LR, (CC*) MPI-ESM-MR, (DD) MRI-CGCM3, (EE) NorESM1-M, (FF) NorESM1-ME. Data in m s^{-1}

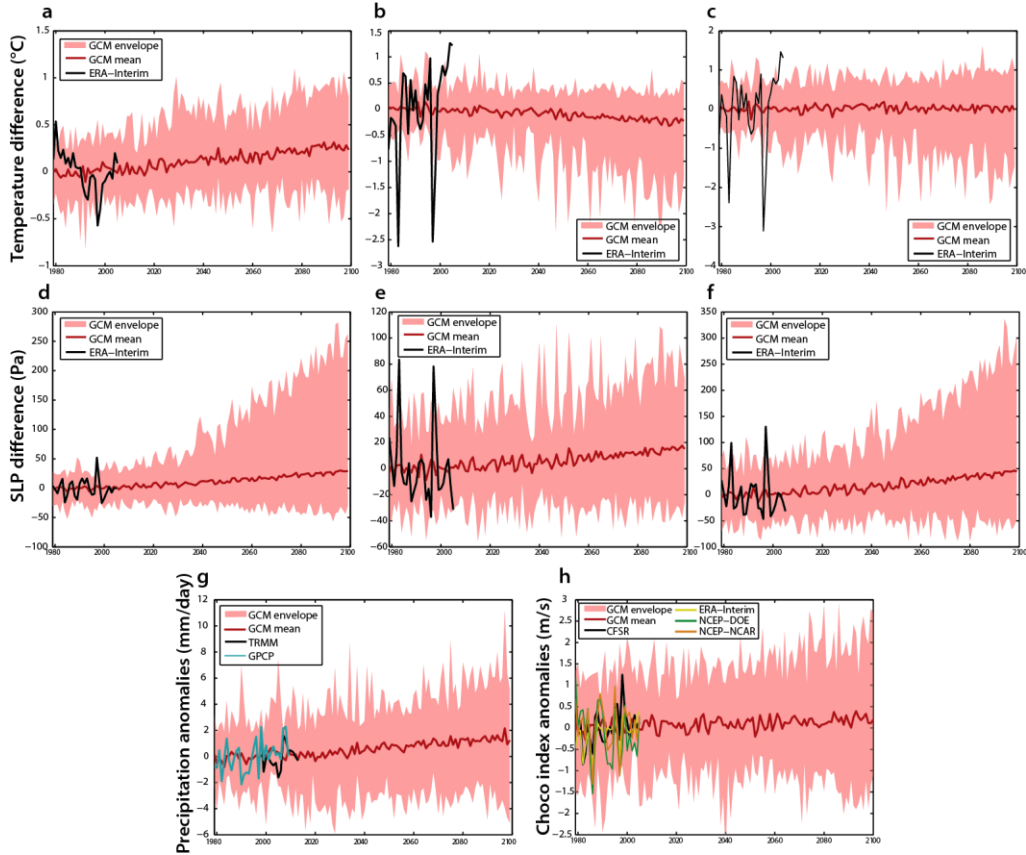


Fig. 3.4 Seasonal JJA anomalies of the temperature differences at 1000hPa ($^{\circ}\text{C}$) between: **a** Colom-ColPac, **b** ColPac-Niño, and **c** Colom-Niño. Seasonal anomalies of the SLP differences (Pa) between: **d** Colom-ColPac, **e** ColPac-Niño, and **f** Colom-Niño. **g** Area average precipitation anomalies (mm day^{-1}) over western Colombia (75°W - 77.5°W , 2°N - 8°N). **h** Choco jet index anomalies (m s^{-1}). Time series for the period 1979-2100

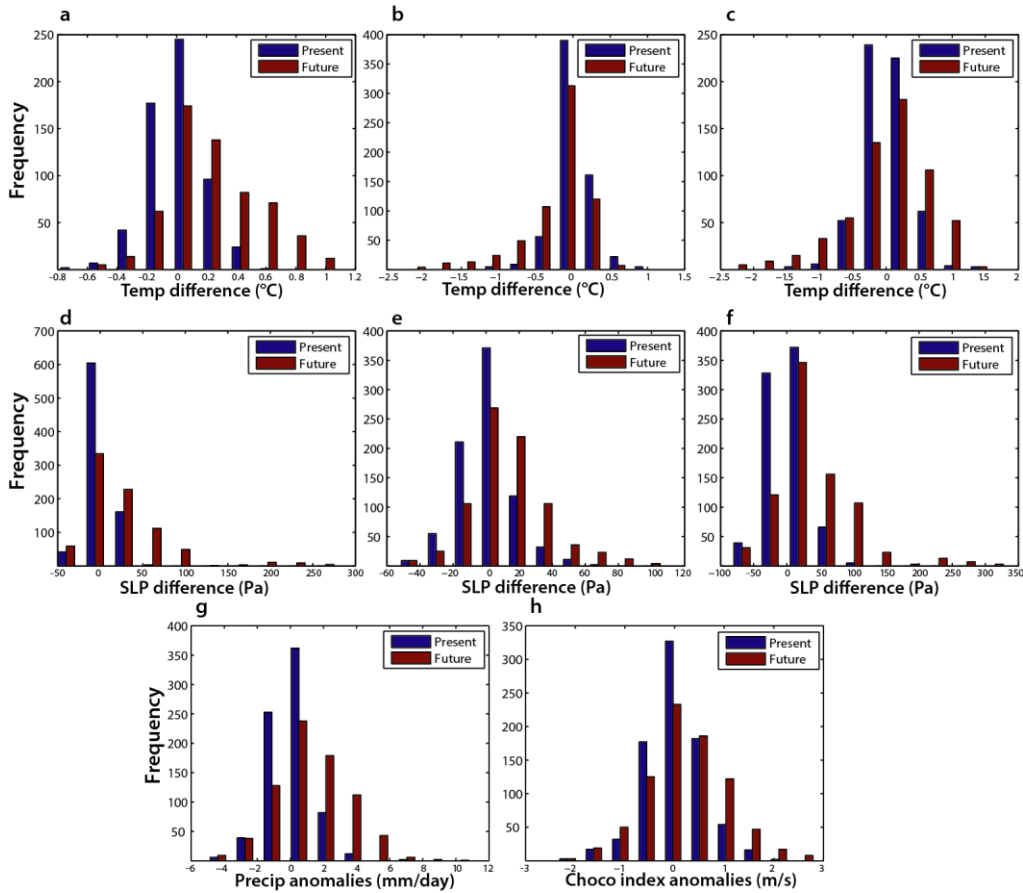


Fig. 3.5 Probability density functions for seasonal JJA anomalies of: temperature differences at 1000hPa ($^{\circ}\text{C}$) between **a** Colom-ColPac, **b** ColPac-Niño, and **c** Colom-Niño. SLP differences (Pa) between **d** Colom-ColPac, **e** ColPac-Niño, and **f** Colom-Niño. **g** Area average precipitation anomalies (mm day^{-1}) over western Colombia ($75^{\circ}\text{W}-77.5^{\circ}\text{W}$, $2^{\circ}\text{N}-8^{\circ}\text{N}$). **h** Choco jet index anomalies (m s^{-1}). Data from the multi-model ensemble. All PDFs exhibit changes with a 95% confidence level

3.4 Discussion and Conclusions

The Choco low-level jet is an important atmospheric feature for northern South America hydro-climatology. At interannual scales, variations in the intensity of this jet are related with rainfall anomalies over central and western Colombia (Arias et al. 2015, Martínez et al. 2003, Mapes et al. 2003, Zuluaga and Poveda 2004). Therefore, future changes in the Choco low-level jet caused by global warming could generate important impacts on populations and ecosystems over the region. Therefore, in this chapter we explore the

possible future changes of this surface circulation under the RCP85 global warming scenario.

Because one of the common methods to explore future projections is to select models with better simulation of the particular phenomenon in the present-day climate (Maloney et al. 2014, Cook and Vizi 2008), we pay particular attention to future conditions in GCMs that present a more realistic simulation of the basic features of the Choco jet (models part of the Best group, section 2.3.2). However, in order to map out the range of “possible futures” and to get an idea of the uncertainty in the climate projections, we also use 32 different GCMs (Collins et al. 2013).

Our results suggest that there are two different future changes in the Choco jet. The first scenario consists of a weakening of the jet, which is observed in half of the models during JJA and SON in the northern part of the tropical Pacific Ocean (between 3°N-9°N). Best models agree in these future conditions. A second scenario is depicted by 12 of the GCMs and exhibits a strengthening of the Choco jet below 3°N during the same seasons (Figs. 3.1 and 3.3). In addition, the future southward migration of the Choco jet projected by CMIP5 models during JJA and SON seems to be caused by a weakening of the temperature and SLP gradients between Colom-Niño region (Figs. 3.4 and 3.5), which generates a pressure gradient force that is north-south oriented (see supplementary material). Conversely, an increasing of the surface temperature contrast between continental and oceanic regions tends to strengthen the Choco jet velocity (see supplementary material). As a consequence of the combination of these factors, we find a stronger and further south Choco jet by the end of the 21st century. Figure 3.6 shows a schematic diagram that summarizes the future

changes on this low-level jet. Changes in this surface circulation could imply regional future changes in precipitation that need to be addressed in further studies.

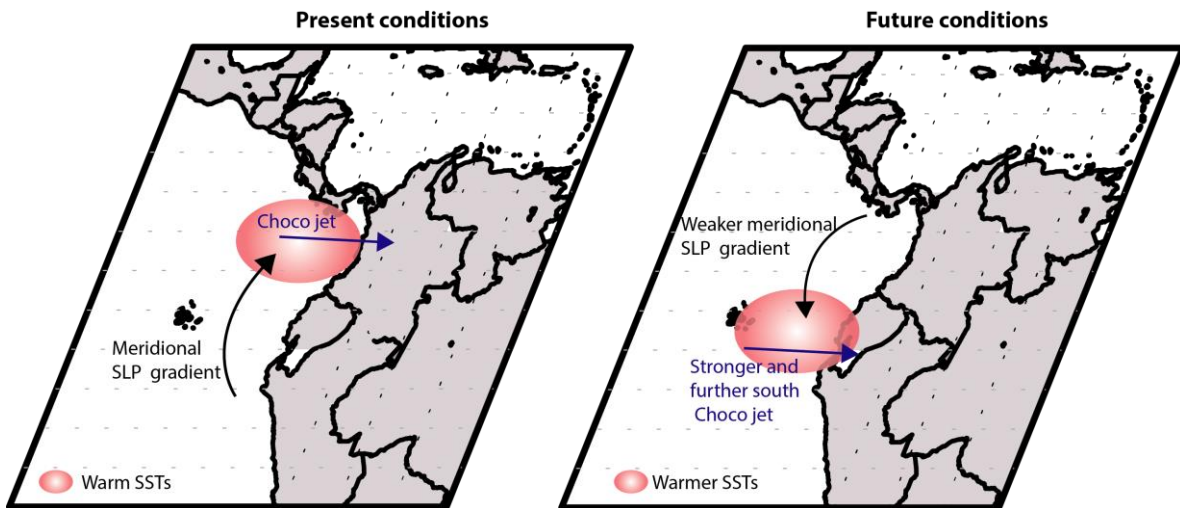


Fig. 3.6 Schematic diagram of the present conditions that partially explain the existence of the Choco jet (left) and the future projected changes in these conditions according to CMIP5 GCMs (right). Future warmer SSTs offshore of the Ecuador-Peru coast weaken the north-south oceanic SLP gradient, pushing the Choco jet further south of its current position

3.5 Supplementary material

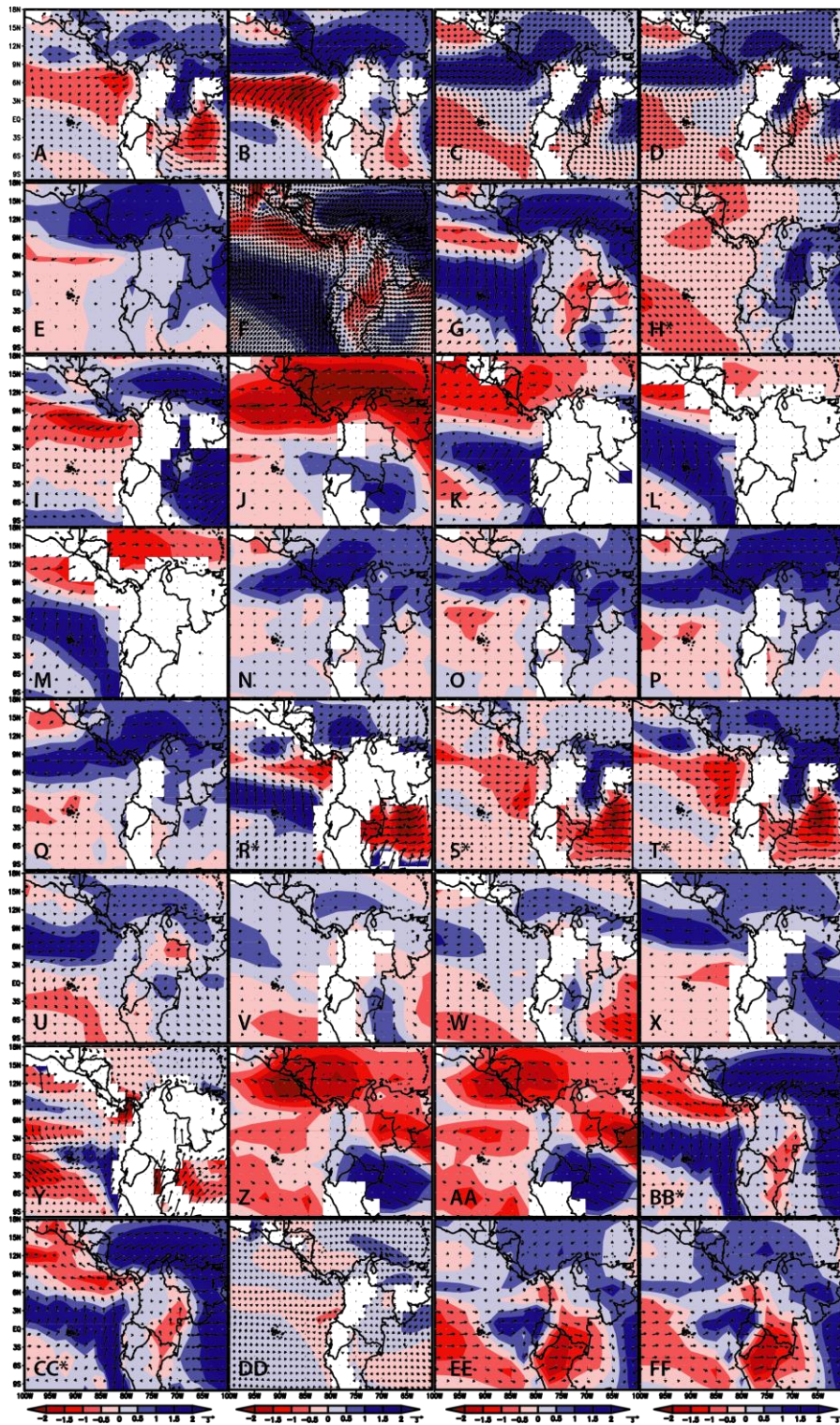


Fig. S3-1 Climatology differences between future (2070-2100) and present (1979-2005) horizontal winds (vectors) and wind difference magnitude (shading) at 925hPa for SON. Asterisks indicate the Best models

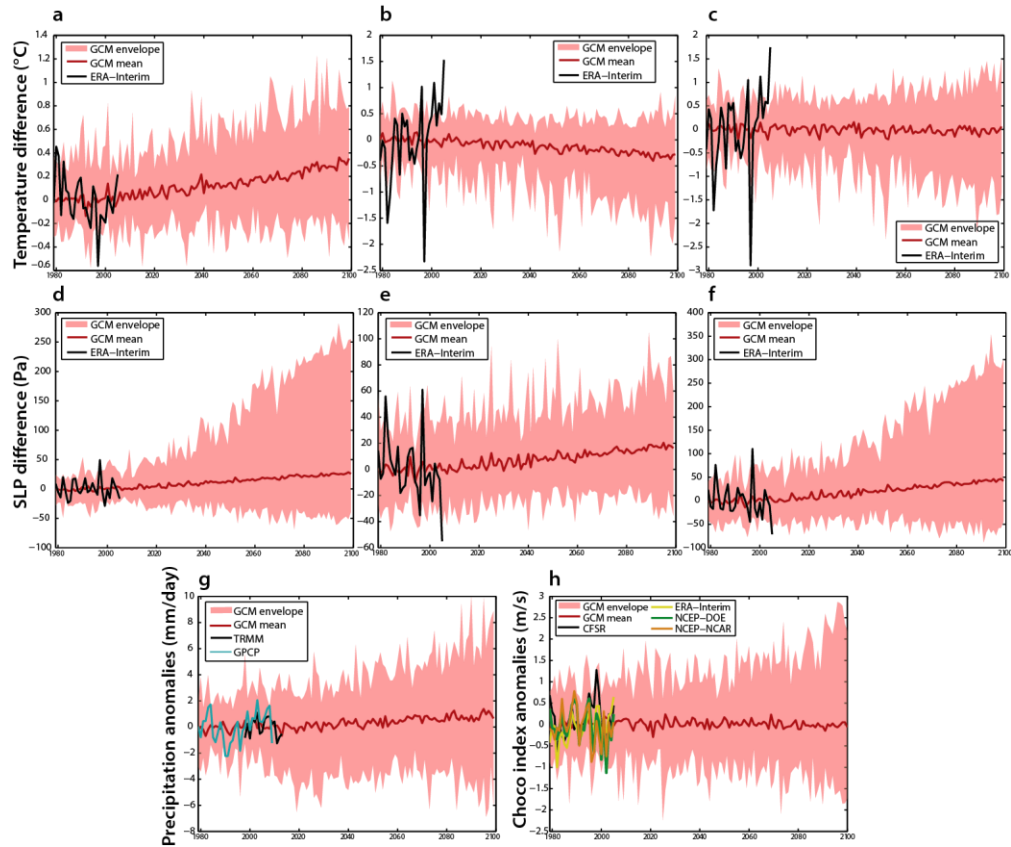


Fig. S3-2 Seasonal SON anomalies of the temperature differences ($^{\circ}\text{C}$) between: **a** Colom-ColPac, **b** ColPac-Niño, **c** Colom-Niño. Seasonal anomalies of the sea level pressure differences (Pa) between: **d** Colom-ColPac, **e** ColPac-Niño, **f** Colom-Niño. **g** Area average precipitation anomalies (mm day^{-1}) over western Colombia ($75^{\circ}\text{W}-77.5^{\circ}\text{W}$, $2^{\circ}\text{N}-8^{\circ}\text{N}$). **h** Choco jet index anomalies (m s^{-1}). Time series for the period 1979-2100

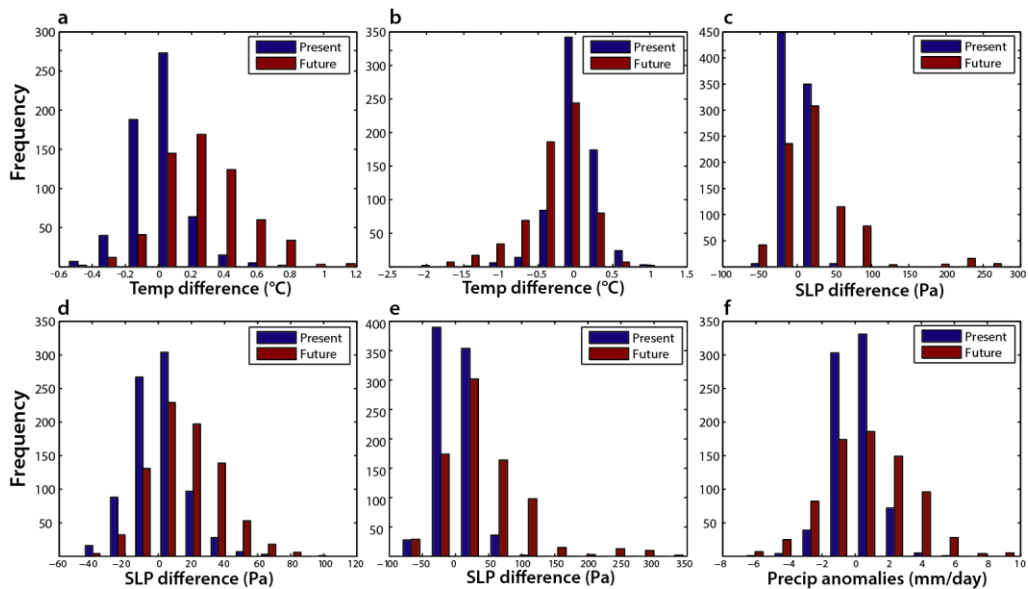


Fig. S3-3 Probability density functions for seasonal SON anomalies of: temperature differences at 1000hPa ($^{\circ}\text{C}$) between **a** Colom-ColPac, and **b** ColPac-Niño. SLP differences (Pa) between **c** Colom-ColPac, **d** ColPac-Niño, and **e** Colom-Niño. **f** Area average precipitation anomalies (mm day^{-1}) over western Colombia

(75°W-77.5°W, 2°N-8°N). Data from the multi-model ensemble. All PDFs exhibit changes with a 95% confidence level

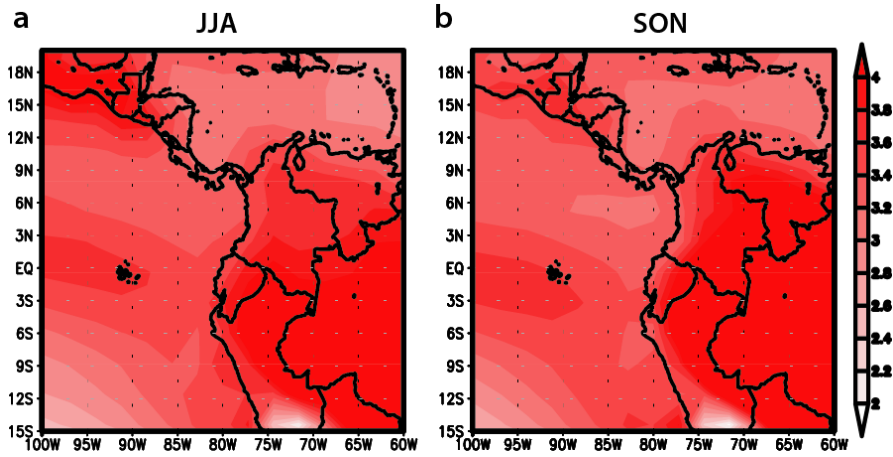


Fig. S3-4 Ensemble mean of temperature difference between future (2070-2100) and present (1979-2005) climatology at 1000hPa for: **a** boreal summer, and **b** boreal fall. Data in °C

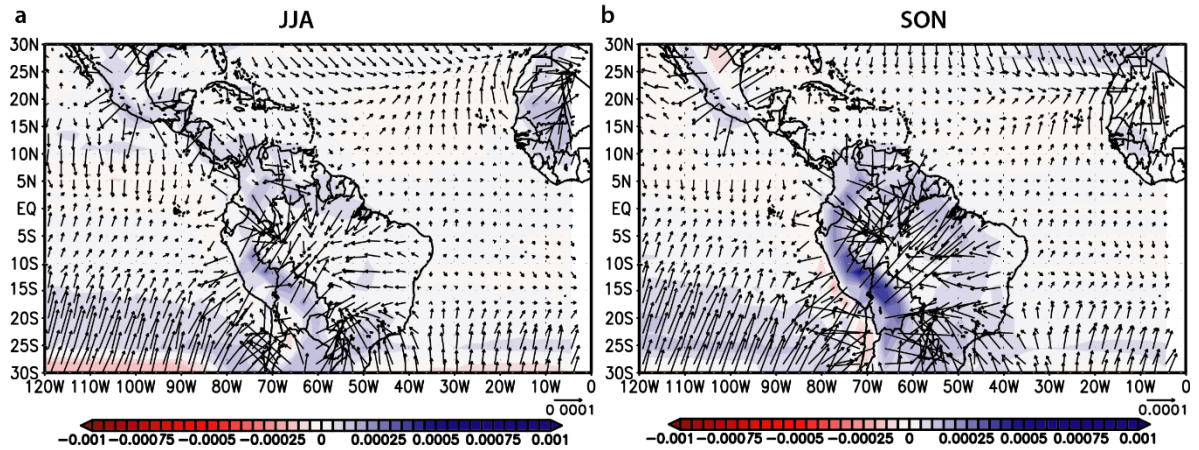


Fig. S3-5 Ensemble mean of SLP gradient differences (vectors) and SLP gradient difference magnitude (shading) between future (2070-2100) and present (1979-2005) climatology for: **a** boreal summer, and **b** boreal fall. Data in Pa m⁻¹

General Conclusions

Chapter 1 assess the ability of 32 GCMs part of the CMIP5 project to simulate the precipitation climatology over northern South America for the period 1979-2005, in order to identify models that exhibit the best representations over the region and to analyze the possible causes of biases of rainfall simulations. Our results suggest that, due to an anomalous warming over the southern part of the eastern tropical Pacific during DJF and MAM, models are unable to properly simulate precipitation over the region, locating the oceanic ITCZ further south. This error is linked to dry biases in precipitation annual cycle over several continental regions (Andean, Pacific, and Caribbean regions). Therefore, in a general sense, a good representation of the surface temperature over the eastern tropical Pacific is related with a satisfactory simulation of rainfall over the same region. However, we find that during MAM and SON, small improvements in the simulation of temperature spatial distribution over the eastern tropical Pacific can lead to significant improvements in precipitation spatial pattern over the same region. Finally, by using Taylor diagrams, annual cycles in continental regions, and the inter-hemispheric temperature gradients over the Pacific Ocean, we identify models with a better simulation of rainfall over northern South America (ACCESS1-0, ACCESS1-3, HadGEM2-CC, and HadGEM2-ES).

Since precipitation is the result of several complex processes, many of them not solved by GCMs, Chapter 2 explores the skill of GCMs to reproduce the existence of the Choco low-level jet. This jet is involved in the genesis of Mesoscale Convective Systems in the region, and therefore, is linked to precipitation over central and western Colombia. We use 26 CMIP and 11 AMIP models included in the CMIP5 archive, and we focus on the

simulation of the climatological basic features (annual cycle, spatial distribution and vertical structure) of the jet. Using factor and cluster analysis, we objectively classify models in Best, Worst, and Intermediate groups. Despite the coarse horizontal resolution of GCMs, this study demonstrates that nearly all models can represent the existence of the Choco low-level jet. AMIP and Best models present a more realistic simulation of the jet. Worst models exhibit biases such as an anomalous southward location of the Choco jet during the whole year and a shallower jet. The model skill to represent this local jet comes from their ability to reproduce some of its main origin processes, such as the temperature and pressure differences between particular regions in the eastern Pacific and western Colombian lands, which are non- local features. Conversely, Worst models considerably underestimate temperature and pressure differences between these key regions. We identify a close relationship between the location of the Choco jet and the Inter-tropical Convergence Zone (ITCZ), and CMIP5 models are able to represent such relationship. In this sense, errors in Worst models are related with bias in the location of the ITCZ over the eastern tropical Pacific Ocean, as well as the representation of the topography and the horizontal grid size. However, we also explore GCMs skill to represent the interannual variability dominant modes of the Choco jet, as well as the interannual relationship with the precipitation over the region. We find that the interannual variability of this jet seems mainly controlled by low frequency phenomena such as the PDO and AMO in all reanalysis. Although, due to the limited length of the time series of the Choco jet, our results present serious limitations. The ENSO signal also plays an important role in controlling the interannual variability of the Choco jet, with important contributions during strong El Niño years. ENSO and PDO are negatively related to the activity of the Choco jet, due to the similar SLP and SST anomalies pattern over the Pacific Ocean between these

large scale phenomena. Conversely, the Choco jet seems to be directly correlated with the AMO phase because of the nature of its SST anomalies over the south tropical eastern Pacific. AMIP and CMIP models are able to represent the signal of these atmospheric-oceanic phenomena in the Choco jet time series. In the same way, GCMs are able to properly represent the direct relationship observed between the Choco jet activity and the precipitation over the western part of Colombia. However, only some models (CCSM4, CESM1-FASTCHEM, CESM1-WACCM, MPI-ESM-LR, MPI-ESM-MR, MPI-ESM-P, MIROC5) are able to realistically simulate the spatial pattern of the relationship between the Choco jet index anomalies and the precipitation anomalies over the region. AMIP models present a better simulation of this pattern. It is important to remark that Best and Worst models do not exhibit significant differences in their representations of the interannual variability of the Choco jet, probably because this classification is only based on the representation of the climatological features of the jet. Therefore, to explore the future projections of the Choco jet in Chapter 3, we use all available GCMs and not only the models classified as Best.

Future changes of the Choco low-level jet are examined in Chapter 3. In order to map out the range of “possible futures” and to get an idea of the uncertainty in the climate projections, we use 32 different GCMs, but we pay particular attention to future conditions in GCMs that present a more realistic simulation of the basic features of the Choco jet (models part of the Best group). Models tend to agree on two different future conditions of the jet: i) a weakening of the jet in half of the models during JJA and SON in the northern part of the tropical Pacific Ocean (between 3°N-9°N). Best models agree in these future conditions; ii) 12 of the GCMs exhibit a strengthening of the Choco jet below 3°N during

the same seasons. These changes in the Choco jet are driven by a weakening of the temperature and SLP gradients between Colom-Niño region, which generates a north-south oriented pressure gradient force, and an increase of the surface temperature contrast between continental and oceanic regions. Therefore, the Choco jet seems to present a southward migration by the end of the 21st century, which could imply regional future changes in precipitation that need to be addressed in further studies.

References

Adam O, Bischoff T, Schneider T (2015) Seasonal and interannual variations of the energy flux equator and ITCZ. Part I: Zonally averaged ITCZ position. *Journal of Climate* 29(9): 3219-3230

Adler RF, Huffman GJ, Chang A et al. (2003) The version-2 global precipitation climatology project (GPCP) monthly precipitation analysis (1979-present). *Journal of hydrometeorology* 4(6): 1147-1167

Agudelo J, Arias PA, Vieira SC, Martínez JA (2017) The lengthening of the Amazon dry season: influence on water vapor transport toward the Intra-American region. *Climate Dynamics*, submitted

Amador JA (1998) A climatic feature of the tropical Americas: The trade wind easterly jet. *Tópicos meteorológicos y oceanográficos*, 5(2), 91-102

Amador JA (2008) The intra-Americas sea low-level jet. *Annals of the New York Academy of Sciences*, 1146(1), 153-188

Amante C, Eakins BW (2009) ETOPO1 1 Arc-Minute Global Relief Model: Procedures, Data Sources and Analysis. NOAA Technical Memorandum NESDIS NGDC-24. National Geophysical Data Center, NOAA. doi:10.7289/V5C8276M

Ambrizzi T, de Souza EB, Pulwarty RS (2004) The Hadley and Walker regional circulations and associated ENSO impacts on South American seasonal rainfall. In: Diaz J, Bradley RS (ed) *The Hadley circulation: present, past and future*, Kluwer Academic Publishers, Springer Netherlands pp 203-235

Arias PA, Martínez JA, Vieira SC (2015) Moisture sources to the 2010-2012 anomalous wet season in northern South America. *Climate Dynamics* 45(9-10): 2861-2884. doi: 10.1007/s00382-015-2511-7

Arora VK, Scinocca JF, Boer GJ et al. (2011) Carbon emission limits required to satisfy future representative concentration pathways of greenhouse gases. *Geophysical Research Letters* 38(5)

Bellenger H, Guilyardi É, Leloup J, Lengaigne M, Vialard J (2014) ENSO representation in climate models: from CMIP3 to CMIP5. *Climate Dynamics*, 42(7-8), 1999-2018

Bi D, Dix M, Marsland SJ et al. (2013) The ACCESS coupled model: description, control climate and evaluation. *Aust. Meteorol. Oceanogr. J.*63(1), 41-64

Bischoff T, Schneider T (2015) The equatorial energy balance, ITCZ position, and double ITCZ bifurcations. *Journal of Climate* 29(8): 2997-3013

Broccoli AJ, Dahl KA, Stouffer RJ (2006). Response of the ITCZ to Northern Hemisphere cooling. *Geophysical Research Letters* 33(1)

Cai W, Borlace S, Lengaigne M et al. (2014) Increasing frequency of extreme El Niño events due to greenhouse warming. *Nature Climate Change* 4(2)

Cannon AJ (2015) Selecting GCM scenarios that span the range of changes in a multimodel ensemble: application to CMIP5 climate extremes indices. *Journal of Climate*, 28(3) 1260-1267

Carmona AM, Poveda G (2014) Detection of long-term trends in monthly hydro-climatic series of Colombia through Empirical Mode Decomposition. *Climatic change* 123(2), 301-313

Colas F, McWilliams JC, Capet X, Kurian J (2012) Heat balance and eddies in the Peru-Chile current system. *Climate dynamics* 39(1-2): 509-529

Collins WJ, et al. (2011) Development and evaluation of an Earth-System model HadGEM2. *Geosci. Model Dev.* 4, 1051–1075

Collins M, Knutti R, Arblaster J, Dufresne JL, Fichefet T, Friedlingstein P, Gao X, Gutowski WJ, Johns T, Krinner G, Shongwe M, Tebaldi C, Weaver AJ, Wehner M (2013)

Long-term Climate Change: Projections, Commitments and Irreversibility. In: Climate Change 2013: The Physical Science Basis. Contribution of Working Group I to the Fifth Assessment Report of the Intergovernmental Panel on Climate Change [Stocker TF, Qin D, Plattner GK, Tignor M, Allen SK, Boschung J, Nauels A, Xia Y, Bex V and Midgley PM (eds.)]. Cambridge University Press, Cambridge, United Kingdom and New York, NY, USA

DANE (2011) Estadística DANE, Statistical database. DANE, Bogotá

Dee DP, Uppala SM, Simmons AJ et al. (2011) The ERA-Interim reanalysis: Configuration and performance of the data assimilation system. Quarterly Journal of the Royal Meteorological Society 137(656): 553-597

Donohoe A, Marshall J, Ferreira D, Mcgee D (2013) The relationship between ITCZ location and cross-equatorial atmospheric heat transport: From the seasonal cycle to the Last Glacial Maximum. Journal of Climate 26(11): 3597-3618

Donner LJ, Wyman BL, Hemler RS et al. (2011) The dynamical core, physical parameterizations, and basic simulation characteristics of the atmospheric component AM3 of the GFDL global coupled model CM3. Journal of Climate 24(13): 3484-3519

Dufresne JL, Foujols MA, Denvil S et al. (2013) Climate change projections using the IPSL-CM5 Earth System Model: from CMIP3 to CMIP5. Climate Dynamics 40(9-10): 2123-2165

Ebisuzaki W (1997) A method to estimate the statistical significance of a correlation when the data are serially correlated. Journal of Climate 10(9): 2147-2153

Enfield DB, Mestas-Nuñez AM, Trimble PJ (2001) The Atlantic multidecadal oscillation and its relation to rainfall and river flows in the continental US. Geophysical Research Letters, 28(10), 2077-2080

Flato G, Marotzke J, Abiodun B et al. (2013) Evaluation of climate models. In: Climate Change 2013 The Physical Science Basis. Contribution of Working Group I to the Fifth Assessment Report of the Intergovernmental Panel on Climate Change. Cambridge University Press, pp 741-866

Garreaud R, Vuille M, Compagnucci R, Marengo J (2009) Presentday South American climate. *Palaeogeogr Palaeoclimatol Palaeoecol* 281:180–195

Gent PR, Danabasoglu G, Donner LJ et al. (2011) The community climate system model version 4. *Journal of Climate* 24(19): 4973-4991

Gleckler PJ, Taylor KE, C Doutriaux (2008) Performance metrics for climate models. *Journal of Geophysical Research: Atmospheres* Vol. 113(D6)

Gordon CT, Rosati A, Gudgel R (2000) Tropical sensitivity of a coupled model to specified ISCCP low clouds. *Journal of Climate* 13(13): 2239-2260

Gulizia C, Camilloni I (2015) Comparative analysis of the ability of a set of CMIP3 and CMIP5 global climate models to represent precipitation in South America. *International Journal of Climatology* 35(4): 583-595

Hirota N, YN Takayabu (2013) Reproducibility of precipitation distribution over the tropical oceans in CMIP5 multi-climate models compared to CMIP3. *Climate Dynamics* 41, 11-12

Hoyos I, Dominguez F, Cañón-Barriga J et al. (2017). Moisture origin and transport processes in Colombia, northern South America. *Climate Dynamics*, doi:10.1007/s00382-017-3653-6

Hoyos N, Escobar J, Restrepo JC, Arango AM, JC Ortiz (2013) Impact of the 2010–2011 La Nina phenomenon in Colombia, South America: The human toll of an extreme weather event. *Applied Geography* 39, 16-25

Huang B, Banzon VF, Freeman E, Lawrimore J, Liu W, Peterson TC, Smith TM, Thorne PW, Woodruff SD, Zhang HM (2014) Extended Reconstructed Sea Surface Temperature version 4 (ERSST.v4): Part I. Upgrades and intercomparisons. *Journal of Climate* 28(3): 911-930

Huffman GJ, Adler RF, Bolvin DT, Nelkin EJ (2010) The TRMM multi-satellite precipitation analysis (TMPA). In: Gebremichael M, Hossain F (ed) *Satellite rainfall applications for surface hydrology*. Springer Netherlands, pp. 3-22

Hurrell JW, Holland MM, Gent PR et al. (2013) The community earth system model: a framework for collaborative research. *Bulletin of the American Meteorological Society* 94(9): 1339-1360

Hwang YT, Frierson DM (2013) Link between the double-Intertropical Convergence Zone problem and cloud biases over the Southern Ocean. *Proceedings of the National Academy of Sciences* 110(13): 4935-4940

IDEAM (2005) *Atlas Climatológico de Colombia*, IDEAM, Bogotá, Colombia, 1st edition

IDEAM (2012) *Evaluación de las simulaciones de precipitación y temperatura de los modelos climáticos globales del proyecto CMIP5 con el clima presente en Colombia*. IDEAM–METEO/147-2012

Insel N, Poulsen C, Elhers T (2010) Influence of the Andes Mountains on South American moisture transport, convection, and precipitation. *Clim Dyn* 35:1477–1492

Ji D, Wang L, Feng J et al. (2014) Description and basic evaluation of Beijing Normal University Earth system model (BNU-ESM) version 1. *Geoscientific Model Development* 7(5), 2039-2064

Jiang X, Lau NC, Held IM, Ploshay JJ (2007) Mechanisms of the Great Plains low-level jet as simulated in an AGCM. *Journal of the atmospheric sciences* 64(2): 532-547

Jones CD, Hughes JK, Bellouin N et al. (2011) The HadGEM2-ES implementation of CMIP5 centennial simulations. *Geosci Model Dev* 4: 543–570. doi: 10.5194

Kalnay et al.,(1996) The NCEP/NCAR 40-year reanalysis project. *Bull. Amer. Meteor. Soc.*, 77, 437-470, 1996

Kanamitsu M, Ebisuzaki W, Woollen J, Yang S-K, Hnilo JJ, Fiorino M, Potter GL (2002) NCEP-DOE AMIP-II Reanalysis (R-2). *Bulletin of the American Meteorological Society* 1631-1643

Kerr RA (2000) A North Atlantic climate pacemaker for the centuries. *Science*, 288 (5473), 1984-1986

Kim D, Sobel AH, Del Genio AD et al. (2012) The tropical subseasonal variability simulated in the NASA GISS general circulation model. *Journal of Climate* 25(13): 4641-4659

Kim HM, Webster PJ, Curry JA (2012) Evaluation of short-term climate change prediction in multi-model CMIP5 decadal hindcasts. *Geophysical Research Letters*, 39(10)

Knutti R (2010) The end of model democracy?. *Climatic change* 102(3-4), 395-404

Langenbrunner B, Neelin JD (2013) Analyzing ENSO teleconnections in CMIP models as a measure of model fidelity in simulating precipitation. *Journal of Climate*, 26(13), 4431-4446

Lee JY, Wang B (2014) Future change of global monsoon in the CMIP5. *Climate Dynamics*, 42(1-2), 101-119

Li T, SGH Philander (1996) On the annual cycle of the Eastern equatorial Pacific. *Journal of Climate* 9 (12)

Li L, Lin P, Yu Y e al. (2013) The flexible global ocean-atmosphere-land system model, Grid-point Version 2: FGOALS-g2. *Advances in Atmospheric Sciences* 30: 543-560

Li G, Xie SP (2014) Tropical Biases in CMIP5 Multimodel Ensemble: The Excessive Equatorial Pacific Cold Tongue and Double ITCZ Problems*. *Journal of Climate* 27(4): 1765-1780

Lorenz C, H Kunstmann (2012) The hydrological cycle in three state-of-the-art reanalyses: Intercomparison and performance analysis. *Journal of Hydrometeorology* 13(5), 1397-1420

Luo JJ, Masson S, Roeckner E, Madec G, Yamagata T (2005) Reducing climatology bias in an ocean-atmosphere CGCM with improved coupling physics. *Journal of climate* 18(13): 2344-2360

Ma CC, Mechoso CR, Robertson AW, Arakawa A (1996) Peruvian stratus clouds and the tropical Pacific circulation: A coupled ocean-atmosphere GCM study. *Journal of Climate* 9(7): 1635-1645

Maloney ED, Camargo SJ, Chang E et al. (2014) North American climate in cmip5 experiments: part iii: assessment of twenty-first-century projections*. *Journal of Climate* 27(6)

Mantua NJ, Hare SR (2002) The Pacific decadal oscillation. *Journal of the oceanography* 58(1), 35-44

Mantua NJ, Hare SR, Zhang Y, Wallace JM, Francis RC (1997) A Pacific interdecadal climate oscillation with impacts on salmon production. *Bulletin of the American Meteorological Society*, 78(6), 1069-1079

Mapes BE, Warner TT, Xu M, Negri AJ (2003) Diurnal patterns of rainfall in northwestern South America. Part I: Observations and context. *Monthly Weather Review* 131(5): 799-812

Martínez I, Keigwin L, Barrows TT, Yokoyama Y, Southon J (2003) La Niña-like conditions in the eastern equatorial Pacific and a stronger Choco jet in the northern Andes during the last glaciation. *Paleoceanography* 18(2)

Martin ER, Schumacher C (2011) The Caribbean low-level jet and its relationship with precipitation in IPCC AR4 models. *Journal of Climate* 24(22): 5935-5950

McCuen, RH, Knight Z, Cutter AG (2006) Evaluation of the Nash–Sutcliffe efficiency index. *Journal of Hydrologic Engineering*, 11(6), 597-602

Oueslati B, Bellon G (2015) The double ITCZ bias in CMIP5 models: interaction between SST, large-scale circulation and precipitation. *Climate Dynamics* 44(3-4): 585-607

Palomino-Lemus R, Córdoba-Machado S, Gámiz-Fortis SR, Castro-Díez Y, Esteban- Parra MJ (2014) Validation of tropical Pacific SLP patterns in CMIP5 models. In: Fernández-Montes S, Rodrigo FS (eds) *Cambio Climático y Cambio Global*. Asociación Española de Climatología, (AEC) Serie A 9: pp 853

Polade SD, Gershunov A, Cayan DR, Dettinger MD, Pierce DW (2013) Natural climate variability and teleconnections to precipitation over the Pacific-North American region in CMIP3 and CMIP5 models. *Geophysical Research Letters*, 40(10), 2296-2301

Poveda G, Jaramillo L, Vallejo LF (2014) Seasonal precipitation patterns along pathways of South American low-level jets and aerial rivers. *Water Resources Research* 50(1): 98-118

Poveda G, Álvarez DM, Rueda ÓA (2011) Hydro-climatic variability over the Andes of Colombia associated with ENSO: a review of climatic processes and their impact on one of the Earth's most important biodiversity hotspots. *Climate Dynamics* 36(11-12): 2233-2249

Poveda G, Waylen PR, RS Pulwarty (2006) Annual and interannual variability of the present climate in northern South America and southern Mesoamerica. *Palaeogeography, Palaeoclimatology, Palaeoecology* 234 (1)

Poveda G, Jaramillo A, Gil MM, Quiceno N, Mantilla RI (2001) Seasonality in ENSO-related precipitation, river discharges, soil moisture, and vegetation index in Colombia. *Water resources research* 37(8): 2169-2178

Poveda G, Mesa OJ (2000) On the existence of Lloró (the rainiest locality on Earth): enhanced ocean-atmosphere-land interaction by a low level jet. *Geophys Res Lett* 27:1675-1678

Qiao F, Song Z, Bao et al. (2013) Development and evaluation of an Earth System Model with surface gravity waves. *Journal of Geophysical Research: Oceans* 118(9) 4514-4524

Rasmusson EM, Carpenter TH (1982) Variations in tropical sea surface temperature and surface wind fields associated with the Southern Oscillation/El Niño. *Monthly Weather Review* 110(5): 354-384.

Rencher AC (2003) *Methods of multivariate analysis* (Vol. 492). John Wiley & Sons

Ricciardulli L, Wentz F (2011) Reprocessed QuikSCAT (V04) wind vectors with Ku-2011 geophysical model function. *Remote Sensing Systems Tech. Rep* 43011(8)

Rotstayn LD, Collier MA, Dix MR et al. (2010) Improved simulation of Australian climate and ENSO-related rainfall variability in a global climate model with an interactive aerosol treatment. *International Journal of Climatology* 30(7) 1067-1088

Russell JM, Johnson TC (2007) Little Ice Age drought in equatorial Africa: intertropical convergence zone migrations and El Niño–Southern Oscillation variability. *Geology*, 35(1): 21-24

Ruiz D, Moreno HA, Gutiérrez ME, PA Zapata (2008) Changing climate and endangered high mountain ecosystems in Colombia. *Science of the total environment*, 398 (1)

Ryu JH, Hayhoe K (2014) Understanding the sources of Caribbean precipitation biases in CMIP3 and CMIP5 simulations. *Climate dynamics* 42(11-12): 3233-3252

Sanderson BM, Knutti R, Caldwell P (2015) Addressing interdependency in a multimodel ensemble by interpolation of model properties. *Journal of Climate* 28(13): 5150-5170

Sakamoto MS, Ambrizzi T, Poveda G (2012a) Moisture sources and life cycle of convective systems over Western Colombia. *Advances in Meteorology*: 2011

Sakamoto TT, Komuro Y, Nishimura T, et al. (2012b) MIROC4h—a new high-resolution atmosphere-ocean coupled general circulation model. *気象集誌. 第2輯* 90(3): 325-359

Saurral RI, Camilloni IA, Ambrizzi T (2015) Links between topography, moisture fluxes pathways and precipitation over South America. *Climate Dynamics*, 45(3-4): 777-789. doi: 10.1007/s00382-014-2309-z

Scoccimarro E, Gualdi S, Bellucci A (2011) Effects of Tropical Cyclones on Ocean Heat Transport in a High Resolution Coupled General Circulation Model. *Journal of Climate* 24 4368-4384

Schlesinger WH (2000). *Biogeoquímica: un análisis del cambio global*. Ariel

Sierra JP, Arias PA, Vieira SC (2015) Precipitation over northern South America and its seasonal variability as simulated by the CMIP5 models. *Advances in Meteorology*. doi: 10.1155/2015/634720

Sheffield J, Barrett AP, Colle B et al. (2013) North American Climate in CMIP5 Experiments. Part I: Evaluation of Historical Simulations of Continental and Regional Climatology*. *Journal of Climate* 26(23): 9209-9245

Snow JW (1976) The climate of northern South America. In: Schwerdtfeger, W. (ed.), *Climates of Central and South America*. Elsevier, Amsterdam, pp. 295–403

Stocker TF (Ed.) (2014) *Climate change 2013: the physical science basis: Working Group I contribution to the Fifth assessment report of the Intergovernmental Panel on Climate Change*. Cambridge University Press

Tapias KA, Arias PA (2017) Los chorros de bajo nivel del Chocó y del Caribe durante el último milenio: Análisis de simulaciones CMIP5/PMIP3. Bachelor thesis, Universidad de Antioquia, Colombia

Taylor KE (2000) Summarizing multiple aspects of model performance in a single diagram. *Journal of Geophysical Research: Atmospheres* 106(D7): 7183-7192

Taylor KE, Stouffer RJ, Meehl GA (2012) An overview of CMIP5 and the experiment design. *Bulletin of the American Meteorological Society* 93(4): 485-498

Ting M, Kushnir Y, Seager R, Li C (2011) Robust features of Atlantic multi-decadal variability and its climate impacts. *Geophysical Research Letters*, 38(17)

Tjiputra JF, Roelandt C, Bentsen M et al. (2013) Evaluation of the carbon cycle components in the Norwegian Earth System Model (NorESM). *Geoscientific Model Development* 6(2): 301-325

Torres RR, JA Marengo (2013) Uncertainty assessments of climate change projections over South America. *Theoretical and applied climatology* 112(1-2)

Torrence C, Compo GP (1998) A practical guide to wavelet analysis. *Bulletin of the American Meteorological society*, 79(1), 61-78

Voldoire A, Sanchez-Gomez E, Méliá DS et al. (2013) The CNRM-CM5. 1 global climate model: description and basic evaluation. *Climate Dynamics* 40(9-10): 2091-2121

Volodin EM, Dianskii NA, Gusev AV (2010) Simulating present-day climate with the INMCM4. 0 coupled model of the atmospheric and oceanic general circulations. *Izvestiya, Atmospheric and Oceanic Physics* 46(4): 414-431

Von Storch H, Zwiers F (2013) Testing ensembles of climate change scenarios for “statistical significance”. *Climatic Change* 117(1-2), 1-9

Wang C, Zhang L, Lee SK, Wu L, Mechoso CR (2014) A global perspective on CMIP5 climate model biases. *Nature Climate Change* 4(3): 201-205

Wang J, Wang W, Fu X, KH Seo (2012) Tropical intraseasonal rainfall variability in the CFSR. *Climate Dynamics* 38 (11-12)

Wang X, Auler AS, Edwards RL et al. (2004) Wet periods in northeastern Brazil over the past 210 kyr linked to distant climate anomalies. *Nature*, 432(7018): 740-743

Watanabe M, Suzuki T, O'ishi R et al. (2010) Improved climate simulation by MIROC5: mean states, variability, and climate sensitivity. *Journal of Climate* 23(23): 6312-6335

Wilks, DS (2011) *Statistical methods in the atmospheric sciences* (Vol. 100). Academic press

Xin X, Wu T, Zhang J (2012) Introductions to the CMIP5 simulations conducted by the BCC climate system model. *Adv. Climate Change Res* 8: 378-382

Yin L, Fu R, Shevliakova E, Dickinson RE (2013) How well can CMIP5 simulate precipitation and its controlling processes over tropical South America? *Climate Dynamics* 41(11-12): 3127-3143

Yokoi S, Takayabu YN, Nishii K et al. (2011) Application of cluster analysis to climate model performance metrics. *Journal of Applied Meteorology and Climatology* 50(8): 1666-1675

Yukimoto S, Adachi Y, Hosaka M (2012) A new global climate model of the Meteorological Research Institute: MRI-CGCM3—model description and basic performance. 気象集誌. 第2輯 90(0): 23-64

Zanchettin D, Rubino A, Matei D, Bothe O, Jungclaus JH (2013) Multidecadal-to-centennial SST variability in the MPI-ESM simulation ensemble for the last millennium. *Climate dynamics* 40(5-6): 1301-1318

Zhang ZS, Nisancioglu K, Bentsen M et al. (2012) Pre-industrial and mid-Pliocene simulations with NorESM-L. *Geoscientific Model Development* 5(2): 523-533

Zhang GJ, Wang H (2006) Toward mitigating the double ITCZ problem in NCAR CCSM3. *Geophysical research letters* 33(6)

Zhang Y, Wallace JM, Battisti DS (1997) ENSO-like interdecadal variability: 1900–93. *Journal of climate*, 10(5), 1004-1020


Zubler EM, Fischer AM, Fröb F, Liniger MA (2015). Climate change signals of CMIP5 general circulation models over the Alps—impact of model selection. *International Journal of Climatology*

Zuluaga MD, Poveda G (2004) Diagnostics of mesoscale convective systems over Colombia and the eastern tropical Pacific during 1998-2002. *Avances en Recursos Hidráulicos* 11: 145-160

Avales



Paola Andrea Arias Gómez



Sara Cristina Vieira Agudelo